Nonlinear Frequency Domain Modelling of Wave Energy Converter Arrays

Application to CorPower Ocean's C5 Device

R.A. Mooldijk

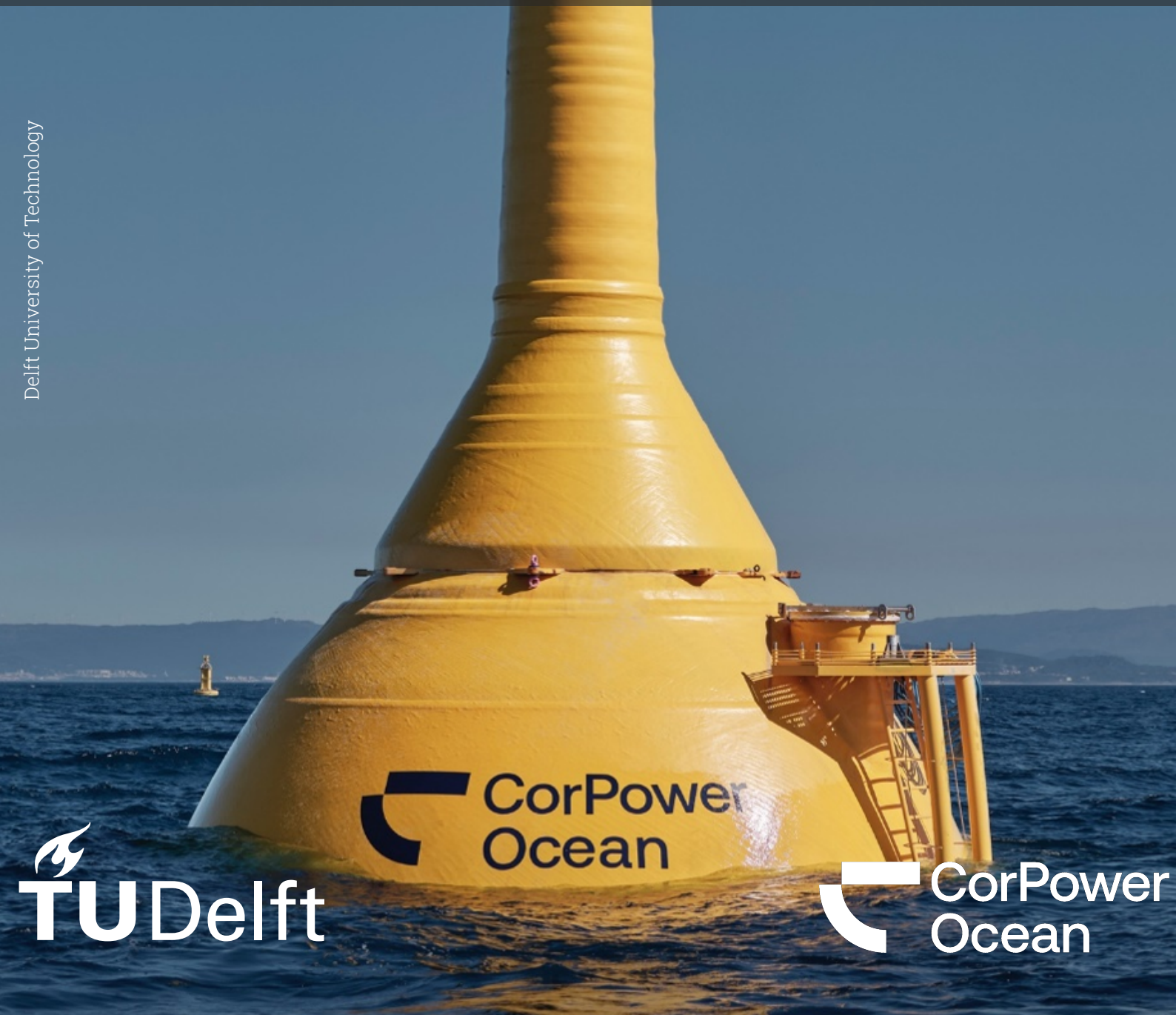

Delft University of Technology

TU Delft

CorPower Ocean

Nonlinear Frequency Domain Modelling of Wave Energy Converter Arrays

Application to CorPower Ocean's C5 Device

by

R.A. Mooldijk

to obtain the degree of Master of Science
at the Delft University of Technology,
to be defended publicly on Friday 12 December at 15:00

Student number:	4771001	
Project duration:	June 09, 2025 – December 12, 2025	
Thesis committee:	Dr. G. Lavidas,	TU Delft
	Dr. A. Antonini,	TU Delft
	Ir. V. Raghavan,	TU Delft
	Dr. J. Todalshaug,	CorPower Ocean
	Dr. T. Vervaet,	CorPower Ocean

TU Delft

Preface

This thesis concludes a long stretch at the Delft University of Technology. It has been demanding, occasionally chaotic, and shaped at each stage by the people around me.

My former housemates and the friends I gathered in Delft provided stability, humour, and the necessary distraction from an unhealthy number of late nights. In Stockholm I found a second group who made a very busy period feel lighter. Being there in the summer proved favourable. The long daylight hours and improbably good weather kept the tempo workable, and the combination of work, company, and place made the months more enjoyable than any modelling project strictly deserves.

My family supported me throughout, including their encouragement to take the opportunity in Stockholm. These years also included personal moments of weight, among them the loss of my grandfather Jan, whose influence never really left. I also want to thank Senna, whose support was constant and unmatchable, and who carried more of this period than most people will ever see. Her presence brought order, energy, and real joy to the work.

My work with the Ministry of Defence gave me experiences far outside the standard academic track. I am grateful for that trust. I am equally grateful to the colleagues at CorPower Ocean in Stockholm and Oslo, whose clarity and straightforward approach made collaboration easy. My supervisors in Delft provided direct and steady guidance, and the distance never reduced the quality of their input.

To all who contributed, I offer my thanks. The next steps are something I now look forward to.

R.A. Mooldijk
Stockholm, December 2025

Abstract

Accurate prediction of nonlinear wave structure interaction remains a challenge for the design of large wave energy converter (WEC) arrays. This thesis develops and validates a weakly nonlinear frequency domain (NLFD) framework for modelling multi device point absorber arrays in realistic irregular seas. The formulation embeds nonlinear restoring, viscous drag, and power take off (PTO) dynamics directly within the frequency domain (FD) balance while retaining linear hydrodynamic coupling from HAMS-MREL. This enables fully coupled array simulations at a fraction of the computational cost of time domain (TD) approaches.

The solver was benchmarked against a nonlinear MATLAB TD reference and verified against the linear HAMS-MREL solution. Nonlinear heave dynamics were reproduced with amplitude errors of 11 to 17% and near identical phase, and the model collapses to the linear limit when nonlinear terms are disabled. These validations establish a robust foundation for irregular sea analyses.

A systematic study across four sea states, three spacings of 5D, 10D and 15D, and four incident headings quantified the mechanisms governing array performance. Nonlinear effects broaden spectral peaks without shifting the dominant frequency. Spacing redistributes absorbed power between devices while leaving the array averaged interaction factor close to unity. Hydrodynamic coupling is weak beyond roughly ten diameters, but nonlinear and directional effects still introduce measurable differences between rows at 15D. Directional incidence imposes the strongest control: long side headings between 60° and 90° maintain radiative synchronisation and produce mild constructive interaction, whereas oblique headings reduce phase coherence and suppress amplification.

A device level case study shows that array behaviour is governed by radiative phase alignment rather than geometric proximity. Devices experiencing radiative softening exhibit larger response and absorbed power, while those subject to radiative stiffening show reduced motion despite nearly identical incoming excitation. This establishes the link between local impedance modification and array scale performance.

Overall, the results show that weakly NLFD methods capture the essential physics of large WEC arrays with clarity, computational efficiency, and controlled accuracy. The framework supports phase based layout, directional alignment, and PTO tuning strategies for early stage design of future wave energy farms.

Contents

List of Figures

List of Tables

List of Abbreviations

BEM boundary element method.

CPO CorPower Ocean AB.

DOF degree of freedom.

FD frequency domain.

HAMS-MREL Hydrodynamic Analysis of Marine Structures – Marine Renewable Energies Lab.

IM impedance matching.

JONSWAP Joint North Sea Wave Project.

NLFD nonlinear frequency domain.

PTO power take-off.

RAO response amplitude operator.

RMS root mean square.

SD spectral domain.

TD time domain.

WEC wave energy converter.

Nomenclature

List of principal symbols used in the thesis.

α	JONSWAP energy scaling factor	-
β	Wave incidence heading	$^\circ$
Δt	Time step used in time-domain simulations	s
$\dot{\zeta}_{\mathrm{eff}}(t)$	Velocity after admissible-rate limiting	$\mathrm{m\,s^{-1}}$
$\dot{\zeta}_{\mathrm{rms}}$	Root-mean-square velocity	$\mathrm{m\,s^{-1}}$
$\dot{x}$	Velocity amplitude (complex or instantaneous)	$\mathrm{m\,s^{-1}}$
$\frac{\partial \mathbf{F}_{\mathrm{NL}}^{(i)}}{\partial \mathbf{X}^{(i)}}$	Local nonlinear-force Jacobian for device i	-
$\frac{\partial F_{\mathrm{NL}}}{\partial \dot{z}}$	Sensitivity of nonlinear force to velocity	-
$\frac{\partial F_{\mathrm{NL}}}{\partial z}$	Sensitivity of nonlinear force to displacement	-
γ	JONSWAP peak enhancement factor	-
$\int S_{zz}\, d\omega$	Integrated displacement spectrum	$\mathrm{m^2}$
$\mathbf{E}$	Vector of excitation Fourier coefficients	N
$\mathbf{E}_k$	Excitation Fourier coefficients at harmonic k	N
$\mathbf{F}(\mathbf{X})$	Fourier projection of nonlinear forces	N
$\mathbf{F}_{\mathrm{exc}}(\omega)$	Complex excitation force vector	N
$\mathbf{F}_{\mathrm{exc},i}(\omega)$	Excitation force vector for device i	N
$\mathbf{F}_{\mathrm{NL}}(\mathbf{X})$	Vector of nonlinear force Fourier projections for all devices	N
$\mathbf{G}(\mathbf{X})$	Residual vector in harmonic balance	-
$\mathbf{J}_{\mathrm{NL}}$	Block-diagonal Jacobian of nonlinear forces	-
$\mathbf{r}_G$	Centre of gravity position vector	m
$\mathbf{X}$	Vector of Fourier displacement coefficients	m
$\mathbf{X}(\omega)$	Complex displacement amplitude	m
$\mathbf{X}(t)$	Time-domain displacement vector	m
$\mathbf{X}^H(\omega)$	Complex conjugate transpose of $\mathbf{X}$	-
$\mathbf{X}_k$	Fourier coefficient vector at harmonic k for all devices and modes	-
$\mathrm{RAO}(\omega)$	Response amplitude operator	-
∇	Gradient / Laplacian operator	-
ω	Angular frequency	$\mathrm{rad\,s^{-1}}$

ω_i	Discrete angular frequency sample	$\mathrm{rad\,s^{-1}}$
ω_p	Peak angular frequency	$\mathrm{rad\,s^{-1}}$
ω_{res}	Resonant angular frequency	$\mathrm{rad\,s^{-1}}$
$\overline{\zeta}$	Mean displacement over a segment	m
$\overline{H_X(\omega)}$	Ensemble averaged response spectrum	-
$\overline{S_{zz}}$	Mean displacement spectral density over the energetic band	$\mathrm{m^2 s}$
∂	Partial-derivative operator	-
ϕ	Velocity potential	-
ϕ_{exc}	Excitation phase angle	-
ϕ_{resp}	Response phase angle	-
σ	JONSWAP spectral width parameter	-
$\tanh(\cdot)$	Hyperbolic tangent saturation operator	-
θ_j	Discrete wave-incidence directions	$^\circ$
θ_p	Mean wave direction	$^\circ$
ζ	Single-DOF displacement	m
A	Reference area for drag	$\mathrm{m^2}$
$A(\omega)$	Added-mass matrix	-
$A(z)$	Waterplane area at vertical coordinate z	$\mathrm{m^2}$
a_0	DC Fourier coefficient of displacement	m
$A_{\mathrm{wave}}(\omega)$	Complex incident wave amplitude	m
a_n	Cosine Fourier coefficient of displacement	m
$A_{\mathrm{lookup}}(z_{\mathrm{rel}})$	Lookup waterplane-area function	$\mathrm{m^2}$
$A_{\mathrm{rot,lookup}}(z_{\mathrm{rel}})$	Lookup lateral projected area function	$\mathrm{m^2}$
$A_{\mathrm{rot}}(z)$	Lateral projected area for rotational modes	$\mathrm{m^2}$
$B(\omega)$	Radiation damping matrix	-
B_{PTO}	PTO damping contribution	-
b_n	Sine Fourier coefficient of displacement	m
B_{PTO}	Linear PTO damping coefficient	$\mathrm{N\,s\,m^{-1}}$
C	Linear hydrostatic stiffness for single-DOF	$\mathrm{N\,m^{-1}}$
C_d	Drag coefficient	-
$C_{d,\theta}$	Quadratic drag coefficient for rotational modes	-
D	Device diameter	m
d	Water depth	m

$D_{\mathrm{hydro}}(\omega)$	Hydrodynamic dynamic stiffness operator	-
$e(t)$	Time-domain excitation force	N
F_p	Peak wave frequency	Hz
F_0	Static PTO preload force	N
$F_{\mathrm{b}}(t)$	Buoyancy force	N
$F_{\mathrm{drag}}(t)$	Viscous drag force	N
$F_{\mathrm{lin}}(t)$	Linearised hydrostatic force	N
f_{NL}	Nonlinear force contribution	N
$F_{\mathrm{NL}}(t)$	Total nonlinear force or moment	N
$F_{\mathrm{PTO,lin}}$	Linear PTO force model $-B_{\mathrm{PTO}}\dot{x}$	N
F_{PTO}	Nonlinear saturated PTO force	N
$F_{\mathrm{rest}}(t)$	Nonlinear restoring force	N
$F_{\max}$	Maximum admissible PTO force	N
g_ℓ	Linear operator collecting inertia, radiation, and hydrostatic terms	-
H	Wave height	m
H_s	Significant wave height	m
$H_X^{(j)}(\omega)$	Response spectrum of segment j	-
K	Hydrostatic restoring matrix	-
K_{PTO}	PTO stiffness contribution	-
k_h	Hydrostatic stiffness in heave	$\mathrm{N\,m^{-1}}$
L	Wavelength	m
L_{anchor}	Lever arm for rotational restoring and drag	m
M	Rigid-body mass and inertia matrix	-
m	Rigid-body mass (single-DOF)	kg
$M_{\mathrm{drag}}(t)$	Viscous rotational drag moment	N m
M_{HB}	Harmonic-balance linear operator	-
$M_{\mathrm{rest}}(t)$	Restoring moment in roll or pitch	N m
N	Number of WEC devices in the array	-
N_h	Number of Fourier harmonics	-
n_{dev}	Number of devices in the array	-
n_{dof}	Number of retained rigid-body degrees of freedom	-
N_{seg}	Number of simulated segments per sea state	-
N_ω	Number of discrete frequency points	-

$P_{\mathrm{abs}}(\omega)$	Absorbed power at frequency ω	W
P_i	Mean absorbed power of device i in the array	W
P_{abs}	Absorbed power computed from instantaneous PTO force and velocity	W
P_{array}	Total absorbed power of the array	W
P_{single}	Absorbed power of an isolated device	W
q	Interaction factor of a device	-
r_i	Device–level power ratio relative to the single device	-
R_{eq}	Effective radius at equilibrium waterplane	m
S	Inter-device spacing	m
$S(\omega)$	One-dimensional wave spectral density	$\mathrm{m^2 s}$
s_B	Scaling factor applied to B_{PTO}	-
s_K	Scaling factor applied to K_{PTO}	-
$S_{zz}(\omega)$	One-sided displacement power spectral density	$\mathrm{m^2 s}$
T	Wave period	s
T_e	Energy period	s
T_p	Peak wave period	s
T_{seg}	Duration of one simulation segment	s
$V(z)$	Displaced volume at vertical coordinate z	$\mathrm{m^3}$
v_{lim}	Maximum admissible PTO velocity	$\mathrm{m\,s^{-1}}$
$V_{\mathrm{lookup}}(z_{\mathrm{rel}})$	Lookup displaced-volume function	$\mathrm{m^3}$
x	Horizontal coordinate	m
x_G	Centre-of-gravity coordinate in x	m
y	Horizontal coordinate	m
y_G	Centre-of-gravity coordinate in y	m
z	Vertical coordinate	m
$Z(\omega)$	Fourier transform of $z(t)$	$\mathrm{m\,s}$
$z(t)$	Mean-removed displacement signal	m
$Z_{\mathrm{rad}}(\omega)$	Radiation impedance	-
z_{eq}	Equilibrium vertical position	m
$Z_{\mathrm{H}}(\omega_k)$	Full hydrodynamic impedance matrix including interaction terms	-
z_{rel}	Displacement relative to equilibrium $z - z_{\mathrm{eq}}$	m
z_G	Centre-of-gravity coordinate in z	m

1

Introduction

1.1. Background

The European push for decarbonisation and energy independence has sparked increased interest in ocean energy as a reliable and renewable source. Wave energy, in particular, offers high predictability and energy density, and the IPCC estimates its global potential at 29,500 TWh annually, nearly ten times the current electricity consumption of Europe [1]. If Europe establishes leadership in this field, up to 500,000 jobs could be created by 2050 [2].

Despite these opportunities, wave energy technologies remain comparatively immature when benchmarked against wind and solar. The sector faces unique technical challenges: the stochastic and multi-directional nature of waves, the harsh marine environment, and the complexity of wave–-structure interactions all contribute to slow technology uptake [3, 4]. Within this context, point absorber wave energy converters (WECs) have gained attention due to their compact geometry, broadband responsiveness, and favourable power-to-footprint ratio [4, 5, 6]. Their dimensions remain small relative to the incident wavelength, which supports efficient omnidirectional energy capture [3, 7]. The same compactness allows dense array placement, while their dynamic response can be tuned to prevailing wave conditions to improve performance [5, 6].

Recent studies report array level power-to-footprint ratios for point absorbers around 10–12 W/m^2, which is significantly higher than wind but lower than the device only metric often cited in the literature [8].

One of the frontrunners in this space is CorPower Ocean AB (CPO), a Swedish developer of phase-controlled point absorbers. The company's latest device, the C5, represents a pre-commercial system that integrates advanced control strategies to enhance resonance tuning and energy capture. At the heart of this approach is the 'WaveSpring' mechanism, which dynamically adjusts the buoy's response to incoming waves, enabling both resonance amplification for optimal power generation and detuning for storm survivability [9, 10]. Building on lessons learned from the previous C4 prototype, the C5 introduces hydrodynamic refinements, larger scale, and embedded actuation systems designed to actively tune the device response to wave conditions. This combination of phase control and resonance tuning allows the device to maximise energy extraction while maintaining stability and reliability in varying sea states.

1.2. Problem Setting and Research Objectives

Scaling wave energy from single devices to commercially viable arrays introduces a fundamental systems challenge: energy absorption is no longer determined solely by the response of an individual converter, but by the collective hydrodynamics of the array. Each WEC modifies the surrounding wave field through diffraction and radiation, altering the excitation environment of neighbouring devices [11, 12]. These interactions are highly sensitive to array geometry and wave conditions, and can result in constructive or destructive interaction that amplifies or suppresses overall response [13].

Classical frequency domain (FD) models provide an efficient means of simulating these interactions, but they are limited to linear hydrodynamics and linearised device dynamics. Nonlinear effects are usually studied in the time domain (TD), which captures them accurately but at high computational cost. Recent studies have shown that nonlinear frequency domain (NLFD) methods can reproduce selected nonlinear behaviours with accuracy comparable to TD solvers, while retaining the efficiency of FD analysis [14, 15].

Despite this progress, most applications remain restricted to single WEC systems or simplified array models. The combined influence of multiple nonlinear effects on hydrodynamically coupled, multi–degree of freedom (DOF) arrays has not been systematically investigated. In particular, little is known about how nonlinearities alter spectral content, velocity statistics, phase structure and coherence across arrays, or how these changes depend on spacing and directional incidence.

This gap motivates the development of weakly NLFD models capable of resolving array-scale interactions under realistic sea states. By moving beyond absorbed power and incorporating the underlying nonlinear response mechanisms, such models expose the behaviour of large WEC arrays under nonlinear dynamics.

1.3. Research Questions

The main research question of this thesis is:

> *How can a weakly nonlinear frequency domain model characterise the dynamic behaviour and power performance of large WEC arrays under realistic sea conditions?*

To address this central question, the following sub-questions are formulated:

1. To what extent does the model reproduce established time domain results?
2. How accurately does the developed nonlinear frequency domain solver reproduce the linear hydrodynamic behaviour predicted by HAMS-MREL?
3. How do nonlinear effects influence spectral amplification and absorbed power for a single device under varying sea states?
4. How does inter-device spacing modify array-scale hydrodynamic interactions and power absorption?
5. How does wave incidence direction modify array-scale hydrodynamic interactions and power absorption?

1.4. Scope and Limitations

This study focuses on the hydrodynamic performance of fixed layout point absorber arrays using CPOs C5 as a representative case. The modelling framework is based on FD simulations with weakly nonlinear forces implemented through NLFD. Structural flexibility, mooring dynamics, detailed power take-off (PTO) models, and feedback control are excluded.

Validation against external data is limited to comparisons with linear FD results from Hydrodynamic Analysis of Marine Structures – Marine Renewable Energies Lab (HAMS-MREL) under irregular waves, and MATLAB TD experimental data for a single WEC, single DOF under regular waves.

Wave conditions are restricted to regular waves and irregular unidirectional seas represented by the Joint North Sea Wave Project (JONSWAP) spectrum. Directional seas, site-specific bathymetry, tidal currents, and economic assessments fall outside the scope. The emphasis is on developing a physically consistent yet computationally efficient modelling approach that enables systematic analysis of hydrodynamic interactions, nonlinear effects, and directional sensitivity in large arrays.

1.5. Modelling Approach

This research employs a simulation-based methodology, combining hydrodynamic modelling with NLFD analysis. Frequency-dependent hydrodynamic coefficients are first generated using HAMS-MREL, an open source boundary element method (BEM) solver specifically developed for multi-body hydrodynamic analysis of marine renewable energy arrays [16]. HAMS-MREL provides added mass, radiation damping, and excitation forces for multiple interacting bodies, and has been validated against both semi-analytical solutions and commercial solvers. These coefficients are then used as input to a custom Python-based solver implementing a NLFD formulation capable of evaluating array performance under irregular unidirectional seas.

To improve physical realism, weakly nonlinear effects are included. Unless otherwise specified, nonlinearities in this thesis refer to viscous drag, nonlinear hydrostatic restoring, and PTO saturation. These effects are approximated within the FD framework using harmonic balance, allowing nonlinear forces to be incorporated while retaining computational efficiency.

The modelling pipeline includes targeted validation against established reference models. Linear FD results from HAMS-MREL verify the hydrodynamic formulation, and MATLAB TD data confirm the nonlinear single-device behaviour. After this validation, the extended NLFD model is applied to analyse array dynamics under realistic seas. The analysis evaluates changes in device dynamics, including velocity statistics, phase behaviour, spacing sensitivity and heading dependence. Power output is included for context, but the focus remains on how nonlinear effects modify the underlying device response. Phase and short time series plots support the interpretation where required.

1.6. Thesis Structure

The remainder of this thesis is organised as follows:

- **Chapter 2: Literature Review** — Synthesises existing research on WEC array hydrodynamics, FD modelling, nonlinear extensions, and the treatment of directional seas. It highlights unresolved challenges and motivates the focus on weakly NLFD methods.
- **Chapter 3: Theoretical Framework** — Presents the governing hydrodynamic principles and FD formulation underpinning the simulation of WEC arrays, including wave representation, array interactions, the computation of hydrodynamic coefficients, and the incorporation of weakly nonlinear effects.
- **Chapter 4: Methodology** — Details the numerical implementation, including hydrodynamic coefficient generation with HAMS-MREL, the NLFD solver architecture, representation of nonlinear forces, and key model assumptions.
- **Chapter 5: Results** — Combines the presentation and interpretation of results. Each section discusses the findings directly in relation to literature, addressing model validation, nonlinear response behaviour, array spacing effects, and directional sensitivity. The chapter concludes with a synthesis section that consolidates the main trends, identifies model limitations, and summarises the broader physical implications of the results.
- **Chapter 6: Conclusions and Recommendations** — Concludes the thesis by addressing the main research question, summarising the core contributions, and identifying avenues for future work.

2

Literature Review

The design of WECs in arrays depends on two capabilities: accurate modelling of hydrodynamic interactions and methods that remain robust at scale. This chapter reviews four themes central to these aims: FD hydrodynamic modelling and layout sensitivity, NLFD extensions, directional wave effects, and the comparative performance of BEM solvers for multi-body systems.

The literature was identified through structured searches on Google Scholar, Scopus, and ScienceDirect using Boolean keyword combinations aligned with these themes. Studies were assessed for modelling framework, array geometry, treatment of directionality, and representation of nonlinear phenomena.

By tracing these strands, the chapter clarifies the current state of array-scale modelling and highlights remaining challenges. The reviewed work shows the limitations of uniform assumptions and the potential of FD approaches that integrate hydrodynamic coupling, nonlinear effects, and array geometry. These insights motivate the thesis focus on scalable, physically consistent modelling of fixed WEC arrays.

2.1. Theme 1: Frequency Domain Modelling, Hydrodynamic Interactions, and Layout Sensitivity

Hydrodynamic interactions, arising from wave diffraction and radiation, are central to the performance of WEC arrays. In closely spaced layouts, each device alters the incident and scattered wave field experienced by its neighbours. These effects depend strongly on spacing, symmetry, and wave conditions. This theme reviews FD modelling techniques used to resolve such interactions, with emphasis on BEM-based solvers that balance accuracy and computational efficiency.

Hydrodynamic Coupling and Layout Effects in Frequency Domain Models

Array layout has a pronounced influence on absorbed power through interaction patterns. Shao et al. [17] used a BEM-based solver to study 4×4 and 8×2 arrays, showing that elongated layouts reduce shielding in regular waves, while compact configurations perform better under irregular seas. Yang et al. [18], reviewing over 80 optimisation studies, highlighted the trade-off between compactness and constructive interaction, and the difficulty of extending FD models to directional or nonlinear scenarios. Zhong and Yeung [19] demonstrated with a semi-analytical model that symmetry can enhance interaction factors up to $q = 1.4$, though this benefit declines as asymmetry or spacing increases.

Babarit [12] introduced the “park effect” to describe losses in downstream rows of aligned arrays, concluding that reducing row count and increasing spacing improves capture. Cotey [20], using a transfer matrix model, similarly identified spacing patterns that raised interaction factors toward 1.8. Zeng et al. [21] coupled a BEM model with a genetic algorithm to show that optimal inter-device distance depends on local wave climate. Balitsky et al. [22] found that incidence angle and spectral spread significantly weaken constructive interaction. Shao et al. [23] reported that staggered hexagonal and star layouts reduce shadowing and improve both power and levelised cost in directional seas. Raghavan et al. [24] confirmed that at spacings of 15D or more, devices respond almost independently and hydrodynamic coupling becomes negligible.

Frequency Domain Modelling and Nonlinear Extensions

Linear potential flow models remain the standard for simulating WEC arrays in the FD. These models are computationally efficient and agree well with experiments under small amplitude wave conditions. However, they cannot capture nonlinear force effects which limits their value in systems with strong dynamic coupling.

To address these shortcomings, Tan et al. [25] introduced a weakly nonlinear spectral domain (SD) model incorporating PTO saturation via statistical linearisation, reducing power prediction error from 24% to 4% compared with TD results. Bonfanti and Sirigu [26] applied a similar method to the ISWEC platform, demonstrating that efficiency can be maintained while including key nonlinearities.

Husain et al. [27] proposed a transfer function approach that preserves passivity in multi-body radiation force models, validated on a 3×3 array of CPO like devices under irregular conditions. Giorgi et al. [28] developed a six-DOF nonlinear model for axisymmetric point absorbers, showing that heave–pitch coupling can either enhance or diminish power depending on the excitation spectrum and response amplitude.

Together, these studies demonstrate that incorporating simplified nonlinear terms into FD solvers can notably improve predictive accuracy while retaining the computational advantages that make frequency-based modelling attractive for design and optimisation.

Synthesis

The reviewed studies confirm that array geometry, including spacing, row configuration, and symmetry, strongly shapes hydrodynamic interactions and overall performance. Layout optimisation has been widely explored using BEM-based and semi-analytical models, but commonly under the assumption of globally uniform device dynamics.

Recent advances in FD modelling allow selected nonlinear effects to be incorporated without switching to full TD simulation. Studies by Tan et al. [25], Husain et al. [27], and Giorgi et al. [28] show that phenomena such as PTO saturation and nonlinear hydrostatics can be represented efficiently within the FD. These developments extend the applicability of frequency-based solvers to more realistic array-scale conditions.

2.2. Theme 2: Nonlinear Frequency Domain Modelling of WECs

Classical FD models provide an efficient framework for simulating the dynamics of WECs, but their scope is limited to linear hydrodynamics and linearised device dynamics. Nonlinear effects are typically addressed through TD simulation, which is accurate but computationally intensive, or through statistical linearisation, which can reduce fidelity in strongly nonlinear regimes. The NLFD, based on harmonic balance and Galerkin projection, offers a promising alternative by representing nonlinear forces within the same spectral basis used for radiation and diffraction. This section reviews the theoretical foundations of NLFD, its early applications to WEC modelling, and more recent extensions that demonstrate its potential for multi-DOF systems and arrays.

Foundational Work on Nonlinear Frequency Domain Methods

The NLFD method is formulated by projecting the governing equations of motion onto a Fourier basis and solving for the steady-state coefficients through harmonic balance. This transforms the nonlinear system of differential equations into a coupled algebraic system, where nonlinear force contributions are evaluated in the TD and reprojected into the SD at each iteration. The approach was first developed in the nonlinear vibrations community, where Failla, Spanos, and Di Paola [15] established a Galerkin framework for multi-DOF oscillators under random excitation. Their formulation introduced cubicisation techniques for general nonlinearities and demonstrated efficient Newton-Raphson iteration for solving the residual equations. They also provided methods for constructing spectral density matrices of displacement and velocity responses, setting a mathematical foundation for extending harmonic balance to complex systems.

Merigaud and Ringwood later introduced the method to wave energy applications. In their early studies [14, 29], the NLFD approach was applied to heaving point absorbers and oscillating wave surge converters. Results were benchmarked against both TD Runge–Kutta schemes and SD statistical linearisation. The method reproduced the nonlinear response with accuracy comparable to TD simulations while retaining radiation–memory effects directly in the FD, eliminating the need to evaluate the radiation convolution integral that appears in TD formulations. These studies established NLFD as a viable and efficient alternative for nonlinear WEC dynamics, while also highlighting limitations in convergence robustness and applicability to strongly non-smooth nonlinearities.

Subsequent analyses of multi-DOF harmonic balance formulations [30] confirmed that while computational gains of one to two orders of magnitude can be achieved relative to TD solvers, the algorithm's convergence is particularly sensitive to the initial Newton–Raphson state under highly energetic or strongly nonlinear conditions. Such cases may yield multiple equilibrium solutions or local divergence when the solver is started from the linear solution. These effects define the practical stability bounds of the weakly nonlinear assumption. In the present study, these challenging sea states are deliberately included to test the robustness of the implementation and identify the onset of numerical stiffness within the array simulations.

Recent Advances in WEC Modelling with NLFD

Recent studies have explored NLFD and related approaches in the context of wave energy. Guiver [31] reformulated the dynamics of a heaving point absorber with nonlinear viscous damping as a forced Lur'e system, applying nonlinear frequency response methods to the design of constrained PTO control laws. This work demonstrated that Fourier-based formulations can accommodate nonlinear damping within a single-DOF oscillator, while emphasising that the approach is limited to steady state responses.

Array-level applications remain largely linear. Wei et al. [32] developed a FD model for the Ocean Grazer floater blanket, incorporating mechanical constraints between floaters. Their analysis revealed anti-resonance behaviour in dense arrays but did not include nonlinear forces; NLFD was mentioned only as a possible extension. By contrast, Jin, Zhang, and Xu [33] combined potential flow hydrodynamics with nonlinear mooring stiffness to investigate buoy arrays. Their results showed that nonlinear restoring broadened the frequency response and improved energy capture at low frequencies, underlining the importance of nonlinear dynamics in array models.

These contributions indicate that while NLFD and related FD methods can capture selected nonlinear effects, applications to multi-DOF hydrodynamically coupled arrays remain largely unexplored.

Synthesis

The reviewed studies establish that NLFD can reproduce nonlinear oscillator dynamics with high accuracy and efficiency, offering a clear alternative to TD solvers. Failla et al. provided the theoretical foundation for multi-DOF systems, while Merigaud and Ringwood demonstrated its suitability for single-DOF WECs subject to nonlinear forces. Subsequent work has shown that frequency-based approaches can capture selected nonlinearities, as in Guiver's study of nonlinear damping, Wei's array modelling with mechanical constraints, and Jin's analysis of nonlinear stiffness in buoy arrays.

Together these contributions confirm the potential of NLFD for wave energy applications, but also reveal clear limitations. Most applications remain confined to single-DOF devices or focus on isolated nonlinear effects. Array models are typically linear, with nonlinear dynamics either excluded or treated in simplified form. Systematic applications of NLFD to hydrodynamically coupled multi-DOF arrays under irregular seas are notably absent from the literature.

2.3. Theme 3: Directional Wave Effects on Arrays

Most WEC array models assume waves approach from a single fixed direction, typically head-on. However, real offshore wave climates are rarely unidirectional. Oblique and multi-directional wave fields alter the excitation forces experienced by each WEC and shift the interaction patterns within the array. These changes may amplify or reduce overall power absorption depending on device placement and array geometry. This theme reviews how the literature treats directional variability, focusing on FD models that simulate wave incidence from a range of angles.

Directional Sensitivity in Layout Optimisation

Early studies highlight the critical influence of wave direction on array performance. Child and Venugopal [13] used a linear potential flow model to optimise five-device layouts for a single wave heading. When these layouts were exposed to a broader range of angles, performance losses reached up to 40% due to changes in phase alignment. The authors introduced a robustness metric based on integrating the interaction factor $\bar{q}(\beta)$ over a range of headings, showing that some asymmetric configurations maintain more consistent performance under angular variation.

Balitsky et al. [22] used a coupled BEM and mild slope wave model to study two arrays separated by a navigational gap. They found that a change in wave angle of just 15° could reduce power output in the downstream array by more than 20% due to wave redirection and shadowing. Zhao et al. [34] studied rectangular oscillating water column arrays and found that resonance phenomena triggered by oblique wave incidence degraded hydrodynamic efficiency. McGuinness and Thomas [35] optimised a five-device point absorber WEC layouts for average performance across a directional band. While they achieved interaction factors up to $\bar{q}(\beta) = 1.95$ for narrow incidence windows, broader directional ranges imposed clear trade-offs between peak performance and robustness.

Directional Response Mapping and Interaction Metrics

More recent work has quantified how performance metrics evolve across changing wave headings and spectral conditions. Raghavan et al. [24] used the HAMS-MREL solver to compute full array power matrices for CPO like layouts, showing that arrays tuned for head-on waves can lose up to 30% of output at 60° due to destructive interaction. The directional interaction factors they reported underscore the importance of including angular variability in array evaluation.

Tay et al. [36] applied WAMIT and post processing tools to compare three array types under directional seas. Terminator arrays reached interaction factors above 1.2 in head-on conditions, whereas point absorber arrays remained close to unity due to symmetry. Under double-peaked spectra, some configurations displayed enhanced performance and spatial variation in wave energy, suggesting potential for design strategies that leverage broadband directional response.

Zou et al. [37] used a coupled TD simulation framework to model directional wave fields and diffraction. Removing diffraction and refraction reduced array output by up to 40%. Triton type devices achieved q factors up to 1.07 even without layout tuning, confirming that spatial gradients in incident energy affect both power and variability.

Modelling Tools for Scalable Directional Hydrodynamics

Several of the above studies rely on solvers capable of handling directional wave incidence efficiently. Raghavan et al. [16] benchmarked the HAMS-MREL solver against WAMIT and demonstrated its suitability for high resolution directional modelling. By allowing arbitrary wave headings and supporting parallel execution, it can generate full angular power maps and interaction surfaces for large arrays at reduced computational cost.

Synthesis

The literature consistently shows that directional wave incidence reshapes array-scale hydrodynamics and alters both interaction patterns and power absorption. Layouts optimised for a single angle often perform poorly when the direction shifts. Resonance effects, shadowing, and uneven energy distribution all contribute to performance losses in realistic sea states.

2.4. Theme 4: Comparison of BEM Solvers for WEC Modelling

Accurate hydrodynamic modelling is central to predicting the performance of WECs. Among the available approaches, BEM solvers are widely used for computing FD hydrodynamic coefficients due to their strong basis in linear potential flow theory and their computational efficiency. Commonly used BEM solvers include commercial packages such as WAMIT and AQWA, open source tools like NEMOH and Capytaine, and research oriented solvers such as HAMS-MREL. These solvers differ in their treatment of multiple interacting bodies, mesh handling, efficiency, and ability to manage irregular frequencies. Selecting the most appropriate solver depends on both the application and the simulation requirements.

Several recent studies have compared the capabilities of these solvers in the context of WEC applications. Penalba et al. [38] compared WAMIT and NEMOH, highlighting differences in computational performance and the fidelity of hydrodynamic coefficients for floating devices. Kass [39] extended this comparison to include Capytaine, WAMIT, and Ansys AQWA, showing that solver performance varies strongly with device complexity and wave conditions. Raghavan et al. [16, 40] benchmarked HAMS-MREL against both WAMIT and NEMOH, demonstrating good agreement in excitation forces and response amplitude operators (RAOs) while also showing superior scalability for multi-body and directional wave cases.

Key differences emerge in four areas. First, support for multi-body interactions varies widely. WAMIT and AQWA support multi-body simulations but are constrained in flexibility and layout options. Capytaine computes hydrodynamic coefficients for multiple bodies but does not provide full multi-body hydrostatic or global equation of motion assembly, leaving these steps to the user. Both NEMOH and HAMS-MREL handle multi-body problems more robustly. Second, irregular frequency handling presents challenges. NEMOH is prone to spurious results in certain frequency ranges, while HAMS-MREL applies built in removal techniques to ensure smooth outputs, similar to WAMIT and AQWA. Third, computational efficiency depends on geometry complexity and solver architecture. Capytaine is efficient for simple shapes but scales poorly for complex systems. WAMIT and AQWA perform well for high-fidelity geometries but require commercial licenses. In contrast, HAMS-MREL supports parallelisation and maintains accuracy with reduced cost for large arrays. Fourth, solver openness and flexibility differ. Only Capytaine, NEMOH, and HAMS-MREL are fully open source, and of these HAMS-MREL offers the most mature interface for directional and array-scale modelling.

A comparative summary of these solvers is provided in Appendix A, outlining solver type, multi-body capabilities, efficiency, and application domains.

Based on these insights, HAMS-MREL is selected for this thesis due to its suitability for modelling CPO's fixed 2×7 array of WECs. HAMS-MREL provides reliable estimates of hydrodynamic coefficients across all six DOF and supports simulation of directional wave fields with position-dependent excitation effects. It is optimised for deep water conditions and scales efficiently to large arrays, making it especially appropriate for array-level design. Compared to other open source solvers, HAMS-MREL offers more robust treatment of irregular frequencies and improved handling of device coupling. Finally, its transparency and modifiability make it well suited for academic research that seeks to incorporate weakly nonlinear extensions.

This thesis therefore builds on the validated capabilities of HAMS-MREL to produce high-fidelity FD simulations of coupled WEC arrays under realistic wave conditions. The solver's strengths in array-scale hydrodynamics, directional wave modelling, and computational performance are essential for meeting the research objectives outlined in Chapter 1.

2.5. Research Gap

The reviewed literature demonstrates substantial progress in WEC array modelling and layout optimisation. Linear FD solvers, including BEM-based tools such as HAMS-MREL, provide reliable predictions of hydrodynamic interactions and have been widely applied to array studies. At the same time, nonlinear effects are typically addressed in the TD, which offers accuracy but at high computational cost.

Extensions of FD modelling to nonlinear dynamics have begun to emerge through NLFD methods. Foundational work has shown that NLFD can efficiently reproduce single-device responses with selected nonlinearities, while maintaining accuracy close to TD solutions. More recent studies have explored specific nonlinear effects or constrained array configurations, but these applications remain narrow in scope and typically address one nonlinearity at a time. Moreover, the majority of studies emphasise absorbed power as the main performance measure, with relatively little attention to the underlying spectral or TD behaviour that governs array dynamics.

Despite these advances, systematic applications of NLFD to hydrodynamically coupled multi-DOF arrays under irregular seas are notably absent. The literature therefore lacks a comprehensive framework to assess how nonlinear forces reshape the dynamic response of realistic WECs, and how these effects interact with spacing, layout, and directional variability.

3

Theoretical Framework

This chapter presents the theoretical basis for the FD modelling framework used to simulate the dynamics of WEC arrays. It defines the physical assumptions, governing equations, and numerical principles that underpin the simulation approach developed in Chapter 4. The framework establishes the formulation of array dynamics and interaction mechanisms, and introduces the role of weakly nonlinear extensions within the FD.

The modelling approach is grounded in linear potential flow theory, which assumes inviscid, incompressible, and irrotational flow. Wave excitation, radiation, and diffraction forces are expressed in the FD and computed using a BEM approach via the HAMS-MREL solver. While the full six rigid-body DOF are included in the hydrodynamic description, later sections examine the extent to which a reduced order representation focusing on heave, roll, and pitch may be sufficient, depending on the motion amplitudes and coupling effects observed.

To improve physical realism without abandoning the efficiency of the FD formulation, weakly nonlinear forces are incorporated using a NLFD approach. These include nonlinear hydrostatic restoring, viscous drag, and simplified PTO saturation. Within the harmonic balance framework, nonlinear terms are evaluated in the TD and reprojected into the FD, enabling their integration alongside the linear hydrodynamic coefficients.

The following sections introduce the governing assumptions, system equations, and nonlinear extensions, as well as the role of HAMS-MREL in providing the hydrodynamic coefficients that form the foundation of the modelling pipeline.

3.1. Modelling Foundations and Assumptions

The hydrodynamic modelling framework used in this thesis is based on linear potential flow theory in the FD [41, 42]. Wave-structure interaction is modelled as steady-state and small-amplitude, enabling superposition and harmonic response. The fluid is assumed inviscid, incompressible, and irrotational, and the velocity potential ϕ satisfies Laplace's equation.

$$\nabla^2\phi = \frac{\partial^2\phi}{\partial x^2} + \frac{\partial^2\phi}{\partial y^2} + \frac{\partial^2\phi}{\partial z^2} = 0 \tag{3.1}$$

These simplifications ensure that the wave–structure interaction can be linearised and decomposed into harmonic components, enabling efficient simulation of multi-body dynamics across a wide range of frequencies and wave headings. This level of approximation retains sufficient accuracy for spectral-oriented studies, especially in early stage design and array optimisation [16, 43]. A visual summary of these assumptions and boundary conditions is shown in Figure 3.1.

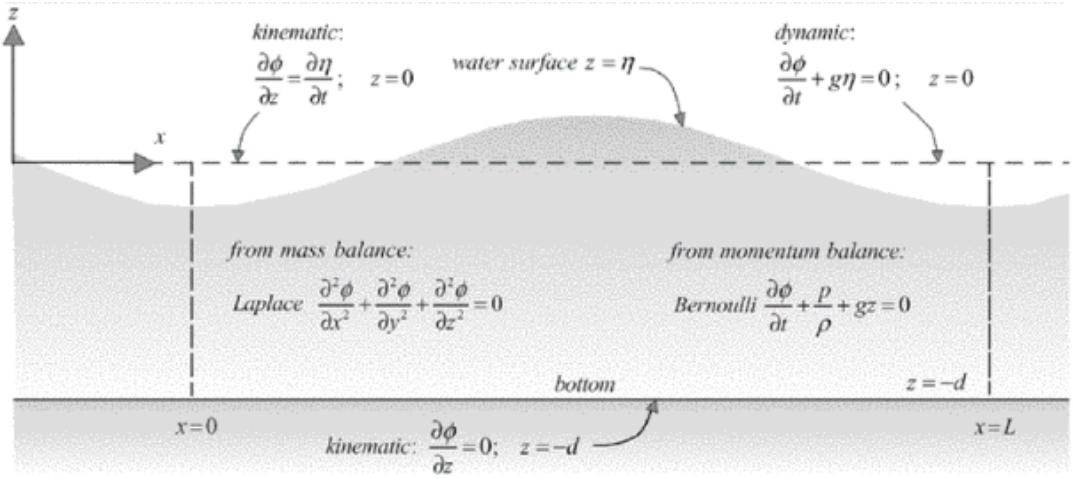

Figure 3.1: Governing conditions for linear wave theory, including Laplace's equation and boundary conditions at the seabed and free surface [44].

These relations hold under the linear wave assumptions of small amplitude relative to wavelength and depth, $H/L \ll 1$ and $H/d \ll 1$.

The present model includes the principal linear hydrodynamic components: radiation damping, added mass, hydrostatic stiffness, and frequency-dependent wave excitation. These quantities are derived from the potential formulation and depend on wave frequency and direction [16, 42]. All wave–body interactions are linear and based on first-order wave theory. Mooring effects are neglected in the governing equations but included in the model through an external stiffness matrix. Each device is assumed to remain within its linear operational range. These exclusions are justified to isolate the effects of wave–structure interaction and are common in initial array studies, particularly when mooring dynamics are not the primary focus [12, 45].

To extend the scope beyond fully linear dynamics, selected nonlinear effects are incorporated using approximate or statistical treatments. Their inclusion improves the realism of the FD formulation without significantly increasing computational cost [46, 47, 48].

All six rigid-body DOF are initially retained to capture the full response of each WEC under directional wave excitation. This includes off-axis motions such as roll, which may become relevant under oblique or broad-crested wave conditions [11, 17]. If lateral modes are found to be negligible, a reduced order model is adopted.

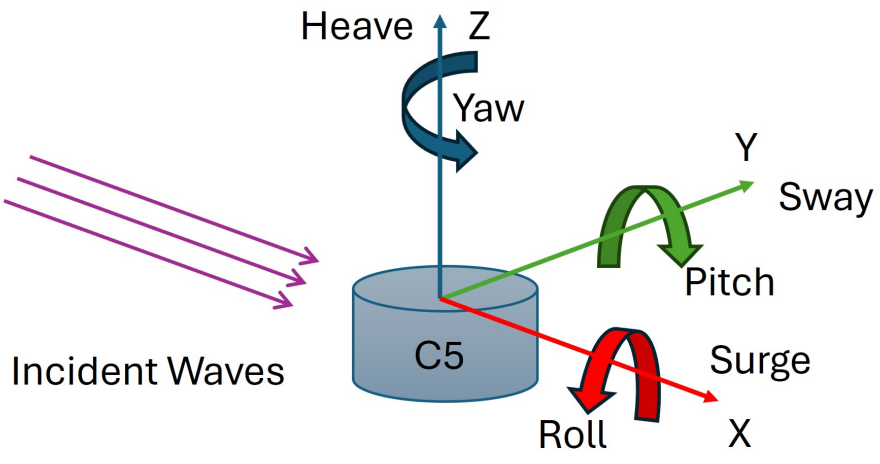

Figure 3.2: Schematic of a wave energy converter showing the six DOF.

The wave field is represented using both regular and irregular components. Regular waves are modelled as monochromatic harmonic inputs, used only for RAO and excitation-force consistency checks. Irregular seas are characterised using the JONSWAP spectrum [49], with parameters calibrated to realistic sea states.

Two types of wave representations are used in this study: regular waves and irregular unidirectional waves. Regular waves represent unidirectional seas with uniform phase and crest coherence and are used for baseline performance testing. Irregular waves, by contrast, introduce spatial variability in phase through random superposition of spectral components, reducing coherence across the array even under a fixed wave heading. This produces realistic excitation variability while remaining computationally tractable.

Figure 3.3 illustrates the distinction between the wave environments considered. Regular waves (left) propagate in a single direction with uniform phase and crest coherence. Irregular waves (right) involve multiple wave components from different phases, leading to spatially varying interaction patterns.

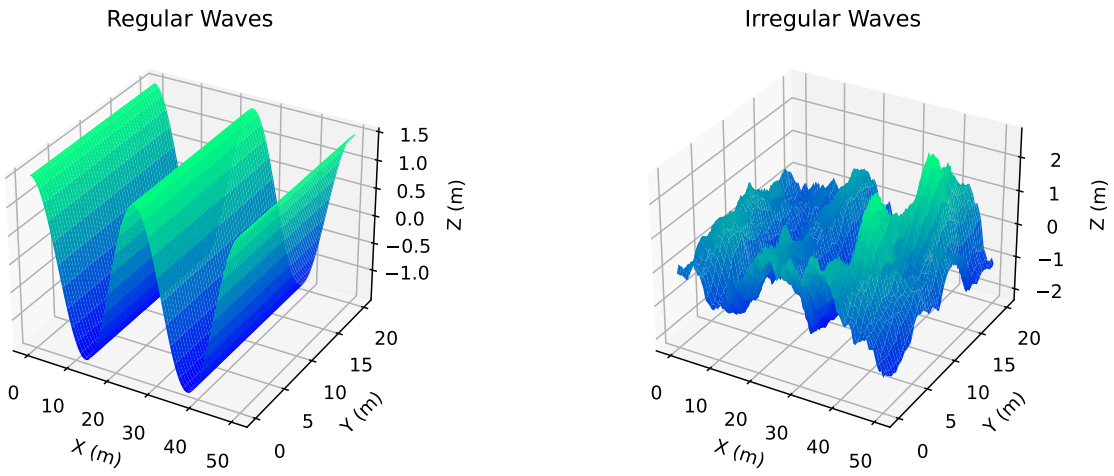

Figure 3.3: Visual comparison between regular and irregular waves.

3.2. Governing Equations in the Frequency Domain

The dynamic response of a floating WEC under wave excitation is modelled using linear potential flow theory expressed in the FD. Under the assumptions of small-amplitude oscillations and time-invariant hydrodynamic coefficients, all time-dependent quantities may be written using complex phasors,

$$\mathbf{X}(t) = \Re\{\mathbf{X}(\omega)\, e^{i\omega t}\}, \tag{3.2}$$

where $\mathbf{X}(\omega)$ denotes the complex displacement amplitude.

For a single body with six rigid-body DOF, the FD equation of motion is

$$\left[-\omega^2 \left(M + A(\omega)\right) + K + K_{\mathrm{PTO}} + i\omega \left(B(\omega) + B_{\mathrm{PTO}}\right)\right] \mathbf{X}(\omega) = \mathbf{F}_{\mathrm{exc}}(\omega), \tag{3.3}$$

where the bracketed quantity is a dynamic stiffness operator, mapping displacement to force in the FD. This operator is displacement-based and is not an impedance in the sense of Alves et al. [50].

The radiation impedance, following its definition in Alves, relates the radiation force to the velocity amplitude,

$$\widehat{\mathbf{F}}_r(\omega) = i\omega\, Z_{\mathrm{rad}}(\omega)\, \widehat{\mathbf{X}}(\omega), \qquad Z_{\mathrm{rad}}(\omega) = B(\omega) + i\omega\, A(\omega), \tag{3.4}$$

showing that impedance is force divided by velocity, while Eq. (3.3) is written in terms of force divided by displacement.

Each matrix in Eq. (3.3) is of dimension 6×6:

- M: rigid-body mass and inertia matrix,
- $A(\omega)$: added-mass matrix,
- $B(\omega)$: radiation damping matrix,
- K: hydrostatic restoring matrix,
- K_{PTO}: PTO stiffness contribution,
- B_{PTO}: linearised PTO damping,
- $\mathbf{F}_{\mathrm{exc}}(\omega)$: complex excitation force vector.

In the absence of PTO or mooring effects, the FD relation simplifies to a purely hydrodynamic dynamic stiffness operator,

$$D_{\mathrm{hydro}}(\omega) = -\omega^2 \left(M + A(\omega)\right) + K + i\omega\, B(\omega), \tag{3.5}$$

and the free response becomes

$$\mathbf{X}(\omega) = D_{\mathrm{hydro}}^{-1}(\omega)\, \mathbf{F}_{\mathrm{exc}}(\omega). \tag{3.6}$$

The RAO is then defined as

$$\mathrm{RAO}(\omega) = \frac{\mathbf{X}(\omega)}{A_{\mathrm{wave}}(\omega)}, \tag{3.7}$$

where $A_{\mathrm{wave}}(\omega)$ is the complex incident wave amplitude. The RAO describes both magnitude and phase of the displacement response and is used in performance, loading, and spectral analyses.

The RAO serves not only as a measure of dynamic amplification, but also forms the basis for absorbed power calculations. For a purely linear damping element, the absorbed power in the linear FD formulation is:

$$P_{\mathrm{abs}}(\omega) = \frac{1}{2}\, \Re\{\mathbf{X}^H(\omega)\, B_{\mathrm{PTO}}\, \mathbf{X}(\omega)\} \tag{3.8}$$

where $\mathbf{X}^H$ denotes the complex conjugate transpose of $\mathbf{X}$.

For an array of N devices, the governing equations are assembled into global matrices of size $6N \times 6N$, with off-diagonal blocks capturing hydrodynamic interactions such as radiation and diffraction coupling. These coefficients are computed using HAMS-MREL, and depend on frequency, direction, and spacing.

3.3. Nonlinear Frequency Domain Modelling

Classical FD modelling assumes linear potential flow, where all hydrodynamic forces are linearised around the mean position. This limits accuracy when nonlinear restoring, viscous, or control forces become significant. To include such effects while preserving the spectral efficiency of the FD approach, the NLFD or harmonic balance formulation is employed [14, 15, 32]. The method expresses the steady-state response as a truncated Fourier series, enforces the governing equations in a harmonic sense, and solves the resulting nonlinear algebraic system in the Fourier coefficients. This allows weak nonlinearities to be incorporated without resorting to long TD integrations.

The governing linear FD formulation for a floating body was introduced in Eq. (3.3). For a single-DOF reduction, the same dynamic-stiffness structure collapses to

$$\left[-\omega^2(M + A(\omega)) + i\omega\, B(\omega) + K\right] \mathbf{X}(\omega) = \mathbf{F}_{\mathrm{exc}}(\omega), \tag{3.9}$$

which neglects all nonlinear force contributions. The NLFD approach extends this linear FD formulation through harmonic balance.

3.3.1. Single-DOF Formulation

For a single-DOF, representing for example heave motion of an axisymmetric device, the governing TD equation can be expressed compactly as

$$g_\ell(\zeta, \dot{\zeta}, \ddot{\zeta}) - f_{\mathrm{NL}}(\zeta, \dot{\zeta}, t) - e(t) = 0, \tag{3.10}$$

where g_ℓ collects the inertia, radiation, and hydrostatic terms treated linearly, f_{NL} represents the nonlinear contributions, and $e(t)$ is the excitation force.

Under steady-periodic forcing, the displacement is approximated by a truncated Fourier expansion

$$\zeta(t) = a_0 + \sum_{n=1}^{N} [a_n \cos(n\omega t) + b_n \sin(n\omega t)], \tag{3.11}$$

where a_n and b_n are the unknown Fourier coefficients of the cosine and sine harmonics, from which the amplitude and phase of each harmonic can be derived. The same Fourier basis is used to project both the excitation and the nonlinear forces into the FD. Projecting the TD equation onto this harmonic basis yields a nonlinear algebraic system,

$$M_{\mathrm{HB}}\, \mathbf{X} - \mathbf{F}(\mathbf{X}) - \mathbf{E} = \mathbf{0}, \tag{3.12}$$

where $\mathbf{X}$ is the vector of Fourier coefficients of the displacement, $\mathbf{E}$ the excitation coefficients, and $\mathbf{F}(\mathbf{X})$ the Fourier projection of the nonlinear forces.

The matrix M_{HB} contains the frequency-dependent linear terms,

$$(M_{\mathrm{HB}})_{i,i} = -\omega_i^2[m + A(\omega_i)] + C, \qquad (M_{\mathrm{HB}})_{i,i+N} = \omega_i B(\omega_i), \qquad (M_{\mathrm{HB}})_{i+N,i} = -(M_{\mathrm{HB}})_{i,i+N}.$$

with

$$(M_{\mathrm{HB}})_{2N+1,\,2N+1} = C.$$

defining the DC component. The nonlinear projection vector is given by

$$F_i(\mathbf{X}) = \frac{2}{T}\int_0^T f_{\mathrm{NL}}(\zeta_X, \dot{\zeta}_X, t)\cos(\omega_i t)\,dt, \tag{3.13}$$

$$F_{i+N}(\mathbf{X}) = \frac{2}{T}\int_0^T f_{\mathrm{NL}}(\zeta_X, \dot{\zeta}_X, t)\sin(\omega_i t)\,dt, \tag{3.14}$$

$$F_{2N+1}(\mathbf{X}) = \frac{1}{T}\int_0^T f_{\mathrm{NL}}(\zeta_X, \dot{\zeta}_X, t)\,dt. \tag{3.15}$$

The resulting residual vector

$$\mathbf{G}(\mathbf{X}) = M_{\mathrm{HB}}\,\mathbf{X} - \mathbf{F}(\mathbf{X}) - \mathbf{E}$$

is solved iteratively using Newton–Raphson updates, ensuring convergence to the steady-state nonlinear solution. This formulation, first presented by Merigaud and Ringwood [14, 29], establishes the basis of the NLFD method.

3.3.2. Multi-DOF Extension

The single-DOF harmonic balance system generalises directly to multiple rigid-body modes. Let n_{dof} denote the number of retained DOF. Stacking the Fourier coefficients for all modes yields the nonlinear algebraic system

$$M_{\mathrm{HB}}\,\mathbf{X} - \mathbf{F}(\mathbf{X}) - \mathbf{E} = \mathbf{0}, \tag{3.16}$$

where $\mathbf{X} \in \mathbb{R}^{(2N+1)n_{\mathrm{dof}}}$ is the global vector of displacement coefficients, M_{HB} collects the linear hydrodynamic terms, $\mathbf{E}$ the excitation coefficients, and $\mathbf{F}(\mathbf{X})$ the Fourier projections of the nonlinear forces for all modes.

The off diagonal terms of M_{HB} preserve the hydrodynamic coupling between DOF, allowing, for example, pitch–heave interaction under oblique waves. The system residual is solved iteratively using the same harmonic balance procedure, with the linear FD solution providing an initial estimate. This multi-DOF formulation [15, 30], captures coupled motion dynamics and forms the foundation for array-level modelling.

3.3.3. Array Extension

The multi-DOF formulation extends naturally to multiple interacting devices. For an array of n_{dev} units, the governing system for the full set of retained harmonics can be written compactly as:

$$Z_{\mathrm{H}}(\omega_k)\,\mathbf{X}_k - \mathbf{F}_{\mathrm{NL}}(\mathbf{X}) = \mathbf{E}_k, \tag{3.17}$$

where $Z_{\mathrm{H}}(\omega_k) \in \mathbb{C}^{(n_{\mathrm{dof}}n_{\mathrm{dev}})\times(n_{\mathrm{dof}}n_{\mathrm{dev}})}$ is the complete hydrodynamic impedance matrix containing both self and interaction terms. The block structure of Z_{H} retains the off-diagonal added mass and radiation damping components that govern radiation and diffraction coupling between devices.

Nonlinear forces are evaluated locally for each device. Their Jacobian remains block diagonal,

$$\mathbf{J}_{\mathrm{NL}} = \mathrm{diag}\left(\frac{\partial \mathbf{F}_{\mathrm{NL}}^{(1)}}{\partial \mathbf{X}^{(1)}}, \ldots, \frac{\partial \mathbf{F}_{\mathrm{NL}}^{(n_{\mathrm{dev}})}}{\partial \mathbf{X}^{(n_{\mathrm{dev}})}}\right),$$

reflecting the assumption of weak nonlinear coupling between devices. The total harmonic balance residual of the array becomes

$$\mathbf{G}(\mathbf{X}) = Z_{\mathrm{H}}\mathbf{X} - \mathbf{F}_{\mathrm{NL}}(\mathbf{X}) - \mathbf{E} = \mathbf{0}. \tag{3.18}$$

This structure preserves full hydrodynamic interaction while treating nonlinearities as locally acting forces. Compared with mixed time–frequency approaches [32, 51], this formulation remains purely spectral and fully consistent within the FD, enabling unified treatment of multi-DOF and multi-device arrays within a single nonlinear algebraic system.

The formulation above establishes the theoretical foundation for the nonlinear solver developed in Chapter 4, where the implementation details, convergence criteria, and parameter selections are described.

3.4. Extension of the Nonlinear Frequency Domain Methodology

The NLFD framework developed in this thesis extends the formulations of Merigaud and Ringwood [14, 29] and Wei et al. [32, 51] to enable coupled multi-DOF, multi-device simulations under irregular seas. Merigaud and Ringwood introduced the harmonic balance formulation for single-DOF WECs, expressing displacement and nonlinear forces in a truncated Fourier basis and solving the resulting algebraic system with Newton–Raphson iteration. Their analytic Jacobian ensured rapid convergence for smooth nonlinearities such as cubic stiffness or quadratic damping, but the approach was restricted to periodic excitation, single-DOF, and differentiable nonlinear functions.

Wei and co-workers generalised the framework to multi-device arrays through a mixed time–frequency formulation. Hydrodynamic coupling was retained in the FD, while nonlinear PTO forces were computed in the TD via a Lagrange multiplier update. Irregular seas were represented by dividing the time series into short, overlapping quasi-stationary windows, each solved independently. This made large array simulations tractable but lost strict FD consistency, required inter-window reconstruction, and limited harmonic coupling across the spectrum. Their array model included only a single active DOF (heave) per device, which restricted the ability to capture rotational coupling and cross-mode interactions within the array.

The present formulation retains a fully spectral treatment within each irregular-sea realisation, applying the NLFD scheme separately to multiple independent 120-second segments rather than using mixed time–frequency windows. Nonlinear effects are evaluated in the TD using the reconstructed motion and projected into the Fourier basis at each Newton–Raphson iteration, maintaining FD consistency of the linear hydrodynamics. A full Newton–Raphson iteration is applied to the global residual vector, using a block diagonal Jacobian that captures local nonlinear sensitivities while remaining computationally scalable. Nonlinear forces act locally on each device, while hydrodynamic coupling between all bodies and modes is retained through the full impedance matrix $Z_{\mathrm{H}}(\omega)$. This ensures that energy exchange through radiation and diffraction remains global, whereas hydrostatic and PTO interactions remain device specific.

In addition, the method extends previous single mode array formulations to a full multi-DOF representation of each device, allowing simultaneous solution of multi-DOF dynamics within the coupled array. The full hydrodynamic impedance matrix preserves inter-device coupling across all active DOF, enabling unified multi-DOF, multi-device simulations within a single nonlinear system. This extension combines the efficiency of the original harmonic balance method with the generality of Wei's array formulation, providing a self-consistent FD framework capable of resolving nonlinear response behaviour and array interactions in realistic irregular seas. This is achieved by embedding Wei's multi-device hydrodynamic impedance structure directly into the harmonic balance system, while evaluating nonlinear forces in the TD and projecting them into the Fourier basis during each Newton–Raphson update. In this way, array-scale coupling and nonlinear effects are solved simultaneously in a single FD without segmenting the sea state.

3.5. Approximate Nonlinear Effects in Frequency Domain Modelling

While the underlying formulation is linear, several nonlinear effects play a significant role in the performance and control of WECs. Real-world constraints cannot be neglected, especially under large-amplitude or broadband wave conditions. However, fully nonlinear TD models are often computationally prohibitive for array-scale studies.

This thesis explores the theoretical basis for incorporating selected nonlinear effects within a weakly NLFD formulation. The nonlinearities are described mathematically and, wherever possible, their influence is incorporated through TD evaluation and FD projection within the NLFD scheme, avoiding the need for full TD simulations over long time horizons. This approach aims to balance physical fidelity with computational efficiency, while acknowledging the inherent limitations of linear FD models. The following subsections present the theoretical models for nonlinear PTO and hydrodynamic effects, with implementation details provided in the methodology, Chapter 4.

3.5.1. Motivation for Including Nonlinearities

FD modelling offers an efficient and analytically tractable framework for evaluating WEC dynamics. However, its inherent linearity limits its ability to capture nonlinear physical effects that arise in real ocean conditions. These effects become particularly relevant for performance assessment under energetic wave spectra and for the accurate prediction of system response in irregular seas [29, 52, 53]. In contrast, TD modelling naturally accommodates nonlinear forces, but suffers from higher computation cost and limited scalability when applied to full arrays [52, 53]. Selected nonlinear effects are approximated and introduced into the system equations through analytical or empirical corrections, based on their demonstrated impact on WEC behaviour.

PTO saturation arises from mechanical limitations in the PTO mechanism, particularly under high loading. This effect cannot be represented using a constant damping coefficient, and its exclusion leads to overestimation of response amplitudes and absorbed power in linear models [54]. Restoring forces become nonlinear when the water plane area

of submerged volume varies significantly with displacement, which occurs in large wave conditions or for devices with rounded geometries [53, 54]. Finally, viscous drag introduces a quadratic dependence on velocity that is absent in linear potential flow theory. Although often neglected in FD formulations, drag has been shown to influence both response amplitude and spectral energy distribution, particularly in energetic seas.

While these effects are straightforward to implement in TD through direct force computation, such an approach is not tractable for array-scale studies requiring many simulations. Approximate inclusion in the FD framework enables retention of the linear system structure while capturing key nonlinear phenomena. This balance between accuracy and computational efficiency motivates the semi-empirical modelling strategies developed in the following subsections.

3.5.2. Nonlinear PTO Saturation

In real WEC systems, the PTO hardware is subject to physical constraints such as force limits, velocity limits, and efficiency losses. These nonlinearities become important under energetic sea states or broadband excitation. Several studies emphasise that failing to account for such effects can lead to overestimation of absorbed power. Tan et al. [25] show that neglecting PTO force constraints yields overly optimistic predictions, while Wei et al. [32] demonstrate that nonlinear PTO models improve accuracy in dense arrays where local hydrodynamic interactions are significant.

In conventional FD formulations, the PTO force is typically represented as

$$F_{\mathrm{PTO,lin}} = -B_{\mathrm{PTO}}\,\dot{x}, \tag{3.19}$$

where $\dot{x}$ is the complex velocity amplitude. This linear model assumes unbounded velocity and force capability and therefore cannot capture the reduction in effective damping that occurs when the PTO hardware approaches its operational limits.

Nonlinear saturation models modify this behaviour by replacing the proportional law with a smooth limiting function that transitions the PTO force toward a maximum admissible value. A commonly used example in the literature is the hyperbolic tangent formulation:

$$F_{\mathrm{PTO}} = F_{\max}\tanh\!\left(\frac{-B_{\mathrm{PTO}}\,\dot{x}}{F_{\max}}\right), \tag{3.20}$$

where $F_{\max}$ is the maximum achievable PTO force. The $\tanh$ function provides a differentiable soft-saturation mechanism that is well suited to FD solvers, as noted by Hansen [55]. Such models suppress unrealistic force growth at large velocities while preserving linear behaviour for small motions.

The present thesis does not employ this saturation law in the nonlinear solver, but the concept is included here for completeness and to position the model relative to existing nonlinear PTO approaches in the literature. The velocity-limiting PTO model actually used in the simulations is described in Section 4.6.1.

3.5.3. Nonlinear Hydrodynamics

Nonlinear hydrodynamic effects are important for accurately predicting WEC performance in large amplitude or broadband seas. In this study, two contributions are included: nonlinear restoring[1] and viscous drag. Both are absent in conventional FD formulations, which assume constant hydrostatic stiffness and neglect viscous dissipation, yet they can significantly alter the response of point absorbers under energetic conditions. These representations remain approximate and do not capture higher-order free-surface or viscous phenomena.

Nonlinear restoring arises from the fact that buoyancy depends on the instantaneous submerged volume rather than a constant water plane stiffness. For devices such as the CPO C5, the restoring force departs from the linear spring assumption as the buoy approaches full submergence or emergence. This effect can reduce unrealistic resonance amplification predicted by linear models. In the present formulation, restoring is computed as a nonlinear function of displacement, capturing the dependence on submerged geometry, before being reprojected into the frequency basis within the NLFD scheme.

Viscous drag represents momentum losses due to flow separation and vortex shedding, which are not accounted for in potential flow theory. Drag is typically expressed as quadratic in velocity,

$$F_{\mathrm{drag}}(t) = -\tfrac{1}{2}\rho C_d A|\dot{x}(t)|\dot{x}(t), \tag{3.21}$$

where ρ is water density, C_d is a drag coefficient, A is a reference area, and $\dot{x}(t)$ is the instantaneous velocity. Within NLFD, this nonlinear drag force is evaluated in the TD using the reconstructed motion and then projected back into the FD.

[1] In this thesis, 'restoring' refers specifically to forces that vary with the submerged volume of the device. This is distinct from the linearised hydrostatic stiffness typically used in FD models.

Together, nonlinear restoring and viscous drag provide a more realistic description of array dynamics while preserving the computational efficiency of FD analysis. Their inclusion ensures that the most significant nonlinear hydrodynamic effects are represented without requiring full TD simulations.

3.6. Hydrodynamic Coefficients from HAMS-MREL

Hydrodynamic coefficients, including added mass, radiation damping, and excitation, are fundamental for modelling the dynamic response of WECs. In this work, these coefficients are obtained using the open source BEM solver HAMS-MREL, which efficiently solves the diffraction and radiation problems for multiple floating bodies in the FD [16]. HAMS-MREL is capable of handling complex multi-body interactions and has been validated against both semi-analytical solutions and established commercial solvers, demonstrating high accuracy and computational efficiency. The results of the elaborate comparison can be seen in Section 2.4.

The solver requires as input the geometry of the floating bodies (provided as mesh files), environmental parameters such as the water depth, wave frequencies, and the headings, and a control file specifying simulation settings. These inputs can be generated and managed using custom scripts, such as `HAMSMultiInput.py`, which automates the creation of input files and output directories. The output of HAMS-MREL includes the hydrodynamic coefficients and exciting forces for all bodies, including interaction terms, which are essential for constructing the equations of motion and computing the RAO. Post-processing scripts, such as `post_processing_HAMS_multibodies.py`, facilitate the extraction and analysis of these results, enabling the calculation of RAO and supporting further device performance assessment.

The hydrodynamic coefficients used here are obtained from HAMS-MREL, whose accuracy and robustness has been demonstrated through validation against commercial BEM solvers, as discussed in Section 2.4. These coefficients form the basis for the dynamic response calculations carried out in this thesis.

3.7. Summary

This chapter established the theoretical basis for the FD modelling of WEC arrays. It began by outlining the physical assumptions and governing equations derived from linear potential flow theory. The framework models wave–structure interactions using small amplitude, steady-state approximations, enabling the use of superposition and harmonic analysis.

The hydrodynamic forces are computed using a BEM approach via the HAMS-MREL solver. The model initially retains all six rigid-body DOF for each WEC, with the option of reduced order representations when certain modes are negligible.

To enhance physical realism, weakly nonlinear effects are incorporated within the NLFD framework. These include nonlinear restoring, viscous drag, and PTO saturation. Each contribution is evaluated in the TD from the reconstructed motion and projected into the Fourier basis at each Newton-Raphson iteration, maintaining the FD structure of the linear hydrodynamics.

The chapter also introduced the representation of different wave environments, including regular and irregular waves, which form the external forcing conditions for array simulations. For arrays, the formulation extends naturally to global system matrices that account for hydrodynamic interactions between multiple devices.

Overall, the chapter provides the theoretical foundation for the modelling pipeline developed in Chapter 4. The transition from linear potential flow to a weakly NLFD formulation establishes the basis for analysing hydrodynamic interactions, spacing effects, nonlinear responses, and directional sensitivity in large arrays of WECs.

4

Methodology

This study evaluates the spectral and time response of a WEC array subjected to realistic irregular seas through a weakly NLFD modelling approach. The array configuration is based on the staggered 2×7 layout proposed by CPO, with representative device spacings of 5D, 10D, and 15D, where D is the device diameter. As shown in Figure 4.1, the figure illustrates only the geometric arrangement; hydrodynamic interaction is expected to be strongest at intermediate spacings and under oblique incidence, consistent with the findings summarised in Section 2.1.

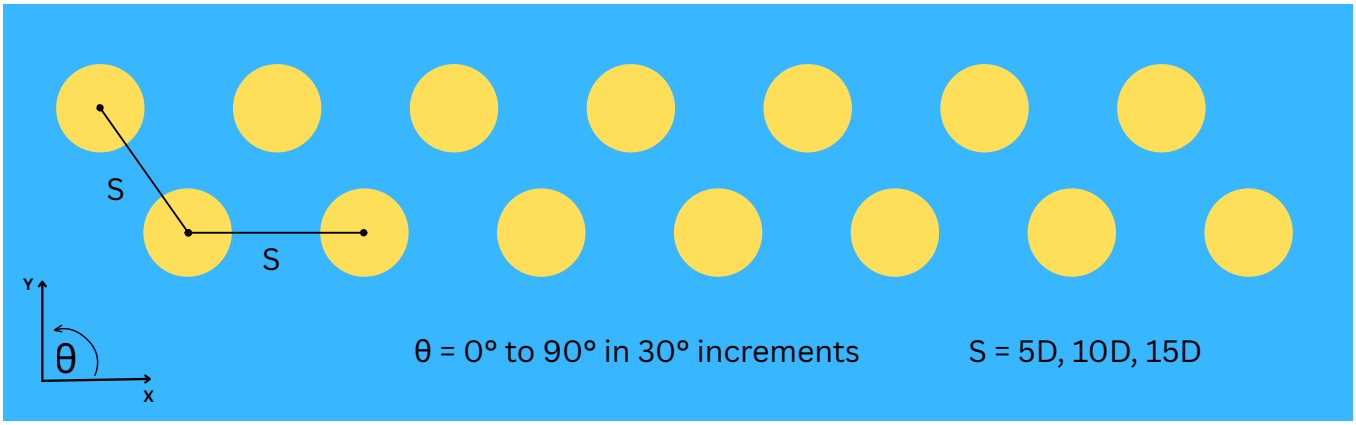

Figure 4.1: Visualisation of the staggered 2×7 WEC array layout, with device spacings of 5D, 10D, and 15D.

The methodology begins by defining the array geometry and the spacing configurations considered in this study. Representative sea states are then selected from a long term hindcast dataset, from which scatter diagrams and spectral inputs are constructed using the JONSWAP formulation. These spectra provide the irregular wave conditions used throughout the analysis.

A reduction to the dominant rigid-body DOF is introduced before performing a convergence study with the HAMS-MREL solver to obtain the hydrodynamic coefficients required for the linear and nonlinear models. After convergence is established, the baseline linear FD formulation is implemented and used to compute response spectra for single and multiple devices.

Nonlinear effects are incorporated by introducing the nonlinear PTO, hydrostatic, and viscous models, followed by the weakly nonlinear FD implementation described in Section 3.3. The PTO parameters are then assessed through an impedance based reference, a scaled parameter sweep, and the final parameter selection.

Power assessment is carried out through segmentation and averaging, spectral density analysis, the array power interaction factor, the device level power ratio, and a TD reconstruction of the absorbed power. The methodology concludes with validation of the nonlinear predictions and a summary of the computational setup.

4.1. Array Layout and Spacing Configurations

Three inter-device spacings, $S \in \{5D,\ 10D,\ 15D\}$, are considered to examine how hydrodynamic coupling strength scales with separation distance. Previous studies (Section 2.1) indicate that compact arrays enhance near field radiation and diffraction effects, while larger spacings lead to quasi-independent behaviour. Here, the same pattern is explored within the developed nonlinear framework to quantify how these interactions evolve once nonlinear forces are included.

At $S = 5D$, strong constructive and destructive interaction are expected, producing high spectral modulation and reduced mean power. At $S = 10D$, partial coupling should remain, yielding smoother spectral responses and moderate interaction factors. At $S = 15D$, hydrodynamic coupling is expected to diminish, with each device approaching the single-device limit [24].

This study therefore treats spacing not as a geometric variable alone but as a control on the transition from coupled to independent array dynamics.

4.2. Wave Data and Spectral Characterisation

4.2.1. Wave Data Source

The scatter diagram of significant wave height H_s versus the energy period T_e was constructed using the 30-year (1992–2021) ECHOWAVE hindcast dataset, which provides high resolution, hourly wave records tailored for applications in North Atlantic European waters. The dataset provides detailed characterisation of sea states at the coastal shelf ($d > 200\,\text{m}$), with a spatial resolution of approximately 2.3 km and hourly resolution [56]. The selected data point, located at $41.460°\text{N},\ 8.850°\text{W}$, was identified for its proximity to the target coordinates $41.459°\text{N},\ 8.842°\text{W}$, as referenced in the Tethys project database [57].

Data extraction, processing, and statistical analysis were performed using Python and the pandas library, enabling efficient handling of the large dataset (262,800 hourly records) and robust computation of occurrence frequencies for each bin. For each record, the peak period T_p was calculated directly from the peak frequency F_p using $T_p = 1/F_p$, and the energy period T_e was then estimated using a gamma dependent relation appropriate for JONSWAP-type spectra:

$$T_e = T_p \cdot \frac{4.2 + \gamma}{5 + \gamma} \tag{4.1}$$

In the numerical model, the JONSWAP spectrum is parametrised using T_p, T_e is used only for scatter diagram classification.

4.2.2. Scatter Diagram Construction

The ranges of H_s and T_e were partitioned into discrete bins, with bin widths selected to balance statistical resolution and interpretability. Each data point was systematically assigned to its corresponds bin, and the frequency of occurrence within each bin was tallied. The resulting matrix of bin counts was visualised as a scatter diagram, with the frequency of each sea state combination indicated by the colour gradient.

The scatter diagram allows for the identification of both the most common sea states, which dominate the site's wave climate, and the less frequent but potentially more extreme conditions. By highlighting regions of high occurrence frequency ("hotspots"), the scatter diagram supports the selection of representative sea states for further analysis and simulation.

The full scatter diagram is provided in Appendix B.

4.2.3. Spectral Representation Using JONSWAP

Representative irregular sea states are constructed to reproduce realistic wave excitation for the numerical model. Each sea state is defined by a significant wave height H_s and an energy (or equivalent peak) period T_e, obtained from the long-term scatter diagram shown in Appendix B. These parameters specify both the energy content and the spectral shape of the corresponding sea condition.

Four representative sea states are extracted from the highest probability regions of the scatter diagram to provide a balanced set of test conditions. They are selected such that both wave height and period are systematically varied while remaining within the most frequently occurring envelope of the local climate:

1. **Sea State I**: $H_s = 1.0$ m, $T_e = 9.0$ s
2. **Sea State II**: $H_s = 2.0$ m, $T_e = 9.0$ s
3. **Sea State III**: $H_s = 2.0$ m, $T_e = 11.0$ s
4. **Sea State IV**: $H_s = 3.0$ m, $T_e = 11.0$ s

This selection allows targeted assessment of nonlinear and spectral effects:

- States I $\rightarrow$ II isolate the influence of increasing wave amplitude at fixed spectral shape, testing amplitude driven nonlinearities.
- States II $\rightarrow$ III maintain equal H_s but vary T_p, isolating period dependent hydrodynamic and control effects.
- States III $\rightarrow$ IV extend the forcing toward the upper limit of the NLFD solver's convergence range [30], exploring the combined effect of large H_s and long T_p on motion amplitude and solver stability.

All four sea states lie along the main probability ridge of the measured wave climate, ensuring that the analysis remains representative of realistic operating conditions while still spanning the nonlinear regime relevant for power absorption and solver performance evaluation.

The spectrum is an extension of the Pierson–Moskowitz spectrum, augmented by a peak enhancement factor γ to model the spectral sharpness observed in fetch limited seas. Following the approach in [58], who derived a best fit value based on 30 years of hindcast spectra for this location, a constant value of $\gamma = 1.82$ is adopted throughout. The one-dimensional spectral density function $S(\omega)$ is defined by:

$$S(\omega) = \alpha\, g^2\, \omega^{-5} \exp\!\left(-\frac{5}{4}\left(\frac{\omega_p}{\omega}\right)^4\right) \gamma^{\exp\left(-\frac{(\omega-\omega_p)^2}{2\sigma^2\omega_p^2}\right)} \tag{4.2}$$

where α is a scaling factor determined by the target H_s and ω_p is the peak angular frequency. The width parameter σ is piecewise-defined to reflect the spectral asymmetry around the peak.

$$\sigma = \begin{cases} 0.07, & \text{for } \omega \leq \omega_p \\ 0.09, & \text{for } \omega > \omega_p \end{cases} \tag{4.3}$$

Each spectrum is evaluated on a range wide enough to include most energy while keeping computational cost low:

$$\omega_i \in \left[0.5 \cdot \omega_{p,\min},\ 3 \cdot \omega_{p,\max}\right], \qquad N_\omega = 300, \tag{4.4}$$

The mean direction is set head on to the array ($\theta_p = 90°$), and the discrete bins used in the hydrodynamic solver are

$$\theta_j \in [0°, 30°, 60°, 90°], \tag{4.5}$$

These four headings were chosen to balance directional coverage with computational feasibility, capturing both end-member and intermediate incidence angles. This resolution is sufficient to characterise the array's directional response.

The target sea states were defined using JONSWAP spectra for $T_p = 9$ s and $T_p = 11$ s, as shown in Figure 4.2.

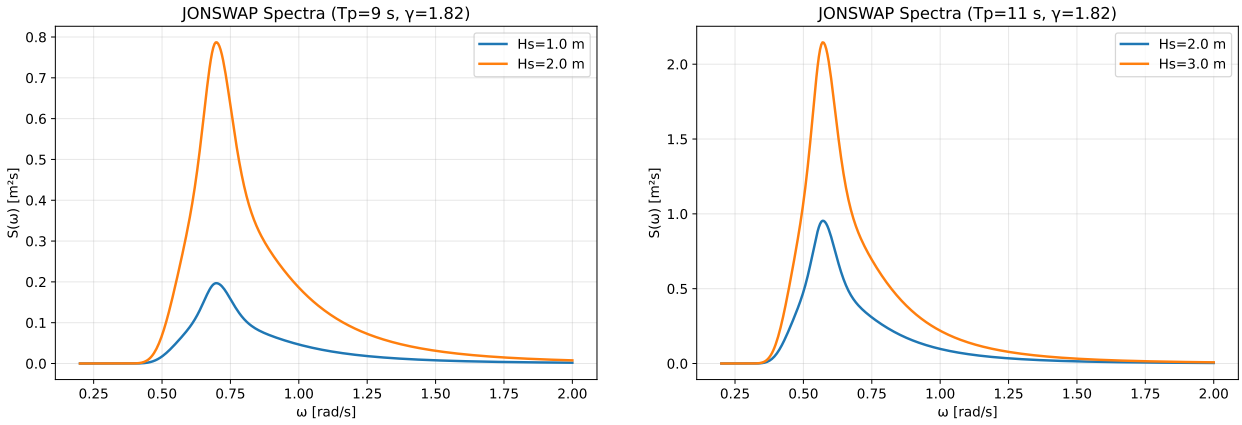

(a) JONSWAP spectra for $T_p = 9$ s with $H_s = 1$ m and 2 m.

(b) JONSWAP spectra for $T_p = 11$ s with $H_s = 2$ m and 3 m.

Figure 4.2: Comparison of JONSWAP spectra for the four validation sea states used in this study.

4.3. DOF Reduction and Justification

The full radiation–diffraction model obtained from the HAMS-MREL solver initially resolves all six rigid-body DOF. However, for subsequent spectral analyses the dimensionality of the system is reduced to three primary modes: heave, roll, and pitch. This simplification significantly lowers computational complexity in the FD implementation while preserving the dominant dynamical characteristics of the WEC response.

This choice reflects the coordinate system used in this thesis, where the hinge point is taken at the seabed. In this formulation, surge and sway forces are incorporated into pitch and roll, respectively, while yaw remains negligible for axisymmetric devices. A schematic of the full six-DOF is shown in Figure 3.2.

Figure 4.3 illustrates the CPO WEC modelled in three DOF about the seabed hinge point. Surge and sway motions are implicitly represented through the rotational modes of pitch and roll, while yaw is omitted. This reduced-order model forms the basis for all subsequent FD and spectral analyses presented in this work.

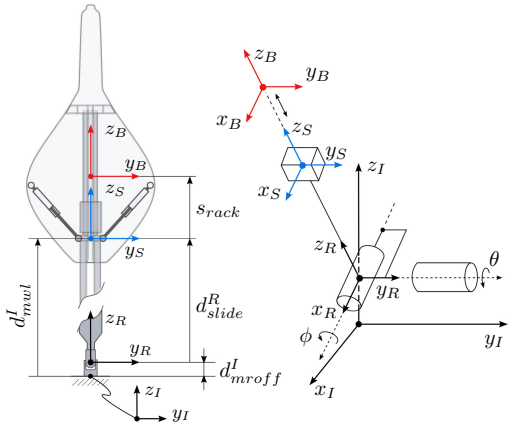

Figure 4.3: Three DOF representation of the CPO WEC modelled about the seabed hinge point [59].

4.4. Convergence Study

A convergence study was performed using HAMS-MREL to evaluate the sensitivity of hydrodynamic coefficients to panel discretisation. Five mesh resolutions were tested: 537, 747, 1222, 2342, and 4185 panels. To eliminate irregular frequencies, a water plane with 195 horizontal planes was included in all models. Representative mesh views for all resolutions are provided in Appendix C.

The convergence study was performed on a single-device subjected to incident waves propagating along the x-direction. Under this unidirectional forcing, only surge, heave, and pitch receive non-zero excitation. Sway and roll remain identically zero in this configuration, since they are not excited by waves travelling strictly along x, and yaw is omitted because the device geometry is axisymmetric.

For each DOF, added mass, radiation damping, and excitation force characteristics were evaluated up to $\omega = 5\,\mathrm{rad\,s^{-1}}$. However, only the subset of frequencies defined by Eq. (4.4) is relevant for the actual simulation campaign. Frequencies above approximately $3\,\mathrm{rad\,s^{-1}}$ are included in the convergence plots for completeness but are excluded from relative error calculations and will not influence the simulation.

It is important to note that hydrodynamic coefficients tend to asymptotically approach zero at higher frequencies. In this region, even small absolute differences between meshes can produce large relative errors due to division by very small reference values. These artefacts are numerically correct but physically insignificant for the operating range of the device, and can misleadingly exaggerate mesh sensitivity if included. To avoid this, average relative errors are only computed within the range $\omega \leq 3\,\mathrm{rad\,s^{-1}}$, which encompasses all relevant wave energy for the site-specific sea states.

The average relative error in added mass and radiation damping for each mesh was computed relative to the finest mesh (4185 panels). Results are summarised in Tables 4.1.

Table 4.1: Average relative errors (%) in added mass and radiation damping for each DOF, computed for $\omega \leq 3\,\mathrm{rad\,s^{-1}}$.

(a) Added Mass

Panels	DOF 1	DOF 3	DOF 5
537	0.44	1.23	1.21
747	0.23	0.74	0.72
1222	0.11	0.31	0.30
2342	0.05	0.07	0.07

(b) Radiation Damping

Panels	DOF 1	DOF 3	DOF 5
537	1.22	0.69	0.76
747	0.82	0.52	0.52
1222	0.36	0.38	0.37
2342	0.19	0.05	0.05

Although the 747-panel mesh offers slightly improved accuracy, the marginal gain comes at a significantly increased computational cost. For array simulations involving a half CorPack of 14 devices, the difference of 210 panels per WEC leads to 2940 additional panels per simulation. As the 537-panel mesh already maintains average errors below $1.25\,\%$, it is selected as the baseline resolution for all subsequent FD simulations.

All convergence plots and full results are provided in Appendix D.

4.5. Baseline Linear Frequency Domain Implementation

The baseline solver implements the linear impedance formulation derived in Chapter 3. Hydrodynamic coefficients $A(\omega)$, $B(\omega)$, and $\mathbf{F}_{\mathrm{exc}}(\omega)$ are imported directly from the HAMS-MREL outputs, and the complex response vector $\boldsymbol{\zeta}(\omega)$ is obtained using Eq. (3.3). This produces the classical frequency-response RAOs and forms the foundation for the nonlinear extensions introduced in Section 3.3.

A spatially uniform incident wave elevation is applied as the global driving input across the array. All devices therefore experience the same incoming wave amplitude and phase, providing a consistent reference frame for inter-device comparison. The excitation force for each WEC, however, is taken directly from the HAMS-MREL solution and therefore remains device-specific. This includes all local diffraction and radiation contributions arising from the array geometry, so each device receives its own complex $\mathbf{F}_{\mathrm{exc},i}(\omega)$ while still being forced by the same global incident wave component.

This setup isolates hydrodynamic interactions at the array-scale while avoiding artificial phase differences between devices. It should therefore be interpreted as representing the deterministic limit of array coherence under a spatially uniform sea state.

4.6. Nonlinear Force Models

To capture nonlinear behaviour while retaining the efficiency of the NLFD formulation, additional physical effects are introduced in the TD model and subsequently projected into the FD within the NLFD solver. The nonlinearities considered include velocity-limited PTO damping, geometry dependent restoring forces, and quadratic viscous drag.

4.6.1. Nonlinear PTO Dynamics

In practical devices, the PTO is constrained by both mechanical and electrical limits. A purely linear damping law,

$$F_{\mathrm{PTO,lin}}(t) = -B_{\mathrm{PTO}}\,\dot{\zeta}(t), \tag{4.6}$$

assumes unrestricted relative heave velocity and therefore overestimates absorbed power under energetic sea states. To represent finite actuation rates more realistically, the present implementation applies a smooth velocity-limiting law rather than direct force saturation.

At each time step the heave velocity is first clamped to the admissible range

$$\dot{\zeta}_{\mathrm{eff}}(t) = \mathrm{clip}\Big(\dot{\zeta}(t), -v_{\mathrm{lim}},\, v_{\mathrm{lim}}\Big)\,,$$

and the damping force is modified using a soft-saturation function:

$$F_{\mathrm{PTO}}(t) = -B_{\mathrm{PTO}}\,v_{\mathrm{lim}}\,\tanh\!\left(\frac{\dot{\zeta}_{\mathrm{eff}}(t)}{v_{\mathrm{lim}}}\right) + B_{\mathrm{PTO}}\,\dot{\zeta}_{\mathrm{eff}}(t). \tag{4.7}$$

For small velocities $|\dot{\zeta}| \ll v_{\mathrm{lim}}$ the hyperbolic tangent expands linearly and the formulation collapses to the classical damping law. As the velocity approaches the admissible limit, the effective damping coefficient decreases smoothly, reflecting the physical reduction in control authority at large piston speeds. This regularised form is differentiable and therefore compatible with Newton-Raphson iteration, while reproducing the intended soft-saturation behaviour.

4.6.2. Hydrostatic and Viscous Nonlinearities

In addition to PTO saturation, nonlinear restoring and drag forces arise from geometry dependent hydrostatics and viscous dissipation. These effects are represented using lookup tables derived from the buoy geometry and evaluated dynamically during time stepping.

Hydrostatic Geometry and Lookup Tables

The displaced volume $V(z)$, water plane area $A(z)$, and lateral projected area $A_{\mathrm{rot}}(z)$ are obtained from smooth polynomial fits to the device geometry exported from MATLAB. At any absolute vertical coordinate z, the instantaneous hydrostatic quantities are evaluated from these relationships and stored as lookup functions:

$$V_{\mathrm{lookup}}(z_{\mathrm{rel}}), \qquad A_{\mathrm{lookup}}(z_{\mathrm{rel}}), \qquad A_{\mathrm{rot,lookup}}(z_{\mathrm{rel}}),$$

where $z_{\mathrm{rel}} = z - z_{\mathrm{eq}}$ is the displacement relative to the static equilibrium position.

The equilibrium offset z_{eq} is obtained by solving

$$\rho g\, V_{\mathrm{lookup}}(z_{\mathrm{eq}}) = mg - F_0, \tag{4.8}$$

with F_0 the static PTO preload. The equilibrium water plane defines an effective body radius

$$R_{\mathrm{eq}} = \sqrt{\frac{A_{\mathrm{lookup}}(z_{\mathrm{eq}})}{\pi}}, \tag{4.9}$$

and the reference geometry is characterised by the absolute coordinates of the centre of gravity

$$\mathbf{r}_G = [x_G,\, y_G,\, z_G]^{\mathrm{T}}.$$

Nonlinear Force Evaluation

At each time step, the total nonlinear force acting on every active DOF is computed as the sum of hydrostatic restoring, viscous drag, and PTO contributions.

Heave.

$$F_{\mathrm{b}}(t) = \rho g\, V_{\mathrm{lookup}}(z(t)), \qquad F_{\mathrm{lin}}(t) = (mg - F_0) + k_h\,[z(t) - z_{\mathrm{eq}}], \qquad k_h = \rho g\, A_{\mathrm{lookup}}(z_{\mathrm{eq}}), \tag{4.10}$$

$$F_{\mathrm{rest}}(t) = F_{\mathrm{b}}(t) - F_{\mathrm{lin}}(t), \qquad \frac{\partial F_{\mathrm{rest}}}{\partial z} = \rho g\, A_{\mathrm{lookup}}(z(t)) - k_h. \tag{4.11}$$

Viscous damping is represented by a Morison-type quadratic drag:

$$F_{\mathrm{drag}}(t) = -\tfrac{1}{2}\rho C_d A_{\mathrm{lookup}}(z(t))\,\dot{z}(t)\,|\dot{z}(t)|, \qquad \frac{\partial F_{\mathrm{drag}}}{\partial \dot{z}} = -\rho C_d A_{\mathrm{lookup}}(z(t))\,|\dot{z}(t)|. \tag{4.12}$$

Roll and Pitch. For the rotational modes, the restoring moment is evaluated from the instantaneous water plane area using a fixed lever arm L_{anchor}:

$$\begin{aligned} M_{\mathrm{rest}}(t) &= -\rho g\, A_{\mathrm{lookup}}(z_{\mathrm{heave}}(t))\, L_{\mathrm{anchor}} \sin\theta(t), \\ \frac{\partial M_{\mathrm{rest}}}{\partial \theta} &= -\rho g\, A_{\mathrm{lookup}}(z_{\mathrm{heave}}(t))\, L_{\mathrm{anchor}} \cos\theta(t), \end{aligned} \tag{4.13}$$

Viscous rotational damping follows the same quadratic form:

$$\begin{aligned} M_{\mathrm{drag}}(t) &= -\tfrac{1}{2}\rho C_{d,\theta} A_{\mathrm{rot,lookup}}(z_{\mathrm{heave}}(t))(L_{\mathrm{anchor}}\dot{\theta})|L_{\mathrm{anchor}}\dot{\theta}|\, L_{\mathrm{anchor}}, \\ \frac{\partial M_{\mathrm{drag}}}{\partial \dot{\theta}} &= -\rho C_{d,\theta} A_{\mathrm{rot,lookup}}(z_{\mathrm{heave}}(t)) L_{\mathrm{anchor}}^2 |L_{\mathrm{anchor}}\dot{\theta}|. \end{aligned} \tag{4.14}$$

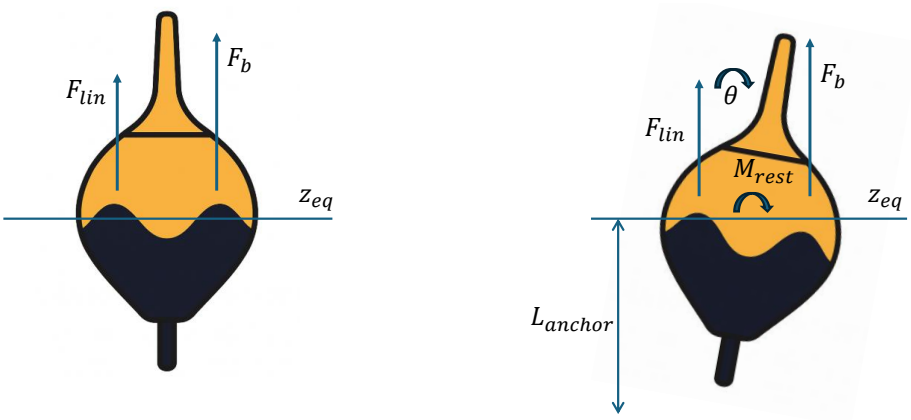

Figure 4.4: Schematic representation of the restoring force and moment evaluation used in this work. Left: heave restoring forces showing buoyant force F_{b} and linearised component F_{lin} about the equilibrium waterline z_{eq}. Right: roll/pitch restoring moment M_{rest} acting through the lever arm L_{anchor} under rotation θ.

Assembly and Jacobian. The total nonlinear force or moment for each mode is then

$$F_{\mathrm{NL}}(t) = F_{\mathrm{rest}}(t) + F_{\mathrm{drag}}(t) + F_{\mathrm{PTO}}(t), \tag{4.15}$$

and the partial derivatives

$$\frac{\partial F_{\mathrm{NL}}}{\partial z}, \qquad \frac{\partial F_{\mathrm{NL}}}{\partial \dot{z}},$$

are incorporated directly into the Jacobian of the harmonic balance solver, ensuring that the sensitivities of nonlinear restoring, drag, and PTO effects are fully captured.

4.7. Nonlinear Frequency Domain Implementation

The NLFD solver developed in this work implements the harmonic balance formulation introduced in Section 3.3. The procedure numerically solves the nonlinear residual system for the steady-state response of each WEC and array configuration.

The implementation follows four main stages:

1. **Hydrodynamic data preparation:** Added mass, radiation damping, and excitation coefficients for all devices and wave headings are imported from the HAMS-MREL solver. These frequency-dependent quantities are interpolated over the discrete frequency set defined in Eq. (4.4).
2. **Fourier representation and initialisation:** The linear FD solution provides the initial guess for the Fourier coefficients of motion. Nonlinear forces are computed in the TD from the reconstructed displacements and velocities, and then reprojected into the frequency basis.

3. **Iterative solution:** The residual system

$$\mathbf{G}(\mathbf{X}) = Z_{\mathrm{H}}\mathbf{X} - \mathbf{F}_{\mathrm{NL}}(\mathbf{X}) - \mathbf{E}$$

is solved using Newton–Raphson updates. Nonlinear force derivatives with respect to displacement and velocity are included analytically (Section 4.6), while finite-difference perturbations are applied to capture the harmonic-balance coupling terms in the global system. Iterations continue until the residual norm falls below the prescribed tolerance or divergence is detected.

4. **Post-processing:** Once convergence is achieved, the reconstructed motion is used to compute displacement and velocity statistics, spectral response, device phase behaviour, and spacing- and heading-dependent interaction measures. The same procedure is applied across all segments, sea states, spacings, and headings.

The solver accommodates both single-device and array configurations using identical iteration and convergence criteria. Hydrodynamic coupling between devices is retained through the full impedance matrix Z_{H}, while nonlinear forces are evaluated locally for each unit under the weak coupling assumption. Parallel evaluation of device level nonlinearities significantly reduces computational cost and ensures scalable array simulations.

4.8. PTO Parameter Assessment

4.8.1. Reference Parameters from Impedance Matching

For each sea state, a reference pair of PTO damping and stiffness coefficients $(B^*_{\mathrm{PTO}}, K^*_{\mathrm{PTO}})$ is obtained from the impedance matching (IM) criterion at the dominant wave frequency $\bar{\omega} = 2\pi/T_p$. The IM method provides the theoretical optimum under linear conditions by equating the radiation impedance of the device to the complex PTO impedance. The resulting tuned parameters are summarised in Table 4.2.

Table 4.2: Reference PTO parameters from IM for each sea state.

T_p [s]	H_s [m]	$\bar{\omega}$ [rad/s]	B^*_{PTO}	K^*_{PTO}
9	1.0	0.754	5.94×10^4	-6.19×10^5
9	2.0	0.754	5.94×10^4	-6.19×10^5
11	2.0	0.632	4.30×10^4	-6.52×10^5
11	3.0	0.632	4.30×10^4	-6.52×10^5

While these values define the theoretical optimum, the nonlinear harmonic balance solver does not always converge exactly at these conditions, particularly for high amplitude responses or low damping. To identify stable and near optimal performance, the PTO parameters are therefore varied systematically around the IM reference values.

4.8.2. Scaled Parameter Sweep

Each sea state employs a two-dimensional grid of scaled PTO parameters,

$$B_{\mathrm{PTO}} = B^*_{\mathrm{PTO}} s_B, \qquad K_{\mathrm{PTO}} = K^*_{\mathrm{PTO}} s_K,$$

with scaling factors

$$s_B \in [1.2, 1.6, 2.0, 2.4, 2.8, 3.2, 3.6, 4.0, 4.4, 4.8, 5.2, 5.6, 6.0], \qquad s_K \in [1.4, 1.2, 1.0, 0.8, 0.6, 0.4, 0.2].$$

This produces 13×7 parameter combinations per sea state, spanning under and over damped as well as reactive regimes. The nonlinear solver is executed for each pair $(B_{\mathrm{PTO}}, K_{\mathrm{PTO}})$, and only converged solutions are retained for performance assessment.

4.8.3. Selected PTO Parameters

Absorbed power is computed in all simulations and is required for evaluating the q factor, defined as the ratio between absorbed power in the array and that of a single isolated device. The PTO optimisation therefore uses the single–device NLFD model only. This isolates the intrinsic nonlinear response of one unit and avoids the computational cost of performing a full multi–device PTO sweep for every spacing and heading.

The highest–power regions of the single–device sweep are shown in Appendix E. The optima occur at:

$$T_p = 9.0\,\mathrm{s},\ H_s = 1.0\,\mathrm{m} : B_{\mathrm{PTO}} = 2.38 \times 10^5,\ K_{\mathrm{PTO}} = -6.19 \times 10^5,$$
$$T_p = 9.0\,\mathrm{s},\ H_s = 2.0\,\mathrm{m} : B_{\mathrm{PTO}} = 3.33 \times 10^5,\ K_{\mathrm{PTO}} = -7.43 \times 10^5,$$
$$T_p = 11.0\,\mathrm{s},\ H_s = 2.0\,\mathrm{m} : B_{\mathrm{PTO}} = 2.06 \times 10^5,\ K_{\mathrm{PTO}} = -5.22 \times 10^5,$$
$$T_p = 11.0\,\mathrm{s},\ H_s = 3.0\,\mathrm{m} : B_{\mathrm{PTO}} = 2.24 \times 10^5,\ K_{\mathrm{PTO}} = -9.13 \times 10^5.$$

These values represent the optimal tuning for a single isolated device. They do not account for array–induced changes in excitation, radiation coupling, or local phase; consequently, a single global tuning cannot be optimal for all devices, spacings, or headings simultaneously.

Using single–device tuning introduces two known implications:

- Devices inside the array may operate away from their individual optimum, because array coupling modifies their effective hydrodynamic impedance.
- Heading–dependent forcing alters local excitation amplitude and phase, meaning that one tuning cannot fit all operating conditions.

These effects are an accepted modelling decision. A full multi–device PTO optimisation would require a high–dimensional sweep at every spacing and heading and is computationally infeasible for 14–device arrays.

To improve convergence robustness in the NLFD solver while remaining close to the optimal values, slightly adjusted parameters were adopted:

$$T_p = 9.0\,\mathrm{s},\ H_s = 1.0\,\mathrm{m} : B_{\mathrm{PTO}} = 2.30 \times 10^5,\ K_{\mathrm{PTO}} = -5.90 \times 10^5,$$
$$T_p = 9.0\,\mathrm{s},\ H_s = 2.0\,\mathrm{m} : B_{\mathrm{PTO}} = 2.20 \times 10^5,\ K_{\mathrm{PTO}} = -4.00 \times 10^5,$$
$$T_p = 11.0\,\mathrm{s},\ H_s = 2.0\,\mathrm{m} : B_{\mathrm{PTO}} = 2.10 \times 10^5,\ K_{\mathrm{PTO}} = -4.20 \times 10^5,$$
$$T_p = 11.0\,\mathrm{s},\ H_s = 3.0\,\mathrm{m} : B_{\mathrm{PTO}} = 2.60 \times 10^5,\ K_{\mathrm{PTO}} = -3.40 \times 10^5.$$

These values ensured robust convergence across all nonlinear simulations without changing the qualitative behaviour of the absorbed power distributions.

4.9. Power Assessment

4.9.1. Segmentation, Convergence, and Averaging Strategy

Each irregular JONSWAP realisation is divided into twenty statistically independent 120 s segments, representing forty minutes of sea exposure. The 120 s duration provides adequate frequency resolution while maintaining manageable computational cost. Following [30], this length captures stationary nonlinear statistics without phase bias.

The harmonic count is reduced to $N = 50$ for irregular seas to preserve computational efficiency, instead of the recommended $N = 75$, while for regular wave validation cases a smaller value of $N = 6$ is adopted, as noted by [30]. The total number of harmonic components solved is therefore $2N + 1$, including the zero-frequency (DC) term. Because the computational cost of the nonlinear solver scales approximately with $N^2 \ln N$ [14], the reduced resolution is primarily employed to demonstrate the feasibility and stability of the method within reasonable runtimes. Although this simplification inevitably influences spectral accuracy and amplitude reconstruction, it allows the concept to be validated efficiently before performing higher-resolution simulations. This distinction ensures sufficient frequency resolution for broadband irregular seas while maintaining numerical efficiency for monochromatic reference tests. Sea states that fail to converge or display non-physical responses are excluded from subsequent analysis, though the raw data are retained for reference and reproducibility. The same PTO parameters ($B_{\mathrm{PTO}}, K_{\mathrm{PTO}}$) are applied consistently across all runs to isolate array-scale interactions and to attribute differences in the results solely to hydrodynamic coupling and nonlinear response characteristics.

For PTO parameter optimisation, the first ten segments of each sea state are used to estimate mean absorbed power and identify the most effective $(B_{\mathrm{PTO}}, K_{\mathrm{PTO}})$ combination. For spectral analyses and final plots, ten segments are simulated and ensemble averaged to obtain smooth, statistically representative response spectra:

$$\overline{H_X(\omega)} = \frac{1}{N_{\mathrm{seg}}} \sum_{j=1}^{N_{\mathrm{seg}}} H_X^{(j)}(\omega), \qquad N_{\mathrm{seg}} = 10.$$

This averaging procedure balances computational efficiency with statistical robustness and ensures comparability across sea states.

4.9.2. Spectral Density Analysis

The spectral response of each device was characterised from the nonlinear TD displacement signals using the real Fast Fourier Transform. For each device and DOF, the displacement time series was first mean–subtracted to remove the DC component,

$$z(t) = \zeta(t) - \overline{\zeta},$$

and the resulting signal was transformed to the FD as

$$Z(\omega) = \int_0^{T_{seg}} z(t)\, e^{-i\omega t}\, \mathrm{d}t.$$

and the one sided power spectral density computed as

$$S_{zz}(\omega) = \frac{2\,\Delta t^2}{T_{seg}} \left|Z(\omega)\right|^2, \tag{4.16}$$

where Δt is the time step and T_{seg} the segment duration. This formulation corresponds directly to the numerical implementation using `rfft` and `rfftfreq` in Python. Spectra were ensemble averaged over ten 120 s segments to ensure statistical convergence.

The resulting $S_{zz}(\omega)$ spectra are later used in Chapter 5 to examine how nonlinear forces influence resonance behaviour, bandwidth broadening, and spectral amplification across sea states and array configurations. Because phase differences between independent realisations can suppress coherent peaks, representative spectra presented in the results correspond to the first converged segment of each simulation, which accurately reflects the dynamics in steady state.

4.9.3. Array Power Interaction Factor

Collective hydrodynamic effects were quantified through the interaction factor q, which expresses how the total absorbed power of an array compares with that of isolated devices under identical conditions. It is defined as

$$q = \frac{P_{\text{array}}}{N_{\text{dev}}\, P_{\text{single}}}, \tag{4.17}$$

where P_{array} is the total absorbed power of the array, P_{single} the absorbed power of a single-device, and N_{dev} the number of devices. When $q > 1$, the interaction between radiated and diffracted waves is constructive and the array extracts more power than the equivalent set of uncoupled devices; when $q < 1$, destructive interaction occurs [60].

The total absorbed power of the array was obtained by summing the mean absorbed powers of all devices,

$$P_{\text{array}} = \sum_{i=1}^{N_{\text{dev}}} P_i, \tag{4.18}$$

where P_i denotes the mean absorbed power of device i.

The interaction factor is later used in Chapter 5 to analyse how spacing, heading, and sea state influence array-scale performance.

4.9.4. Device–Level Power Ratio

To resolve local variations within an array, each device is also compared directly against the isolated single–device reference. The device–level power ratio is defined as

$$r_i = \frac{P_i}{P_{\text{single}}}, \tag{4.19}$$

While q measures the array–averaged constructive or destructive behaviour, r_i isolates the local hydrodynamic influence on each device. Values $r_i > 1$ indicate a local constructive gain relative to the single device, whereas $r_i < 1$ indicate a local penalty.

4.9.5. Power Evaluation

The absorbed power for each simulation is computed directly from the instantaneous PTO force and velocity:

$$P_{\text{abs}} = \frac{1}{T_{\text{seg}}} \int_0^T F_{\text{PTO}}(t)\, \dot{\zeta}(t)\, dt. \tag{4.20}$$

The resulting mean power values are mapped across the $(B_{\text{PTO}}, K_{\text{PTO}})$ grid to form contour plots of absorbed power for each sea state. These maps highlight the regions of stable operation, indicate the practical tuning range where the nonlinear solver converges, and quantify how nonlinear effects modify the ideal IM configuration. Comparisons between the linear IM predictions and the nonlinear harmonic balance results reveal the shift in optimal PTO parameters caused by strong nonlinearities and coupled multi-DOF interactions.

4.10. Validation and Analytical Structure

Linear RAOs presented in Appendix H show heave amplitudes ranging between 1.75 and 0.35 m/m across the analysed frequency range, whereas the corresponding pitch and roll amplitudes remain between 0.035 and 0.015 rad/m. Even when normalised by the characteristic radius of the buoy ($D/2 = 5\,\text{m}$), the ratio of pitch to heave displacement amplitude remains below $(0.035 \times 5)/0.35 \approx 5$. This corresponds to $(5)^2 = 25\,\%$ of the heave-associated kinetic energy contribution. As the PTO operates exclusively in heave, this degree of coupling is minor for energy extraction. Restricting the nonlinear simulations to heave therefore represents a controlled approximation that retains the essential physics while avoiding unnecessary computational expansion for this validation.

4.10.1. Validation Approach

Model verification and validation are performed in two complementary steps. First, the heave-mode time series from the Python implementation are compared with a high-fidelity MATLAB reference model in the TD to confirm numerical consistency. The comparison includes displacement and velocity signals to verify the correct use of hydrodynamic coefficients and nonlinear force formulation. Minor deviations may occur due to differences between the TD and FD treatments of the radiation term and the inclusion of the preload force in the MATLAB buoyancy definition. Close agreement in amplitude, phase, and waveform establishes the correctness of the nonlinear force implementation.

Second, the linear multi-DOF response is compared directly against HAMS-MREL reference data. If the linear solution collapses to the HAMS-MREL predictions in both amplitude and phase, the hydrodynamic core of the model is considered validated. This provides a verified linear baseline from which the nonlinear extensions are subsequently introduced and analysed, as detailed in Section 5.2.

4.10.2. Time Domain Response and Power Analysis

The nonlinear simulations are evaluated directly in the TD. This approach captures instantaneous device behaviour without relying on FD linearisation and allows direct comparison between linear and nonlinear responses. For each retained DOF, the TD outputs of displacement, velocity, and excitation force are compared between the linear and nonlinear solutions.

Phase relations between excitation force and body velocity are obtained using the Hilbert transform to determine the instantaneous phase lag. This phase difference governs the efficiency of energy transfer from the wave field to the PTO. A constant phase lag is characteristic of linear harmonic response, while time-varying or asymmetric phase behaviour indicates the presence of nonlinear effects arising from restoring stiffness, viscous drag, or PTO saturation.

4.11. Computational Setup and Performance

All simulations were executed on the DelftBlue supercomputer at TU Delft [61]. Each array configuration ($5D$, $10D$, $15D$) was evaluated under four sea states and four wave headings, yielding sixteen distinct simulation cases per spacing. Each case comprised ten 120 s segments processed sequentially within the NLFD framework.

Parallelisation was implemented across headings on independent compute nodes, with one simulation per node. The computations were performed on Intel Xeon 64-core nodes with 250 GB of shared memory. Sixteen CPUs were allocated per run with 4 GB of memory per CPU. The typical wall-clock runtimes were approximately 11.2 h for the 15 D array, 10.6 h for the 10 D array, and 11.7 h for the 5 D array. These durations correspond to the complete set of ten segments per sea state and heading. The consistent runtimes across spacings confirm that computational cost scales primarily with the number of nonlinear devices rather than hydrodynamic separation distance.

All modelling and simulation code, including full documentation, is available upon request from the author or from Dr. George Lavidas.

5

Results

This chapter presents and interprets the outcomes of the numerical simulations performed with the weakly NLFD model. The structure follows the research questions introduced in Chapter 1, progressing from single–device validation to array–scale sensitivity analysis.

The chapter begins by benchmarking the heave time series against the MATLAB TD reference (Section 5.1) and validating the linear solver against HAMS-MREL predictions (Section 5.2). These comparisons establish a verified baseline for the subsequent nonlinear analyses.

The following sections examine the 14–device array, focusing on the influence of spacing (Section 5.4) and wave incidence direction (Section 5.5). These sections report the array–level trends directly. A separate detailed mechanism analysis is provided in Section 5.6, where device–level excitation, impedance modification, phase behaviour, and velocity statistics are examined in depth.

Results are presented in terms of RAO, phase plots, spectral energy distributions, absorbed power metrics, and reconstructed time series. The chapter concludes with a synthesis of the main physical trends and model limitations.

The structure of the chapter is as follows:

- Section 5.1: Verification of the MATLAB and Python NLFD implementations under regular wave conditions.
- Section 5.2: Validation of the linear solver against HAMS-MREL reference results.
- Section 5.3: Single-device absorbed power and spectral amplification analysis under irregular seas.
- Section 5.4: Array effects of inter-device spacing.
- Section 5.5: Array effects of wave incidence direction.
- Section 5.6: Local device response and synchronisation mechanisms.
- Section 5.7: Synthesis and reflection on the overall results, key mechanisms, and model limitations.

This structure maintains a direct correspondence between the modelling framework and the research questions, ensuring that each result is discussed in context and that the chapter ends with an integrated interpretation of the findings.

5.1. Model Verification Against MATLAB

The Python implementation of the NLFD solver was verified against the high-fidelity MATLAB TD reference under regular wave excitation. The comparison isolates the heave motion and velocity of a single device, the dominant DOF governing power absorption. Both solvers use identical hydrodynamic coefficients, PTO parameters, and wave definitions, ensuring a consistent physical basis for validation.

Motion and Velocity Comparison Across Sea States

Figure 5.1 shows the displacement and velocity comparison for Sea State 3, the case with the largest relative amplitude deviation. The full validation set for all four sea states is given in Appendix F. Phase alignment and waveform consistency confirm that the nonlinear restoring, viscous drag, and PTO terms are reproduced correctly within the NLFD formulation. The response amplitude scales with sea state severity as expected.

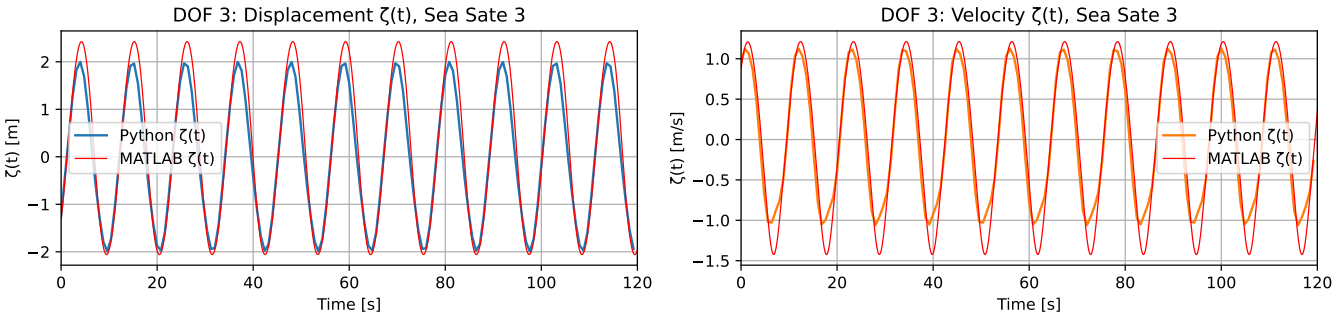

Figure 5.1: Heave displacement and velocity comparison for Sea State 3.

Quantitative Error Assessment

The amplitude discrepancies between both solvers are listed in Table 5.1. Displacement errors remain below 11%, while velocity errors stay within 17%. The small systematic under-prediction in the upper sea states results from finite harmonic truncation and the slightly stiffer restoring behaviour that occurs when the NLFD formulation linearises part of the hydrostatic term. These deviations are consistent with expected differences between FD and TD treatments of the radiation force: the NLFD solver applies an instantaneous radiation impedance, whereas the TD model includes a convolution integral for radiation memory.

Table 5.1: Amplitude comparison between the MATLAB TD and Python NLFD solvers under regular wave conditions.

Sea State	Displacement Error [%]		Velocity Error [%]	
	Value	Sign	Value	Sign
1	0.84	(+)	1.86	(+)
2	5.65	(–)	5.61	(–)
3	11.00	(–)	17.07	(–)
4	10.11	(–)	12.57	(–)

Discussion

The comparison confirms that the weakly NLFD model reproduces the temporal evolution of the heave response with high fidelity. Phase agreement across all four sea states demonstrates that both solvers resolve the same hydrodynamic impedance and PTO dynamics. The amplitude deviations at higher wave heights correspond to minor over-stiffening of the nonlinear buoyancy term at large displacements, a known consequence of harmonic truncation in weakly nonlinear formulations. Overall, the observed errors fall well within acceptable FD–TD tolerances for regular wave validation, confirming that the implementation provides a correct and robust foundation for subsequent irregular sea simulations. Such small discrepancies are physically expected due to fundamental methodological differences between FD and TD analyses. FD methods idealise wave–structure interaction as steady and harmonic, neglecting transient and strongly nonlinear components that are fully resolved in TD formulations. Consequently, perfect one-to-one matching is theoretically unattainable, and deviations ranging from a few to low double-digit percent are generally regarded as standard in contemporary hydrodynamic validation studies. For example, Read [53] reported errors of approximately 14% when nonlinear forces were included and 2% for linear cases, larger than those obtained in the present near linear sea state with $H = 1\,\mathrm{m}$ and $T = 9\,\mathrm{s}$.

5.2. Linear Validation Against HAMS-MREL

The linear behaviour of the developed solver for a single device was validated against reference RAOs computed with HAMS-MREL. This comparison ensures that, when nonlinear terms are disabled, the implementation reproduces the correct hydrodynamic response and provides a reliable baseline for the nonlinear analyses that follow.

Validation Approach

For each of the four sea states, the linear solver outputs were compared with the corresponding HAMS-MREL RAOs in heave, roll, and pitch. Amplitude and phase were evaluated on the same frequency grid as the HAMS-MREL solution, ensuring direct one-to-one comparison. If the hydrodynamic coefficients and impedance formulation are implemented correctly, the NLFD solver reduces exactly to the HAMS-MREL reference. The same B_{PTO} and K_{PTO} parameters were used for both solvers to maintain a consistent validation basis. As discussed in Subsection 4.8.3, subsequent nonlinear analyses use optimised parameters.

Results and Interpretation

The comparison confirms near-perfect agreement between the Python and HAMS-MREL results across all sea states. RAO amplitudes and phases for all DOF coincide across the full frequency range, verifying that the solver accurately reproduces the underlying radiation–diffraction physics. This demonstrates that the hydrodynamic impedance and excitation formulations are implemented correctly and that the model collapses to the established BEM solution in its linear limit.

Representative overlays for all four sea states are provided in Appendix H, showing the direct correspondence between the NLFD and HAMS-MREL results. These outcomes validate the linear formulation as a robust and verified foundation for the nonlinear extensions introduced in the next sections.

5.3. Single Device Absorbed Power Analysis and Spectral Amplification

This section addresses the third research question by characterising the response of a single device under irregular seas. The analysis establishes a physical baseline for interpreting array-scale behaviour in Sections 5.4 and 5.5.

5.3.1. Single Device RAO Amplitude and Phase Behaviour

Figure 5.2 shows the heave-mode RAO and phase for a representative operating condition of $T_p = 11\,\mathrm{s}$ and $H_s = 2\,\mathrm{m}$, which is also used throughout the array analyses.

The RAO amplitude decreases smoothly with frequency, consistent with operation below the natural resonance. The phase exhibits a progressive lag driven by hydrostatic, viscous, and PTO damping. The response is stable and free of anomalous nonlinear effects, confirming that this regime provides an appropriate reference for subsequent array studies.

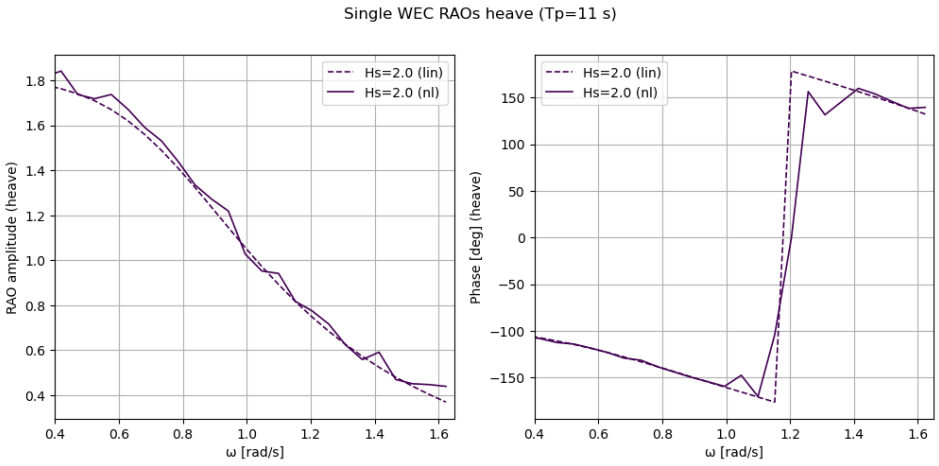

Figure 5.2: Heave-mode RAO amplitude (left) and phase (right) for a single device at $T_p = 11\,\mathrm{s}$, $H_s = 2\,\mathrm{m}$.

5.3.2. Absorbed Power under Irregular Seas

Table 5.2 summarises absorbed power across four representative sea states. Nonlinear predictions are compared directly with linear results using identical hydrodynamic and PTO parameters.

Table 5.2: Absorbed power for a single WEC under different sea states.

T_p [s]	H_s [m]	P_{lin} [W]	P_{nl} [kW]
9.0	1.0	35.58	38.67
9.0	2.0	74.65	79.44
11.0	2.0	74.78	79.79
11.0	3.0	122.11	135.57

At low sea states, linear and nonlinear predictions coincide, confirming that the weakly nonlinear formulation collapses to the linear limit when motion amplitudes are small. At $H_s = 3.0\,\mathrm{m}$, nonlinearities increase absorbed power by around 11% due to amplitude dependent restoring and viscous effects.

5.3.3. Spectral Amplification Behaviour

Figure 5.3 shows the heave displacement spectra reconstructed from the periodic nonlinear solution. The dominant response frequency remains aligned with the excitation spectrum for all sea states, while the spectral bandwidth and magnitude increase with wave height.

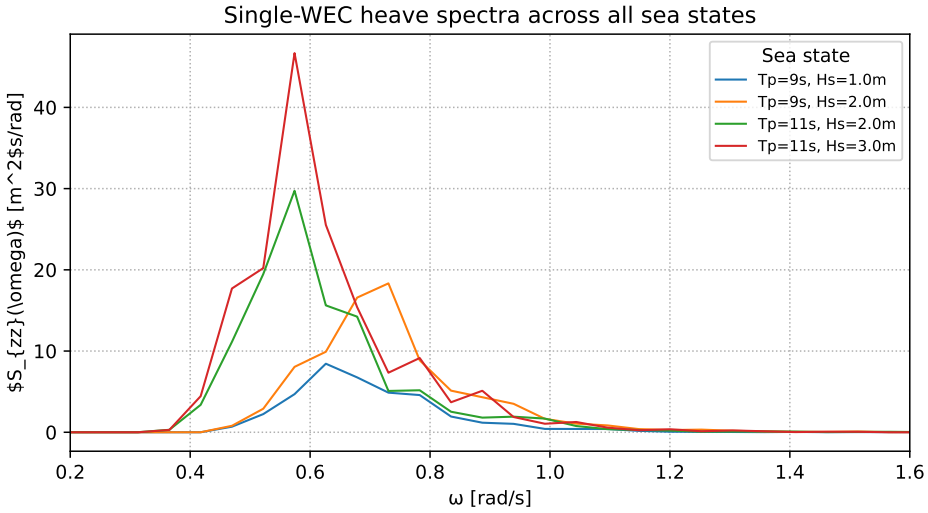

Figure 5.3: Nonlinear heave response spectra for the single WEC under four representative sea states.

Spectral energy peaks increases from approximately $8\,\mathrm{m^2s}$ at $H_s = 1.0\,\mathrm{m}$ to about $48\,\mathrm{m^2s}$ at $H_s = 3.0\,\mathrm{m}$, consistent with the quadratic dependence of the JONSWAP spectrum on wave height. The broadening of the energy peak reflects amplitude dependent damping from nonlinear restoring, viscous drag, and PTO velocity saturation. Because the JONSWAP peak period is close to the natural heave period of the device, the dominant response frequency is stiffness driven, with nonlinearities primarily broadening and attenuating the resonance peak.

Summary

The single device analysis confirms that the weakly nonlinear formulation captures the correct scaling of absorbed power, spectral bandwidth, and motion amplitude across representative sea states. This establishes a clean reference baseline for interpreting spacing and directional effects in the array-scale analyses that follow.

5.4. Sensitivity to Inter-Device Spacing

This section establishes a quantitative baseline for how the array interaction factor varies with inter-device spacing. The objective is limited: report the spacing dependence observed in the nonlinear irregular-wave simulations and demonstrate that the model reproduces the expected spatial redistribution of power across the array. All physical interpretation is deferred to Section 5.6. The three spacings are evaluated under $T_p = 11\,\mathrm{s}$, $H_s = 2.0\,\mathrm{m}$, $\beta = 90°$.

Consistent with established FD array studies [12, 24], increasing spacing weakens near-field interactions and moves the system toward independent response.

5.4.1. Interaction Factor

Figure 5.4 displays the device wise interaction factors q_i for all layouts. The pattern is consistent across all cases: rear-row devices show $q_i > 1$, front-row devices show $q_i < 1$, and the spatial transition matches the expected radiative shadowing behaviour. The array-averaged values are:

$$\bar{q}_{\mathrm{array}} = \begin{cases} 1.015 & \text{(5D)} \\ 1.043 & \text{(10D)} \\ 1.008 & \text{(15D)} \end{cases}$$

These results confirm the canonical spacing trend. At 5D the array exhibits the strongest hydrodynamic interaction, producing the widest spread of local ratios (0.95–1.10). The close spacing intensifies near–field radiation and diffraction, generating sharp constructive and destructive zones across the layout. At 10D the array shows the largest net constructive behaviour: most devices exceed their single–device reference and the interaction ratios concentrate in the 0.99–1.11 band, indicating a broad constructive region sustained by weakened but coherent far–field interference. At 15D the interaction field collapses to weak residual modulation, with individual ratios confined to 0.96–1.05, marking the onset of the independent–device approximation [17]. These results demonstrate that the nonlinear irregular–wave solver resolves these spatial structures with fidelity that is otherwise difficult to obtain outside deterministic FD analysis.

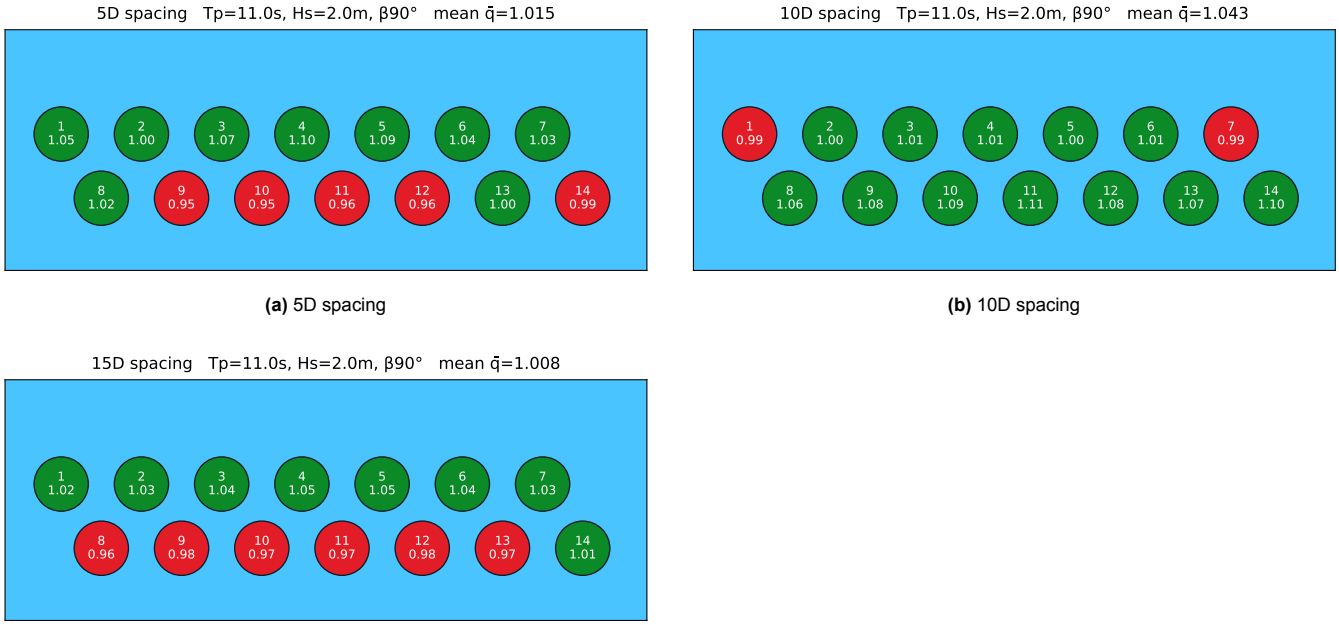

(a) 5D spacing

(b) 10D spacing

(c) 15D spacing

Figure 5.4: Factors r_i and $\bar{q}_{\text{array}}$ for three device spacings.

5.4.2. Array-Averaged Interaction Factors Across Sea States

Figure 5.5 summarises the array-averaged interaction factors $\bar{q}_{\text{array}}$ across all spacings and sea states at $\beta = 90°$. Across all four sea states the interaction factors remain mildly constructive, with $0.98 \lesssim \bar{q}_{\text{array}} \lesssim 1.18$ for all spacings. For the mildest sea state $(T_p, H_s) = (9\,\text{s}, 1.0\,\text{m})$, the 10D layout shows the strongest constructive behaviour, with 5D and 15D giving smaller but still positive amplification. At $(9\,\text{s}, 2.0\,\text{m})$ all spacings collapse close to $\bar{q}_{\text{array}} \approx 1$, while for $(11\,\text{s}, 2.0\,\text{m})$ the 10D case again gives the largest deviation above unity and 5D and 15D follow closely. At $(11\,\text{s}, 3.0\,\text{m})$ the 15D spacing remains essentially unchanged from the previous sea state, with $\bar{q}_{\text{array}} \approx 1.02$. The 5D layout stays slightly constructive (≈1.03), and the 10D layout decreases from its earlier peak but still remains above unity at ≈1.10.

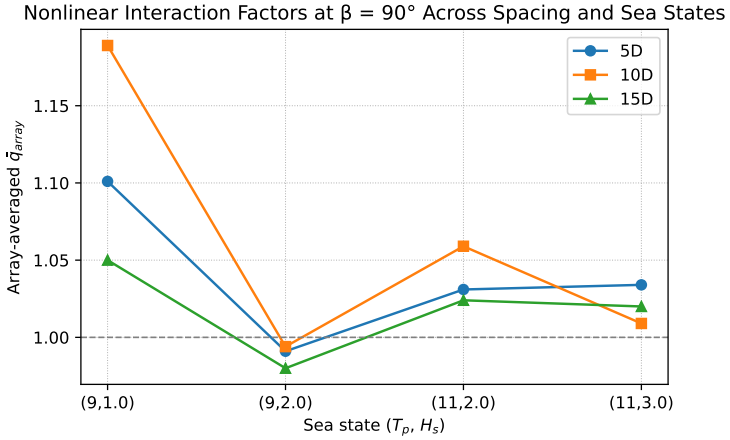

Figure 5.5: Variation of $\bar{q}_{\text{array}}$ with sea state for three spacings.

These trends reproduce the established transition from collective to independent behaviour with increasing separation [12, 17, 19, 24].

5.5. Directional Response

This section extends the analysis to multiple incident wave headings to quantify how directionality influences hydrodynamic coupling and absorbed power. The 10D spacing configuration is used together with the representative irregular sea state $T_p = 11\,\mathrm{s}$, $H_s = 2.0\,\mathrm{m}$, ensuring that all variation arises solely from changes in wave direction.

5.5.1. Interaction Factor and Absorbed Power

Figure 5.6 shows the spatial distribution of individual interaction factors q_i for headings from $0°$ to $90°$. The array-averaged values are:

$$\bar{q}_{\text{array}} = \begin{cases} 1.032 & \text{for } \beta = 0° \\ 0.933 & \text{for } \beta = 30° \\ 1.040 & \text{for } \beta = 60° \\ 1.043 & \text{for } \beta = 90° \end{cases}$$

At $0°$, the devices directly facing the incoming waves show clear amplification (up to $q_i \approx 1.82$), while the rear row exhibits attenuation down to $q_i \approx 0.81$. This produces a mildly constructive net response.

At $30°$, attenuation dominates across the array, with only a few downstream devices near unity, yielding the lowest interaction level of all headings.

At $60°$, most devices show constructive interaction ($q_i \approx 1.02$–1.19), producing the strongest directional amplification in the heading sweep.

At $90°$, the response becomes nearly symmetric, with all devices slightly above unity and a mean value very close to that at $60°$. This behaviour aligns with the expected broadside symmetry in long arrays [35, 36].

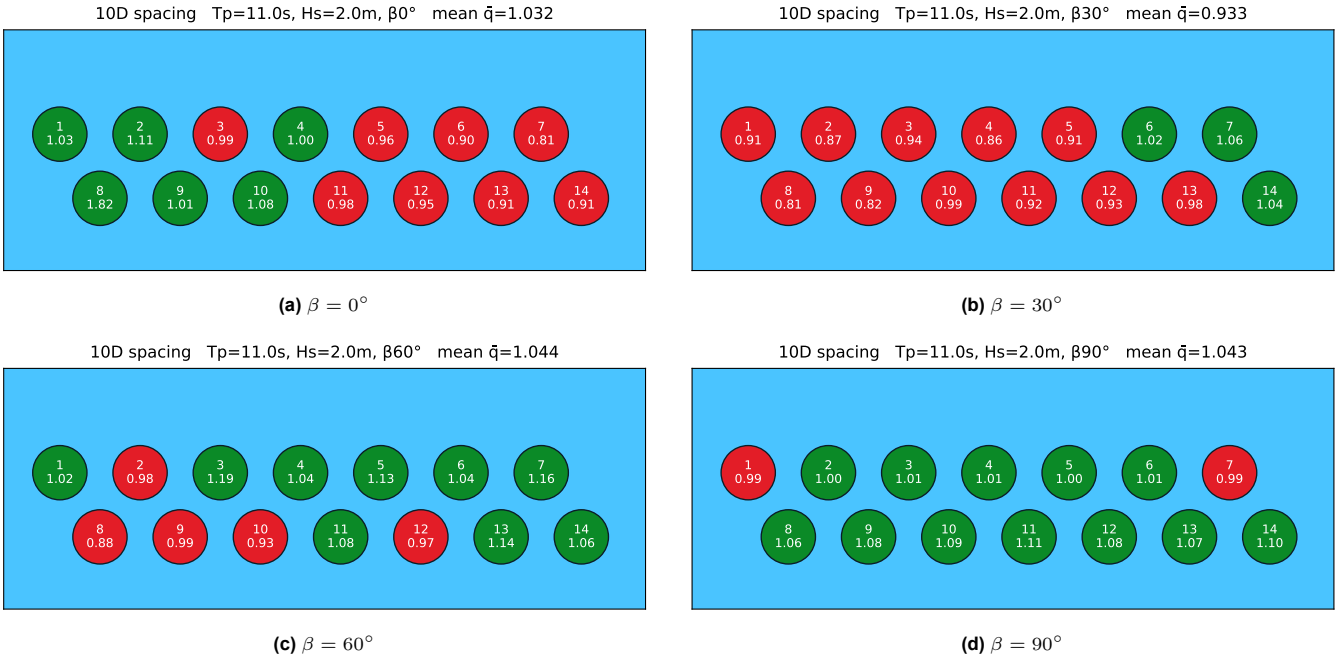

(a) $\beta = 0°$ **(b)** $\beta = 30°$

(c) $\beta = 60°$ **(d)** $\beta = 90°$

Figure 5.6: Factors r_i and $\bar{q}_{\text{array}}$ for the 10D array under varying wave headings.

The directional trends shown here are consistent with earlier FD studies on multi-body arrays [13, 22, 34].

5.5.2. Array-Averaged Behaviour Across Sea States

Figure 5.7 summarises the array-averaged interaction factors $\bar{q}_{\text{array}}$ across all sea states, spacings, and headings. Across all spacings, the $30°$ heading consistently produces the lowest interaction levels, while $60°$ and $90°$ yield the highest. Directional alignment therefore dominates the response, with sea-state intensity acting only as a secondary modifier.

For the compact 5D arrangement, the heading dependence is the most pronounced. At $0°$, the interaction factor rises strongly with sea-state energy, increasing from $\bar{q}_{\text{array}} = 0.75$ in $(T_p, H_s) = (9\,\text{s}, 1.0\,\text{m})$ to $\bar{q}_{\text{array}} = 1.29$ in $(11\,\text{s}, 3.0\,\text{m})$. This increase is driven almost entirely by two devices: WEC 1 and WEC 8 reach $q_i = 3.19$ and $q_i = 2.87$, respectively, in the highest sea state.

At $30°$, all sea states remain below unity ($\bar{q}_{\text{array}} = 0.78$–$0.96$). The $60°$ and $90°$ headings remain close to unity, varying only within $\bar{q}_{\text{array}} = 0.94$–$1.13$ and $\bar{q}_{\text{array}} = 0.98$–$1.19$, respectively.

At larger spacings (10D and 15D), the directional contrast decreases steadily. The $60°$ heading retains the highest values, the $30°$ heading remains the lowest, and the $0°$ and $90°$ cases stay near unity across all sea states. By 15D spacing, the four headings differ by less than a few percent, indicating that directional sensitivity collapses once radiative coupling is sufficiently weakened.

These results align with previous observations that directional alignment, rather than sea state amplitude, becomes the dominant control parameter once devices are sufficiently separated [24, 35, 36].

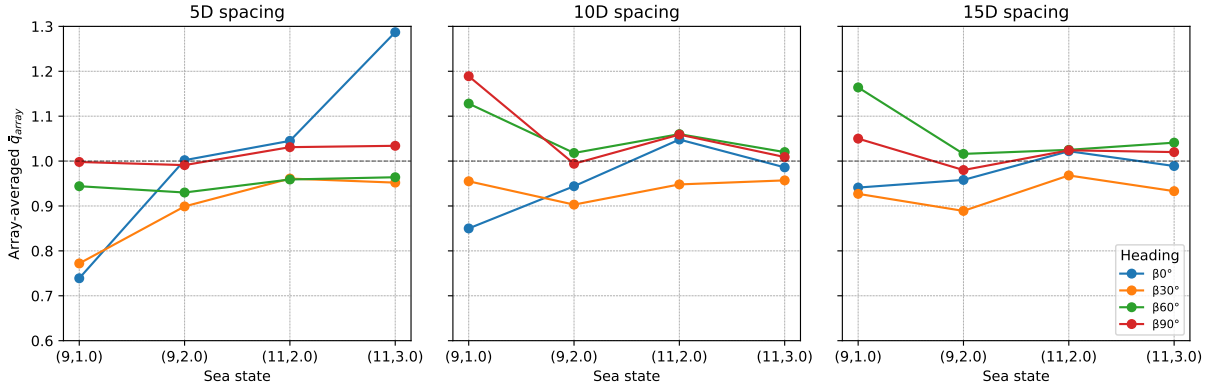

Figure 5.7: Array-averaged interaction factor $\bar{q}_{\text{array}}$ across four sea states, three spacings, and four headings. Dashed line: neutral condition $\bar{q}_{\text{array}} = 1$.

5.6. Case Study: Local Response Mechanisms at 15D Spacing

This section examines the residual interaction mechanisms at large spacing by analysing three representative devices in the 15D configuration under irregular excitation with

$$T_p = 11\,\text{s}, \qquad H_s = 2.0\,\text{m}, \qquad \beta = 90°.$$

The isolated single–device solution provides the reference absorbed power. Local array effects are quantified using the device–level power ratio defined in Section 4.9.4. For the 15D layout, the upstream devices WEC 1 and WEC 2 yield ratios of $r_1 = 1.02$ and $r_2 = 1.03$, indicating a weak constructive deviation from the single–device baseline. WEC 8, located at an off–centre position within the front row, gives $r_8 = 0.96$, showing a mild reduction in absorbed power.

The analysis below explains the origin of these small but systematic deviations using excitation levels, spectral energy content, RAO amplitudes, nonlinear phase statistics, and velocity distributions. The objective is to identify why WEC 1 and WEC 2 experience slight local benefit at 15D spacing, whereas WEC 8 experiences a modest penalty relative to the single–device response.

5.6.1. Excitation Force and Heave Spectral Energy

The link between excitation and spectral response follows the spectral formulation in Section 4.9.2. Because the JONSWAP spectrum is narrow-banded, the dominant contribution to device motion arises from a confined frequency region around the peak.

Figure 5.8 includes a grey curve showing the normalised JONSWAP spectrum together with a shaded band. The shaded band marks the frequency interval in which the spectrum remains above 10% of its peak value. This threshold isolates the part of the spectrum that contributes materially to the device motion while excluding the long low-energy tails. For a narrow JONSWAP peak, values above 10% still supply significant excitation, whereas values below this level decay rapidly and contribute negligibly. The exact choice is not critical; the 10% cut-off consistently separates the energetic region across all cases. All spectral averages in Table 5.3 are taken over this energetic band.

Table 5.3 lists the band-averaged excitation magnitude and the corresponding heave spectral density. The excitation values come directly from the linear hydrodynamics and differ by less than 1% between WEC 1, WEC 2, WEC 8, and the isolated device, showing that the array is effectively at the isolated-device limit hydrodynamically. The incoming wave field therefore does not account for the observed performance differences.

The heave spectral densities show small but systematic differences. WEC 1 and WEC 2 exhibit slightly elevated spectral energy across the energetic band relative to the isolated device, as indicated by their band integrals, which are 2–3% above the single-device value. WEC 8 has a band integral of similar magnitude but shows a distinct feature not present in the other cases: it exhibits the highest peak of the heave displacement spectrum, while the peaks of WEC 1, WEC 2 and the isolated device are nearly coincident. Here, the term “resonance” denotes the frequency at which the heave displacement spectrum $S_{zz}(\omega)$ attains its maximum under the present hydrodynamic and PTO settings. Thus, WEC 8 concentrates its small spectral excess sharply at the resonance frequency, whereas WEC 1 and WEC 2 distribute their modest excess more broadly across the energetic band. Because the energetic band is narrow, even these small changes in peak height or distribution across the band are sufficient to alter the realised motion energy.

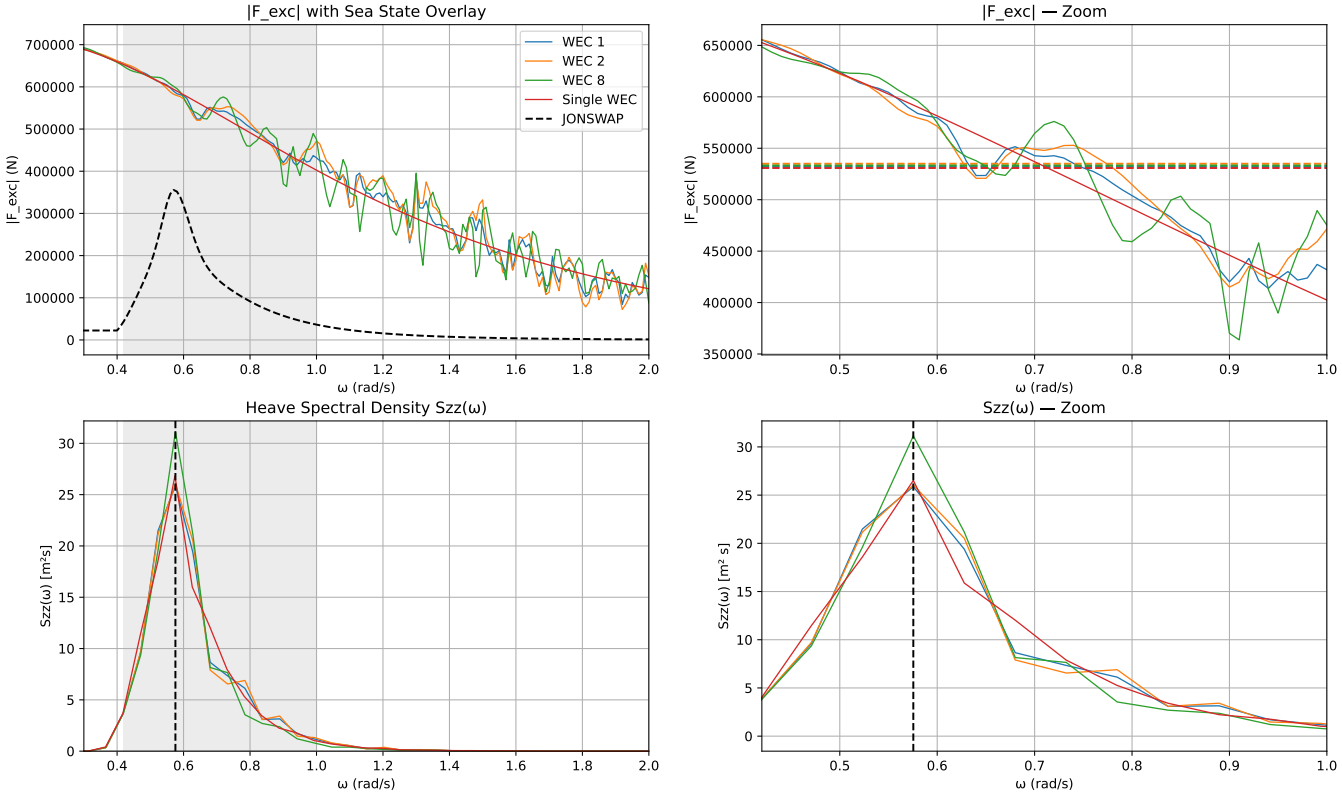

Figure 5.8: Excitation force magnitude and heave spectral density for WEC 1, WEC 2, and WEC 8 at 15D spacing.

Table 5.3: Excitation and heave spectral-response metrics within the energetic JONSWAP band at 15D spacing.

WEC	$\overline{\lvert F_{\mathrm{exc}}\rvert}$ [N]	$\overline{S_{zz}}$ [m^{2}s]	$\int S_{zz}\, d\omega$ [m^2]
1	532 360	9.780×10^{0}	5.346
2	534 962	9.824×10^{0}	5.365
8	533 213	9.788×10^{0}	5.367
Single	530 813	9.682×10^{0}	5.236

In short:

- Excitation forcing is effectively identical across all devices.
- The narrow energetic band makes small RAO-driven perturbations visible in S_{zz}.
- WEC 1 and WEC 2 show slightly elevated broad-band spectral energy, while WEC 8 exhibits the highest resonant peak; these distinct spectral patterns underpin the power differences examined later.

5.6.2. Segment-Averaged Phase, Phase Lag, and RAO Magnitude

The device motions follow directly from the coupled FD equations introduced in Section 3.2. For each device, the heave response examined here is the heave component of the full six–DOF solution $\mathbf{X}(\omega)$, with its RAO defined in Eq. (3.7). Figure 5.9 shows the segment-averaged absolute phase, true phase lag, and RAO magnitude for WEC 1, WEC 2, WEC 8, and the isolated device over the full sea-state frequency range.

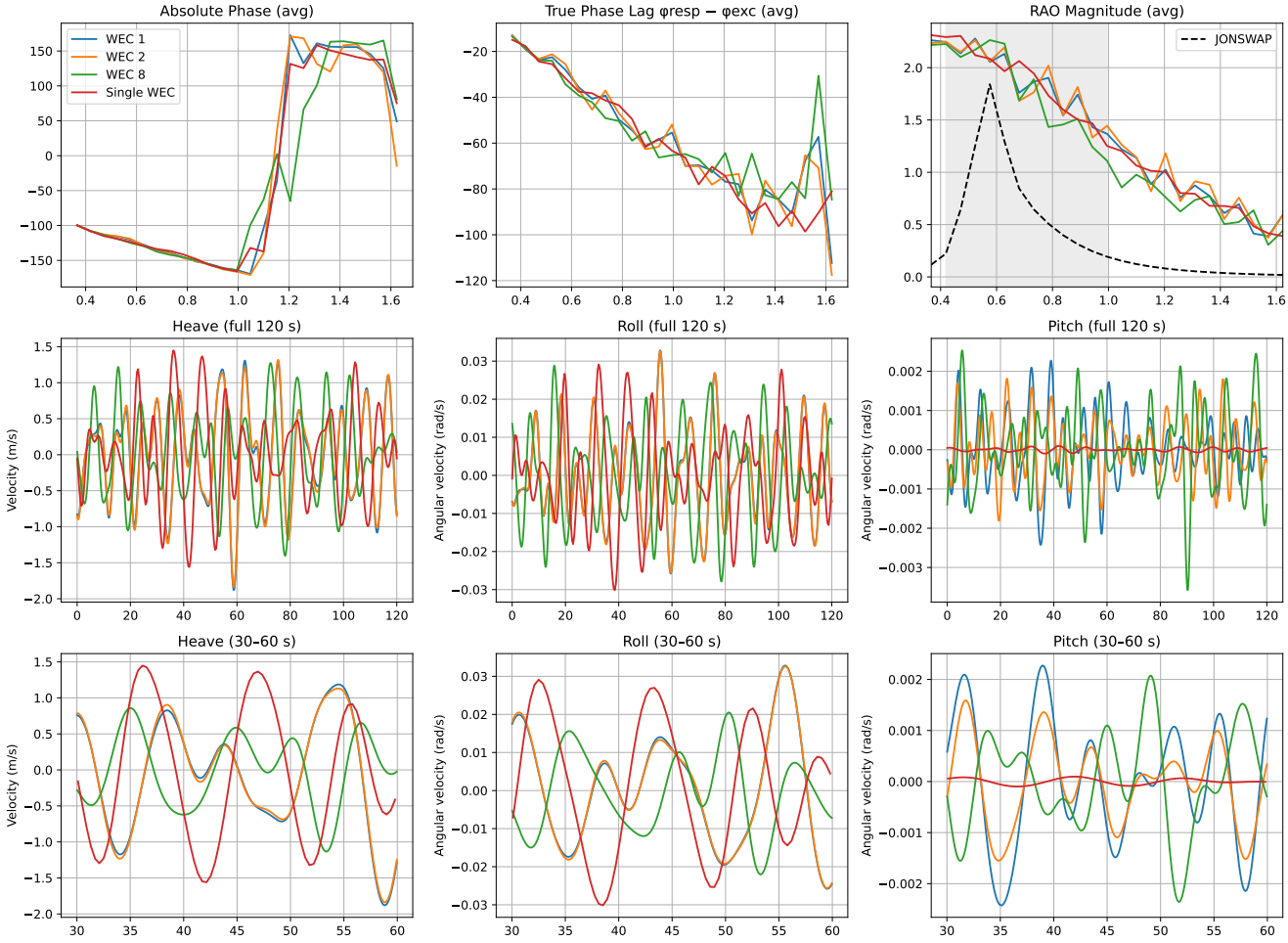

Figure 5.9: Segment-averaged absolute phase, phase lag, and RAO magnitude for WEC 1, WEC 2, WEC 8, and the isolated device at 15D spacing.

Three observations follow directly from the FD results:

1. **Absolute phase.** All devices exhibit the same absolute-phase evolution, including the characteristic phase jump at higher frequencies. A small offset is visible for WEC 8, but this does not represent a physical phase difference. Absolute phase depends on the arbitrary time origin of each nonlinear segment, and segment averaging retains small numerical offsets. Only phase lag removes this bias.
2. **Phase lag.** The true phase lag $\phi_{\mathrm{resp}} - \phi_{\mathrm{exc}}$ decreases monotonically with frequency for all devices, as expected for a radiation- and PTO-damped heaving body. Crucially, the four curves remain tightly grouped across the entire frequency range, including the effective resonant frequency $\omega_{\mathrm{res}} \approx 0.5755\,\mathrm{rad/s}$. At this frequency the devices exhibit nearly identical phase lag (about $-40°$ to $-50°$), demonstrating that hydrodynamic interaction at 15D spacing is too weak to alter the dynamic phase relationship. Phase lag therefore does not contribute to the small differences in absorbed power between devices.

3. **RAO magnitude.** Over the full frequency range, the RAO magnitudes of WEC 1 and WEC 2 are slightly larger than those of WEC 8 and the isolated device across much of the energetic band indicated in grey. In particular, WEC 8 shows a modest reduction in RAO magnitude on the upper side of the band, where the incident JONSWAP spectrum still carries significant energy.

The time-series velocity plots in the lower panels of Figure 5.9 reflect this behaviour: all devices show broadly similar heave-, roll-, and pitch-motion envelopes over the full 120-second realisations. WEC 8 displays slightly lower heave-velocity amplitudes than WEC 1 and WEC 2, consistent with its modestly different RAO shape, but the differences remain small.

Overall, the phase and RAO diagnostics confirm that at 15D spacing the array operates very close to the isolated-device limit. WEC 1 and WEC 2 reproduce the isolated response across the entire sea-state frequency range, while WEC 8 differs only through a narrowly concentrated increase in its resonant RAO peak. These minimal FD deviations underpin the small variations in spectral energy and absorbed power reported earlier, explaining why WEC 1 and WEC 2 experience slight constructive interaction whereas WEC 8 does not.

5.6.3. Nonlinear Phase Coherence and Velocity RMS

Nonlinear phase behaviour is summarised in Table 5.4, which reports the mean phase lag, phase fluctuations, coherence, and velocity root mean square (RMS) for all devices.

Table 5.4: Nonlinear phase statistics across all segments at 15D spacing.

WEC	Mean phase lag (°)	RMS fluct. (°)	Weighted RMS (°)	Coherence	Vel. RMS (m/s)
1	-58.15	32.15	28.52	0.821	0.6266
2	-58.98	33.13	29.42	0.816	0.6300
8	-56.02	29.50	26.65	0.836	0.6097
Single	-60.55	30.39	30.43	0.831	0.6210

The mean phase lag, RMS fluctuation, and coherence values differ only slightly between devices, and none of these quantities follow the ordering of absorbed power. WEC 8 has the highest coherence and the smallest phase fluctuation, but it also has the lowest velocity RMS. Conversely, WEC 1 and WEC 2 do not exhibit distinctly higher coherence or lower phase variability, yet they achieve the largest velocity RMS.

The velocity RMS values reproduce exactly the power ordering discussed earlier:

$$\text{WEC 2} > \text{WEC 1} > \text{Single} > \text{WEC 8}.$$

Because the PTO force used here is proportional to the velocity, the absorbed power reduces directly to a constant multiple of the velocity variance through Eq. (4.20). Velocity RMS is therefore the only nonlinear metric in Table 5.4 that aligns consistently with the observed power ratios, while the phase-based quantities do not influence performance at this spacing.

5.6.4. Why Devices Differ in Absorbed Power

The causal structure for the 15D configuration is:

1. The incident linear excitation $|F_{\mathrm{exc}}(\omega)|$ is almost identical for all devices. Within the energetic JONSWAP band, the band-averaged excitation differs by less than 1% between WEC 1, WEC 2, WEC 8, and the single device. The small power differences therefore cannot be attributed to variations in incoming wave forcing.
2. The absolute and true phase-lag curves of all devices collapse across the full frequency range, including the resonant frequency $\omega_{\mathrm{res}} \approx 0.5755\,\mathrm{rad/s}$. Hydrodynamic interaction at 15D spacing is too weak to produce any meaningful phase shift relative to the isolated device, so phase does not differentiate the device responses.
3. The remaining distinction is the heave RAO magnitude. Across the energetic band, WEC 1 and WEC 2 exhibit slightly larger RAO magnitudes than the single device, while WEC 8 shows a modest reduction. Because the spectrum is narrow, these small differences in RAO magnitude directly lead to the band-averaged spectral-energy shifts observed in $S_{zz}(\omega)$.
4. The heave spectral density and its band integrals follow the same pattern: WEC 1 and WEC 2 accumulate slightly more spectral energy than the single device, whereas WEC 8 remains marginally below. This carries over to the velocity statistics, where the velocity RMS satisfies

$$\dot{\zeta}_{\mathrm{rms},2} > \dot{\zeta}_{\mathrm{rms},1} > \dot{\zeta}_{\mathrm{rms,single}} > \dot{\zeta}_{\mathrm{rms},8}.$$

5. Through Eq. (4.20), and using a PTO force that is proportional to the velocity, absorbed power reduces to a constant multiple of the velocity variance. The ordering of velocity RMS therefore maps directly onto the ordering of absorbed power.
6. Expressed as power ratios relative to the single device,

$$r_2 > r_1 > 1 > r_8,$$

so WEC 1 and WEC 2 experience a slight constructive effect, while WEC 8 is marginally penalised.

At 15D spacing the array is therefore close to the isolated-device limit: excitation and phase are indistinguishable from the single device, and only weak array-induced changes in effective dynamic compliance remain. These small RAO-based adjustments to the velocity variance are sufficient to explain why WEC 1 and WEC 2 gain a few percent in absorbed power, while WEC 8 loses a few percent.

5.7. Reflection

The results presented in this chapter demonstrate that the weakly NLFD formulation provides a coherent, validated, and physically interpretable description of multi–device dynamics under irregular wave excitation. The model reproduces the nonlinear TD benchmark with good quantitative accuracy and collapses exactly to the linear BEM reference when nonlinear terms are disabled, confirming the correctness of both the hydrodynamic implementation and the numerical solution strategy. The subsequent array analyses build on this foundation and reveal how spacing, wave direction, and device synchronisation jointly determine array-scale behaviour. Before discussing the broader implications, the primary findings are summarised below.

Key Findings

- The weakly NLFD solver reproduces the nonlinear TD benchmark within 17 % amplitude deviation and matches HAMS-MREL RAOs exactly in the linear limit, confirming correct radiation–diffraction physics and numerical formulation.
- Increasing wave height primarily raises the peak spectral energy (scaling approximately with H_s^2), while introducing only mild broadening from amplitude-dependent restoring and damping. Changes in T_p have a much stronger effect on the spectral width, shifting the response to lower frequencies and widening the energetic band.
- Inter-device spacing controls the transition from constructive interaction (5D–10D) to near-independent response (15D), with $\bar{q}_{\mathrm{array}}$ approaching unity at large separation.
- Directional incidence governs array performance primarily through radiative phase alignment. Across all spacings, the 30° heading produces the lowest interaction factors, while 60°–90° yield the highest.
- Local 5D analysis shows that device-level differences arise from array-induced impedance modification rather than from differences in the incoming excitation. Rear-row amplification and front-row suppression originate from variations in RAO magnitude, phase behaviour, and velocity statistics.

Overall behavioural trends

Three dominant mechanisms were consistently observed across all results. First, nonlinear restoring and velocity-dependent effects broaden the spectral response without altering the dominant frequency, confirming the validity of the weakly nonlinear assumption in the examined sea states. Second, inter-device spacing determines the strength of hydrodynamic coupling: compact arrays exhibit mild constructive interaction, while wider separations lead to near-independent operation. Third, incident wave direction modulates array behaviour through radiative synchronisation, with long-side incidence providing the most coherent reinforcement.

These trends are consistent with established theoretical and experimental studies [12, 13, 24], and the present model reproduces these dependencies under irregular seas in a fully coupled, multi–device setting.

Physical interpretation

The combined RAO, phase, and spectral analyses show that array performance is governed primarily by phase coherence rather than excitation magnitude. Constructive interaction occurs when radiated and incident fields remain synchronised across rows, whereas destructive interaction arises once radiative phase differences become large enough to reduce dynamic compliance.

The 15D case study in Section 5.6 shows that all devices experience effectively identical excitation and phase behaviour, placing the array close to the isolated device limit. The small differences in absorbed power arise instead

from weak, device specific variations in RAO magnitude across the narrow energetic band. These modest shifts in dynamic compliance produce the observed ordering in spectral energy and velocity variance, explaining why WEC 1 and WEC 2 gain slightly in absorbed power while WEC 8 experiences a minor reduction.

Model limitations and numerical performance

Several assumptions and numerical characteristics influence the quantitative accuracy of the predictions. The weakly nonlinear formulation does not include radiation memory effects, directional spreading, or viscous cross-coupling, restricting its validity to steady periodic regimes. At high sea states, the Newton-Raphson iteration occasionally fails to converge when initiated from a linear seed, particularly when the nonlinear system admits multiple nearby equilibria. This explains the isolated cases of harmonic-bin misallocation observed at 0° incidence in the highest sea state. Such sensitivity is well documented in harmonic balance applications [29, 30] and reflects the practical limit of the weakly nonlinear assumption rather than a flaw in the implementation. This mechanism can occasionally assign the steady solution to an incorrect harmonic bin, producing exaggerated device level amplification in isolated cases. This accounts for the outlier values reported in Section 5.5.2.

Convergence is also sensitive to the initial phase. In multi-device arrays, the Newton-Raphson iteration converges more reliably when the linear seed is naturally aligned with the true nonlinear solution (typically near broadside). At oblique headings, the seed introduces a systematic phase mismatch, increasing iteration count and, in several cases, preventing convergence. This behaviour is consistent with earlier observations that harmonic balance solvers require phase-consistent initialisation in coupled configurations.

A further limitation stems from the use of PTO parameters tuned for a single isolated device. Because the PTO parameters were tuned on a single device, they are not optimal for each specific device in the array configuration. The effective impedance experienced by each device changes within the array due to radiative softening and stiffening, meaning that the optimal PTO settings differ from those of the isolated case. As a result, certain (spacing, heading) combinations exhibit stiffer or softer effective dynamics than anticipated by the single-device tuning, which affects both convergence behaviour and the attainable steady-state response.

A further limitation is the use of global incident excitation, which neglects small device-specific diffraction-induced phase shifts, and the harmonic truncation, which suppresses very high frequency components. The convergence characteristics therefore vary systematically with sea state, heading, and spacing. Convergence remained robust for all moderate sea states, while a subset of the highest-severity cases exhibited reduced convergence rates or failure to converge from the linear seed. A complete overview of iteration counts and convergence outcomes for all (spacing, heading, sea state) combinations is provided in Appendix G for transparency.

A final limitation concerns the sampling of the non-dimensional spacing kd. The four representative sea states correspond to only two distinct peak periods ($T_p = 9$ and 11 s), and therefore to only two values of kd for each spacing. As a result, the present analysis does not span the wider kd-range over which classical linear interference theory predicts oscillatory constructive and destructive interaction. Falnes' two-body formulation [62] shows that spacing-dependent amplification is strongly non-monotonic when expressed as a function of kd, but such behaviour cannot appear here because the selected sea states do not sample the interference extrema. The spacing-related conclusions in this chapter are therefore valid only within the limited kd-interval represented by the chosen sea states and cannot be generalised across the full period distribution in the long-term wave climate.

Despite these limitations, the solver produced physically consistent and repeatable results across the full set of converged simulations and remained numerically stable within the intended weakly nonlinear regime.

Implications for array design and modelling

The findings emphasise that array efficiency depends more on directional phase synchronisation than on spacing alone. Compact configurations permit mild amplification under aligned directional conditions, but the benefit collapses rapidly as incidence deviates from the long-side orientation. Beyond approximately ten diameters spacing, radiative coupling becomes sufficiently weak that the array behaves almost as a collection of independent absorbers. Across all headings and spacings, the array-averaged interaction factor remains within a few percent of unity, indicating strong directional robustness for this class of device. From a design perspective, adaptive PTO tuning that preserves phase alignment offers significantly larger performance gains than small adjustments of array geometry.

Summary

In summary, the solver reproduces linear behaviour, extends reliably into the weakly nonlinear regime, and captures the principal array-scale mechanisms: radiative interaction, shadowing, directional sensitivity, and dynamic compliance modification. The analyses show that phase coherence is the primary driver of array performance, with spacing and heading acting as secondary modifiers. These findings form the basis for the conclusions in Chapter 6, where the research questions are addressed and directions for further work are outlined.

6

Conclusion

This thesis developed and validated a weakly NLFD model for large arrays of point absorber WECs. The objective was to determine how such a formulation can predict and interpret spectral response and absorbed power under realistic irregular seas while remaining computationally efficient. Verification, linear validation, and systematic array studies were conducted across four representative sea states and multiple layouts to assess both physical accuracy and practical modelling value.

Main research question

> *How can a weakly nonlinear frequency domain model characterise the dynamic behaviour and power performance of large WEC arrays under realistic sea conditions?*

The results demonstrate that the weakly NLFD formulation provides a transparent and efficient framework for array-scale analysis. It bridges the gap between linear hydrodynamics and nonlinear TD simulation by reproducing key nonlinear trends at a fraction of the computational cost while maintaining direct access to RAO structure, spectral energy distributions, and phase-synchronisation mechanisms. Such quantities are essential for interpreting array behaviour in irregular seas, where spectral alignment governs performance.

Sub-questions

1. To what extent does the model reproduce established time domain results? Comparison with the nonlinear MATLAB TD reference showed amplitude errors of 11–17%, and consistent phase across all sea states. Waveform shape and nonlinear distortion patterns matched closely, confirming that the formulation captures nonlinear restoring, viscous drag, and PTO behaviour within the weakly nonlinear regime. This provides a validated basis for extending the method to irregular seas.

2. How accurately does the solver reproduce linear hydrodynamic behaviour predicted by HAMS-MREL? With nonlinear terms disabled, the solver collapses exactly to the HAMS-MREL BEM solution. Heave, roll, and pitch RAOs match across the full frequency range, verifying the correctness of the hydrodynamic impedance and excitation formulation. The nonlinear results therefore rest on a fully verified linear foundation.

3. How do nonlinear effects influence spectral amplification and absorbed power for a single device? Increasing wave height broadens the spectral response and increases velocity variance, producing modest power gains relative to the linear prediction. Spectral peaks rise from approximately $8\,\mathrm{m^2s}$ to $48\,\mathrm{m^2s}$ across the tested sea states while remaining centred near the dominant excitation frequency. Nonlinearities therefore modify bandwidth rather than resonance location, and the solver captures the expected physical saturation under energetic seas.

4. How does inter-device spacing modify array-scale hydrodynamic interactions and power absorption? Spacing primarily redistributes absorbed power between devices while leaving the array-averaged response close to that of an isolated unit. At 5D, rear-row devices experience constructive amplification while front-row devices show mild attenuation. At 10D the interactions weaken, and by 15D the system approaches independent behaviour with only small deviations in $\bar{q}_{\mathrm{array}}$. These trends agree with established frequency-domain interaction studies and confirm that spacing mainly affects the spatial pattern of amplification and attenuation.

5. How does wave incidence direction modify array-scale hydrodynamic interactions and power absorption? Heading differences are more influential than spacing. For the representative 10D layout at $T_p = 11\,\mathrm{s}$, $H_s = 2.0\,\mathrm{m}$, the array-averaged interaction factor varies only modestly around unity ($\bar{q}_{\mathrm{array}} = 0.933$ at $30°$, $\bar{q}_{\mathrm{array}} = 1.044$ at $60°$). Direction primarily redistributes power between devices rather than altering the total absorbed by the array. Across all spacings and sea states, the widest $\bar{q}_{\mathrm{array}}$ range (0.75–1.29) occurs in the compact 5D configuration under the highest sea state, where nonlinearities and convergence sensitivity are strongest. Overall, directional phase alignment, and not spacing alone, governs array efficiency under irregular seas.

Synthesis and implications

The results show that the weakly NLFD formulation provides a fast and physically interpretable framework for analysing large WEC arrays in irregular seas. Its FD structure separates excitation, impedance, and nonlinear forces, making the governing mechanisms directly identifiable.

The accuracy of the predictions is bounded mainly by two structural assumptions: (i) the omission of transient viscous memory and (ii) reconstruction of the incident wave field without full diffraction-induced spatial variability. Device-specific excitation from HAMS-MREL is included and phase is corrected, but higher-order local distortion is not represented. The modest amplification observed in compact layouts should be interpreted within these limits.

Convergence difficulties occurred primarily under oblique incidence, where strong nonlinearity and a phase-misaligned linear seed led to occasional Newton-Raphson stagnation. This behaviour is consistent with known limitations of harmonic balance in multi-equilibria regimes and indicates that improved seeding or trust-region methods would enhance robustness.

Within these constraints, the solver resolves the dominant physical mechanisms: radiative phase alignment controls array behaviour; spacing modifies effective compliance through softening and stiffening; and nonlinear damping limits excessive amplification while stabilising the periodic response. The formulation therefore extends linear interaction theory into the weakly nonlinear regime with controlled and well-understood accuracy.

For design use, the findings indicate that phase coherence governs array performance more strongly than geometric compactness. Adaptive PTO tuning aimed at preserving phase alignment is likely to yield greater benefit than incremental spacing changes. A spacing threshold of $S/D \geq 5$ suppresses most hydrodynamic interaction, leaving directional exposure and control strategy as the dominant design variables. The computational efficiency of the solver makes it well suited for early-stage configuration screening without reliance on high-cost TD campaigns.

Contributions

This thesis delivers methodological, scientific, and practical advances for modelling large WEC arrays in irregular seas.

1. Methodological development
   - Developed a fully verified weakly NLFD framework for multi-body arrays, incorporating nonlinear PTO, restoring, and drag forces while retaining the computational efficiency of the FD formulation.
   - Generalised existing single–device formulations to many hydrodynamically coupled bodies with full radiation and diffraction interaction across all DOF.
   - Implemented a modular architecture in which hydrodynamics, nonlinear force models, PTO settings, and array geometries are interchangeable, enabling application to arbitrary layouts and device counts.

2. Verification and physical validation
   - Demonstrated excellent agreement with nonlinear TD and linear BEM benchmarks: the solver reproduces phase–accurate nonlinear dynamics and collapses exactly to the HAMS-MREL solution in the linear limit, validating both the impedance formulation and the numerical implementation.

3. Advancing the understanding of array physics in irregular seas
   - Quantified nonlinear spectral effects across sea states and established scaling relations linking sea–state intensity, radiative phase behaviour, and motion energy.
   - Showed that array efficiency is governed primarily by directional phase synchronisation rather than spacing alone, extending linear interaction theory to weakly nonlinear irregular wave conditions.
   - Produced the first irregular wave characterisation of a 14–device array within a weakly NLFD framework, revealing radiative softening, stiffening, and heading–dependent compliance effects not captured by linear models.

4. Practical modelling and design contributions
   - Delivered a computational framework that evaluates periodic nonlinear response one to two orders of magnitude faster than TD simulation, while providing both FD outputs and reconstructed time series.
   - Provided a reproducible high-performance computing workflow for large multi-parameter sweeps in spacing, heading, and sea state, supporting both research and early-stage industrial layout optimisation.
   - Integrated long–term metocean data from a North Atlantic hindcast, demonstrating scalability toward site-specific forecasting and farm design.

Recommendations for future work

The present formulation establishes a verified and consistent baseline, but several extensions would broaden its physical scope, numerical robustness, and applicability. These can be grouped into enhanced physics, improved solver reliability, control integration, and extended validation.

1. Enhanced physical modelling
   - Extend the solver to incorporate coupled surge and sway modes, short–crested wave fields, and directional spreading, allowing assessment of whether heave dominance and phase coherence persist under more realistic multi-directional forcing.
   - Introduce stochastic phase realisations and directional spectra to quantify ensemble variability and establish confidence bounds on absorbed power and interaction factors.

2. Improved numerical robustness
   - Develop trust-region or continuation-based Newton methods (e.g. dogleg strategies, quasi-Newton updates) to increase reliability in regimes with multiple nonlinear equilibria.
   - Explore improved seeding strategies through continuation in sea-state severity or frequency stepping to reduce sensitivity to initial conditions, especially at oblique headings or high energy levels.

3. Integration of control and measurement
   - Explore array–level PTO tuning rather than relying on single–device tuning, since radiative softening and stiffening modify each device's effective impedance.
   - Incorporate model predictive control with upstream wave measurement (as implemented on the CPO C5), enabling phase-consistent initialisation and reducing the need for multiple independent nonlinear segments.

4. Extended validation and application
   - Couple the hydrodynamic solver with structural–response or techno-economic modules to link array hydrodynamics directly to design decisions.
   - Extend validation to multi-device configurations using recent physical array experiments such as those reported in [63], addressing the remaining experimental gap in array scale validation.

These developments would transition the solver from a validated research tool to a robust operational framework capable of supporting array design, phase-control strategies, and site-specific performance assessment.

Critical reflection and societal relevance

The developed weakly NLFD framework is reliable within the regime for which its assumptions hold: moderate nonlinearities, negligible viscous memory, and incident-wave fields without strong local diffraction effects. By stating these limits explicitly, the work ensures responsible use of the model and avoids over-interpretation of the modest amplification observed in compact arrays. The implementation is open and reproducible, contributing to the wider movement in marine energy toward transparent, physics-based modelling tools.

The solver provides practical value for early-stage array development. Its efficiency enables rapid screening of layouts and PTO settings, reducing reliance on computationally intensive TD campaigns and allowing engineers to explore a broader design space at minimal cost. The ability to resolve hydrodynamic interaction in irregular seas delivers insight during conceptual design, when decisions on spacing, array orientation, and directional exposure are most consequential.

More broadly, improving confidence in multi-device prediction supports the maturing of wave energy as a component of future renewable portfolios. Accurate, accessible tools are essential as the sector transitions from single prototypes to coordinated arrays and farms. By clarifying the strengths and limits of the approach, this work provides both technical capability and critical judgement, ensuring that its results can be used responsibly in design, research, and policy contexts.

Closing remarks

This thesis shows that weakly NLFD methods can capture the governing physics of large WEC arrays with clarity, speed, and controlled accuracy. Array performance is shaped primarily by radiative phase alignment rather than geometric compactness, and even in irregular seas the key mechanisms remain interpretable through excitation, impedance, and spectral structure.

The solver is modular, reproducible, and immediately usable for multi–device hydrodynamic studies. It can be applied directly to layout screening, PTO investigations, and site-specific feasibility assessments without modification to the numerical formulation.

While full nonlinearity, directional spreading, and integrated control remain important avenues for future work, this study demonstrates that mechanism-based prediction at the array scale is achievable at a fraction of the computational cost of conventional approaches. As wave energy moves toward coordinated arrays and commercial deployment, transparent and efficient modelling tools such as this will be essential for linking conceptual design to practical offshore implementation.

References

[1] Ottmar Edenhofer, Ramón Pichs-Madruga, Youba Sokona, Kristin Seyboth, Patrick Eickemeier, Patrick Matschoss, Gerrit Hansen, Susanne Kadner, Steffen Schlömer, Timm Zwickel, and Christoph von Stechow, eds. *Renewable energy sources and climate change mitigation: Special report of the Intergovernmental Panel on Climate Change*. Cambridge, UK and New York, NY, USA: Cambridge University Press, 2012. ISBN: 9781107607101.

[2] ETIP Ocean. *A Study into the Potential Social Value Offered to Europe from the Development and Deployment of Wave and Tidal Energy to 2050*. European Technology and Innovation Platform for Ocean Energy (ETIP Ocean). 2023. URL: https://www.etipocean.eu/wp-content/uploads/2023/09/ETIP-Ocean-Social-Value-Report-2023.pdf.

[3] Annette Kristin Brask. *Control and Estimation of Wave Energy Converters*. Master's thesis, NTNU Trondheim. 2015. URL: https://ntnuopen.ntnu.no/ntnu-xmlui/bitstream/handle/11250/2350944/13829_FULLTEXT.pdf.

[4] Coastal Wiki. *Wave energy converters*. Retrieved from the Coastal Wiki. 2024. URL: https://www.coastalwiki.org/wiki/Wave_energy_converters.

[5] Guixun Zhu, Zahra Shahroozi, Siming Zheng, Malin Göteman, Jens Engström, and Deborah Greaves. "Experimental Study on Point Absorber WECs in Extreme Waves". In: *Ocean Engineering* 280 (2023), p. 115815. DOI: 10.1016/j.oceaneng.2023.115815.

[6] Bingyong Guo, Tianyao Wang, Siya Jin, Shunli Duan, Kunde Yang, and Yaming Zhao. "A Review of Point Absorber Wave Energy Converters". In: *Journal of Marine Science and Engineering* 10.10 (2022), p. 1534. DOI: 10.3390/jmse10101534.

[7] I. C. Scurtu, B. I. Mîndroiu, R. Bosneagu, and I. Hristache. "A Review of Wave Energy Conversion with Point Absorber". In: *Technium EcoGeoMarine* 2 (2023), pp. 45–60. DOI: 10.47577/eco.v2i.12490.

[8] The University of Western Australia, Carnegie Clean Energy, and Australian Renewable Energy Agency. *From single to multiple wave energy converters: Cost reduction resource assessment report (ARENA 2015 RND086)*. Tech. rep. Australian Renewable Energy Agency, 2021. URL: https://arena.gov.au/assets/2021/10/wave-energy-cost-reduction-resource-assessment-report.pdf.

[9] Jørgen Hals Todalshaug, Gunnar Steinn Ásgeirsson, Eysteinn Hjálmarsson, Jéromine Maillet, Patrik Möller, Pedro Pires, Matthieu Guérinel, and Miguel Lopes. "Tank testing of an inherently phase-controlled wave energy converter". In: *International Journal of Marine Energy* 15 (2016). Selected Papers from the European Wave and Tidal Energy Conference 2015, Nante, France, pp. 68–84. ISSN: 2214-1669. DOI: https://doi.org/10.1016/j.ijome.2016.04.007.

[10] Liguo Wang, Jan Isberg, and Elisabetta Tedeschi. "Review of control strategies for wave energy conversion systems and their validation: the wave-to-wire approach". In: *Renewable and Sustainable Energy Reviews* 81 (2018), pp. 366–379. DOI: 10.1016/j.rser.2017.06.074.

[11] D. V. Evans. "Some Analytic Results for Two and Three Dimensional Wave-Energy Absorbers". In: *Power from Sea Waves*. Academic Press, 1980, pp. 213–249.

[12] Aurélien Babarit. "On the park effect in arrays of oscillating wave energy converters". In: *Renewable Energy* 58 (2013), pp. 68–78. DOI: 10.1016/j.renene.2013.03.008.

[13] B.F.M. Child and V. Venugopal. "Optimal configurations of wave energy device arrays". In: *Ocean Engineering* 37.16 (2010), pp. 1402–1417. ISSN: 0029-8018. DOI: https://doi.org/10.1016/j.oceaneng.2010.06.010.

[14] Alexis Mérigaud and John V. Ringwood. "A Nonlinear Frequency-Domain Approach for Numerical Simulation of Wave Energy Converters". In: *IEEE Transactions on Sustainable Energy* 9.1 (2018), pp. 86–94. DOI: 10.1109/TSTE.2017.2716826.

[15] G Failla, PD Spanos, and M Di Paola. "Response power spectrum of multi-degree-of-freedom nonlinear systems by a Galerkin technique". In: *Journal of applied mechanics* 70.5 (2003), pp. 708–714.

[16] V. Raghavan, E. Loukogeorgaki, N. Mantadakis, A. V. Metrikine, and G. Lavidas. "HAMS-MREL, a new open source multiple body solver for marine renewable energies: Model description, application and validation". In: *Ocean Engineering* 297 (2024), p. 115621. DOI: 10.1016/j.renene.2024.121577.

[17] Xuefeng Shao, Jonas W. Ringsberg, Huidong Yao, and Umesh R.S.L. Gowda. “Hydrodynamic interactions and enhanced energy harnessing amongst many WEC units in large-size wave parks”. In: *Journal of Marine Science and Engineering* 12.5 (2024), p. 730. DOI: 10.3390/jmse12050730.

[18] Bo Yang, Shaocong Wu, Hao Zhang, Bingqiang Liu, Hongchun Shu, Jieshan Shan, Yaxing Ren, and Wei Yao. “Wave energy converter array layout optimization: A critical and comprehensive overview”. In: *Renewable and Sustainable Energy Reviews* 184 (2022), p. 113356. ISSN: 1364-0321. DOI: https://doi.org/10.1016/j.rser.2022.112668.

[19] Qian Zhong and Ronald W. Yeung. “Wave-body interactions among energy absorbers in a wave farm”. In: *Applied Energy* 233–234 (2019), pp. 1051–1064. DOI: 10.1016/j.apenergy.2018.09.131.

[20] Sarah M. Cotey. “Hydrodynamic Analysis of Arrays of General Bodies”. Master’s thesis. Cambridge, MA: Massachusetts Institute of Technology, 2024. URL: https://hdl.handle.net/1721.1/154603.

[21] Xiaohui Zeng, Qi Wang, Yuanshun Kang, and Fajun Yu. “Hydrodynamic interactions among wave energy converter array and a hierarchical genetic algorithm for layout optimization”. In: *Renewable Energy* (2022). DOI: 10.1016/j.oceaneng.2022.111521.

[22] Philip Balitsky, Gael Verao Fernandez, Vasiliki Stratigaki, and Peter Troch. “Assessment of the power output of a two-array clustered WEC farm using a BEM solver coupling and a wave-propagation model”. In: *Energy Procedia* (2018). DOI: 10.3390/en11112907.

[23] Xinyuan Shao, Hua-Dong Yao, Jonas W. Ringsberg, Zhiyuan Li, and Erland Johnson. “Performance analysis of two generations of heaving point absorber WECs in farms of hexagon-shaped array layouts”. In: *Ships and Offshore Structures* 19.6 (2024), pp. 687–698. DOI: 10.1080/17445302.2024.2317658.

[24] Vaibhav Raghavan, Matias Alday, Andrei Metrikine, and George Lavidas. “Wave Energy Farm Assessment in Real Wave Climates: The North Sea”. In: *Proceedings of the ASME 2024 43rd International Conference on Ocean, Offshore and Arctic Engineering (OMAE 2024)*. 2024. DOI: 10.1115/OMAE2024-120946.

[25] Jian Tan, Henk Polinder, Antonio Jarquin Laguna, and Sape Miedema. “The application of the spectral domain modeling to the power take-off sizing of heaving wave energy converters”. In: *Renewable Energy* 195 (2022), pp. 528–540. DOI: 10.1016/j.apor.2022.103110.

[26] Mauro Bonfanti and Sergej Antonello Sirigu. “Spectral-domain modelling of a non-linear wave energy converter: Analytical derivation and computational experiments”. In: *Mechanical Systems and Signal Processing* 198 (2023), p. 110398. DOI: 10.1016/j.ymssp.2023.110398.

[27] Salman Husain, Gordon G. Parker, David Forehand, and Enrico Anderlini. “Radiation Force Modeling for a Wave Energy Converter Array”. In: *Energies* 17.1 (2024). ISSN: 1996-1073. DOI: 10.3390/en17010006.

[28] Gianmarco Giorgi, Alessandro Faedo, and John V. Ringwood. “A compact 6-DOF nonlinear model for wave energy converters using Froude–Krylov and hydrostatic forces”. In: *IEEE Transactions on Sustainable Energy* 9.3 (2018), pp. 1173–1181. DOI: 10.1109/TSTE.2018.2826578.

[29] Alexis Mérigaud and John V Ringwood. “Incorporating ocean wave spectrum information in short-term free-surface elevation forecasting”. In: *IEEE Journal of Oceanic Engineering* 44.2 (2018), pp. 401–414.

[30] Riccardo Novo, Giovanni Bracco, Sergej A Sirigu, Giuliana Mattiazzo, Alexis Mérigaud, and John V Ringwood. “Non linear simulation of a wave energy converter with multiple degrees of freedom using a harmonic balance method”. In: *International Conference on Offshore Mechanics and Arctic Engineering*. Vol. 51319. American Society of Mechanical Engineers. 2018, V010T09A041.

[31] Chris Guiver. “A method for constrained energy-maximising control of heaving wave-energy converters via a nonlinear frequency response”. In: *2024 IEEE Conference on Control Technology and Applications (CCTA)*. IEEE. 2024, pp. 590–597.

[32] Y. Wei, A. Bechlenberg, M. van Rooij, B. Jayawardhana, and A.I. Vakis. “Modelling of a wave energy converter array with a nonlinear power take-off system in the frequency domain”. In: *Applied Ocean Research* 90 (2019), p. 101824. ISSN: 0141-1187. DOI: https://doi.org/10.1016/j.apor.2019.05.009.

[33] Huaqing Jin, Haicheng Zhang, and Daolin Xu. “Array buoys with nonlinear stiffness enhance low-frequency wave attenuation and energy capture”. In: *Physics of Fluids* 34.12 (2022).

[34] Xuanlie Zhao, Qingping Zou, Jing Geng, Yang Zhang, and Zhijie Wang. “Influences of wave resonance on hydrodynamic efficiency and loading of an OWC array under oblique waves”. In: *Applied Ocean Research* 124 (2022), p. 103069. DOI: 10.1016/j.apor.2022.103069.

[35] Justin McGuinness and Gareth Thomas. “Optimisation of wave-power arrays without prescribed geometry over incident wave angle”. In: *Irish Maritime Energy Journal* 4 (2021), pp. 1–10. DOI: 10.36688/imej.4.1-10.

[36] Zhi Yung Tay and Vengatesan Venugopal. “The impact of energy extraction of wave energy converter arrays on wave climate under multi-directional seas”. In: *Journal of Ocean Engineering and Marine Energy* 5 (2019), pp. 51–72. DOI: 10.1007/s40722-019-00127-w.

[37] Shangyan Zou, Bryson Robertson, Aeron Roach, Tim Mundon, Brian Rosenberg, and Markel Penalba. “Wave energy converter arrays: A methodology to assess performance considering the disturbed wave field”. In: *Renewable Energy* 215 (2024), p. 120719. DOI: 10.1016/j.renene.2024.120719.

[38] M. Penalba, T. Kelly, and J. V. Ringwood. “Using NEMOH for modelling wave energy converters: A comparative study with WAMIT”. In: *Proceedings of the 12th European Wave and Tidal Energy Conference (EWTEC)*. Cork, Ireland, 2017.

[39] S. Kass. “Exploring the Limits of Boundary Element Methods for Wave Energy Converter Hydrodynamics”. Master’s thesis. Seattle, WA: University of Washington, 2024.

[40] V. Raghavan, G. Lavidas, A. V. Metrikine, N. Mantadakis, and E. Loukogeorgaki. “A comparative study on BEM solvers for Wave Energy Converters”. In: *Trends in Renewable Energies Offshore – Guedes Soares (Ed)*. London: CRC Press, 2023. ISBN: 978-1-003-36077-3.

[41] O. M. Faltinsen. *Sea Loads on Ships and Offshore Structures*. Cambridge University Press, 1990.

[42] C. C. Mei, M. Stiassnie, and D. K. P. Yue. *Theory and Applications of Ocean Surface Waves*. World Scientific, 2005.

[43] M. Penalba, J. V. Ringwood, and G. Giorgi. “High-fidelity modelling of wave energy systems: A review of frequency-domain models for control applications”. In: *Renewable and Sustainable Energy Reviews* 93 (2018), pp. 38–52. DOI: 10.1016/j.rser.2018.05.027.

[44] Leo H. Holthuijsen. “5.3.4 The Velocity Potential Function”. In: *Waves in Oceanic and Coastal Waters*. Cambridge University Press, 2007. ISBN: 978-0-521-86028-4. URL: https://app.knovel.com/hotlink/khtml/id:kt007N2OOB/waves-in-oceanic-coastal/velocity-potential-function.

[45] G. Giorgi and J. V. Ringwood. “Nonlinear hydrodynamic modeling of wave energy converters using meshfree methods”. In: *Ocean Engineering* 163 (2018), pp. 251–264. DOI: 10.1016/j.oceaneng.2018.06.048.

[46] Jian Tan and Antonio Jarquin Laguna. “Spectral-Domain Modelling of Wave Energy Converters as an Efficient Tool for Adjustment of PTO Model Parameters”. In: *Proceedings of the European Wave and Tidal Energy Conference*. Vol. 15. 2022. DOI: 10.36688/ewtec-2023-278.

[47] M. Bonfanti and S. Sirigu. “Nonlinear frequency-domain modeling of wave energy converters”. In: *Renewable Energy* 201 (2023), pp. 1234–1247. DOI: 10.1016/j.renene.2022.12.019.

[48] N. Faedo et al. “Nonlinear modeling and control of wave energy converters: A review”. In: *Renewable and Sustainable Energy Reviews* 135 (2021), p. 110209. DOI: 10.1016/j.rser.2020.110209.

[49] K. Hasselmann et al. “Measurements of wind-wave growth and swell decay during the Joint North Sea Wave Project (JONSWAP)”. In: *Ergänzungsheft zur Deutschen Hydrographischen Zeitschrift, Reihe A(8)* 12 (1973).

[50] M. Alves. “Frequency-Domain Models”. In: *Numerical Modelling of Wave Energy Converters*. Ed. by J.V. Ringwood. Elsevier, 2016, pp. 49–84.

[51] Yanji Wei, Alva Bechlenberg, Bayu Jayawardhana, and Antonis I Vakis. “Modelling of a wave energy converter array with non-linear power take-off using a mixed time-domain/frequency-domain method”. In: *IET Renewable Power Generation* 15.14 (2021), pp. 3220–3231.

[52] Bret Bosma, Zhe Zhang, Ted K.A. Brekken, H. Tuba Özkan-Haller, Cameron McNatt, and Solomon C. Yim. “Wave energy converter modeling in the frequency domain: A design guide”. In: *2012 IEEE Energy Conversion Congress and Exposition (ECCE)*. 2012, pp. 2099–2106. DOI: 10.1109/ECCE.2012.6342553.

[53] Robert Read and Harry Bingham. “Time- and Frequency-domain Comparisons of the Wavepiston Wave Energy Converter”. In: *Proceedings of the 33rd International Workshop on Water Waves and Floating Bodies (IWWWFB 2018)*. Guidel-Plages, France, 2018. URL: http://www.iwwwfb.org/Workshops/33.htm.

[54] Bret Bosma, Ted K. A. Brekken, H. Tuba Özkan-Haller, and Solomon C. Yim. “Wave energy converter modeling in the time domain: A design guide”. In: *2013 1st IEEE Conference on Technologies for Sustainability (SusTech)*. 2013, pp. 103–108. DOI: 10.1109/SusTech.2013.6617305.

[55] Rico H. Hansen, Morten M. Kramer, and Enrique Vidal. “Discrete Displacement Hydraulic Power Take-Off System for the Wavestar Wave Energy Converter”. In: *Energies* 6.8 (2013), pp. 4001–4044. ISSN: 1996-1073. DOI: 10.3390/en6084001.

[56] Matías Alday and George Lavidas. “The ECHOWAVE Hindcast: A 30-years high resolution database for wave energy applications in North Atlantic European waters”. In: *Renewable Energy* 236 (2024), p. 121391. ISSN: 0960-1481. DOI: 10.1016/j.renene.2024.121391.

[57] Tethys. *CorPower Ocean HiWave-5 Project*. Tethys: Marine Energy Knowledge Hub. Accessed: [24/06/2025]. 2025. URL: https://tethys.pnnl.gov/project-sites/corpower-ocean-hiwave-5-project.

[58] Matías Alday, Vaibhav Raghavan, and George Lavidas. “Effects of wave spectrum representation on power production estimations from point absorbers”. In: *Applied Ocean Research* 161 (2025), p. 104626. ISSN: 0141-1187. DOI: https://doi.org/10.1016/j.apor.2025.104626.

[59] Gabriel Forstner, Tobias Glaser, Pierre Lourdais, and Jørgen Hals Todalshaug. “A control-oriented modeling framework for wave energy converters”. In: *Proceedings of the European Wave and Tidal Energy Conference*. Vol. 16. 2025.

[60] A.D. de Andrés, R. Guanche, L. Meneses, C. Vidal, and I.J. Losada. “Factors that influence array layout on wave energy farms”. In: *Ocean Engineering* 82 (2014), pp. 32–41. ISSN: 0029-8018. DOI: https://doi.org/10.1016/j.oceaneng.2014.02.027. URL: https://www.sciencedirect.com/science/article/pii/S0029801814000651.

[61] Delft High Performance Computing Centre (DHPC). *DelftBlue Supercomputer (Phase 2)*. https://www.tudelft.nl/dhpc/ark:/44463/DelftBluePhase2. 2024.

[62] Johannes Falnes. “Radiation impedance matrix and optimum power absorption for interacting oscillators in surface waves”. In: *Applied ocean research* 2.2 (1980), pp. 75–80.

[63] Timothy Vervaet, Peter Troch, Vasiliki Stratigaki, Brecht De Backer, Kurt Stockman, and Marc Vantorre. “Experimental modelling of point-absorber wave energy converter arrays: A comprehensive review, identification of research gaps and design of the WECfarm setup”. In: *Applied Ocean Research* 120 (2022), p. 103137. DOI: 10.3390/jmse10081062.

A

BEM Solver Comparison

Feature	WAMIT	NEMOH	Capytaine	HAMS-MREL	AQWA
Type	Commercial	Open-source	Open-source	Open-source	Commercial
Frequency Domain	Yes	Yes	Yes	Yes	Yes
Parallelisation	No	No	No	Yes (OpenMP support)	Yes
Multiple Bodies	Limited	Yes	Partial (hydrodynamics only)	Yes	Yes
Irregular Frequencies	Yes (removal techniques)	No (susceptible to errors)	Yes	Yes (efficient removal)	Yes
Computational Efficiency	Moderate	Moderate (high computational cost)	High (simple geometries)	High (especially for deep water)	Moderate
Complex Geometries	High	Moderate	Moderate	High	High
Accuracy	High	Moderate	High	High	High
Best For	Complex geometries, large arrays	Simple to moderate geometries	Simple geometries, Python workflows	Multi-body systems, deep-water cases	Large-scale, multi-body systems

Table A.1: Comparison of common BEM solvers for WEC array modelling.

B

Scatter Diagram

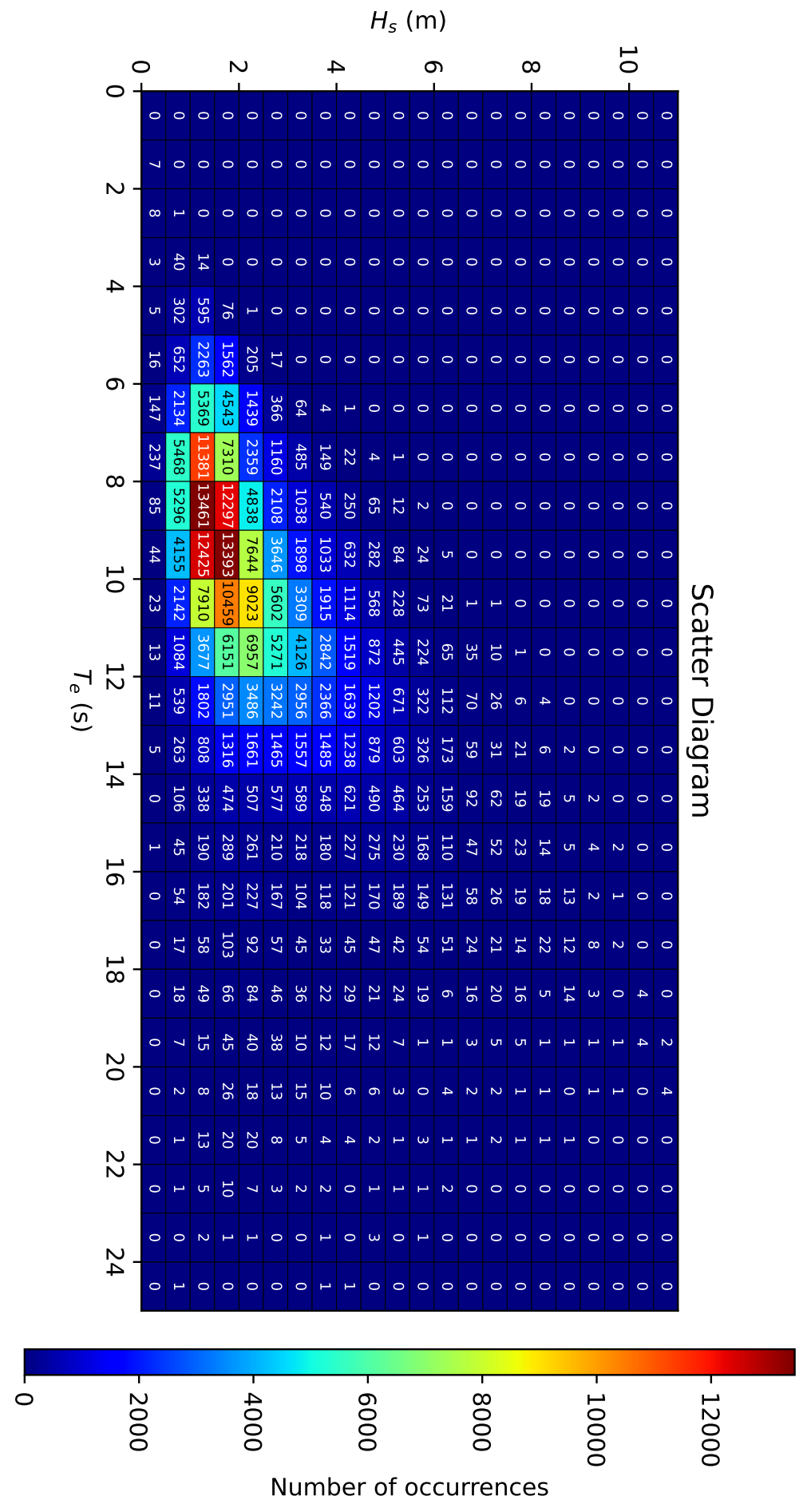

Figure B.1: Scatter diagram for the period 1992–2021.

C

Mesh Files

To illustrate the discretisations used in the convergence study of Section 4.4, the five panel meshes tested in HAMS-MREL are shown below. Each image corresponds to one of the five resolutions (537, 747, 1222, 2342, 4185 panels).

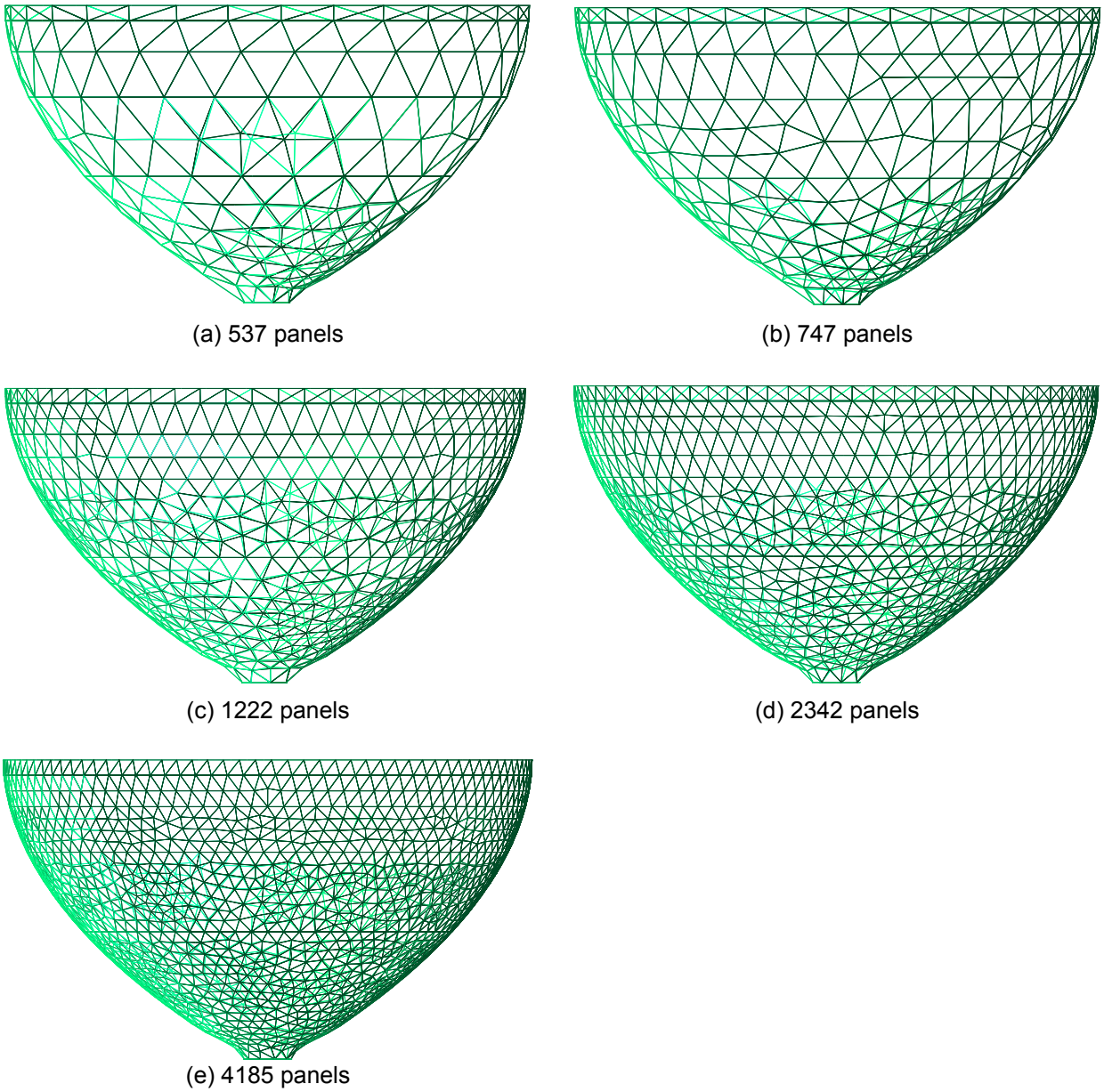

(a) 537 panels

(b) 747 panels

(c) 1222 panels

(d) 2342 panels

(e) 4185 panels

Figure C.1: Meshes used in the hydrodynamic convergence study.

D

Convergence Study

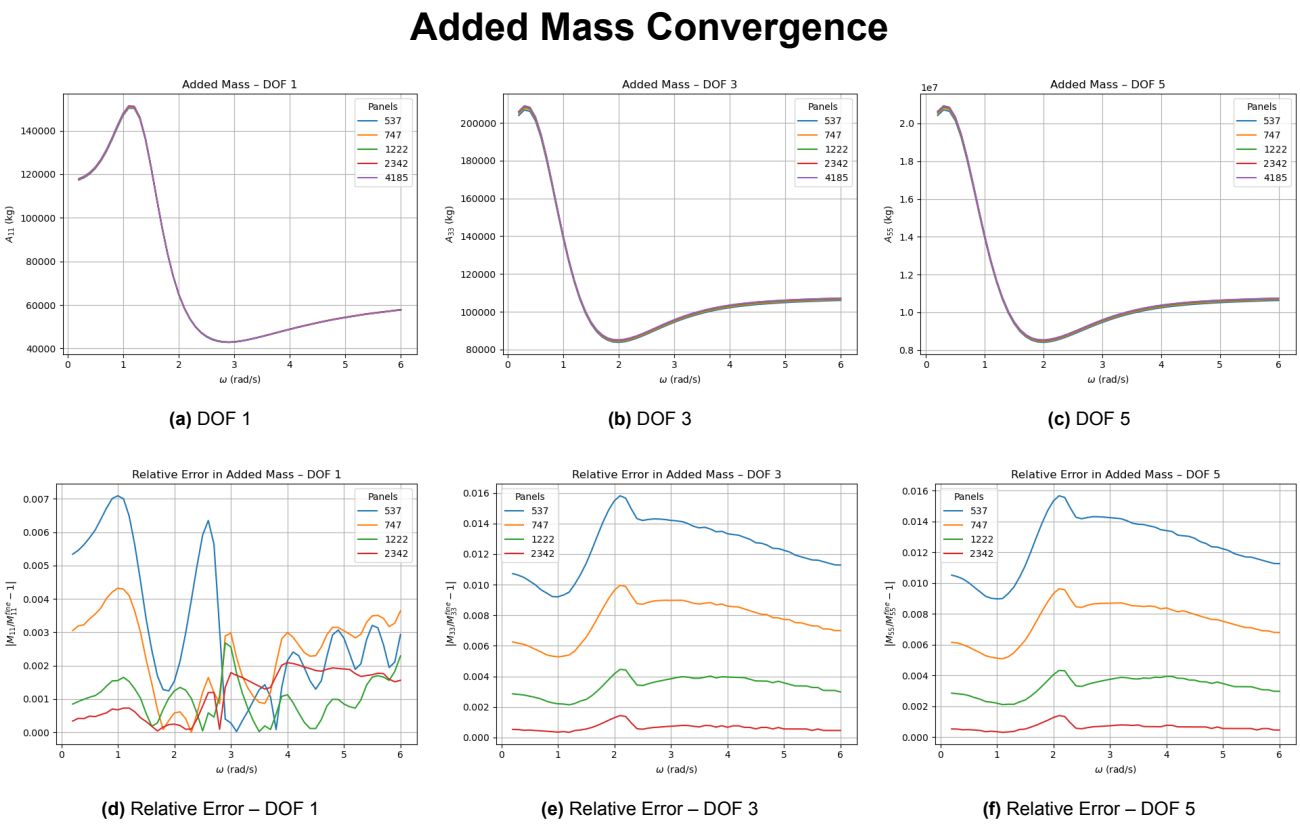

(a) DOF 1 **(b)** DOF 3 **(c)** DOF 5

(d) Relative Error – DOF 1 **(e)** Relative Error – DOF 3 **(f)** Relative Error – DOF 5

Figure D.1: Convergence of added mass values and relative errors.

Radiation Damping Convergence

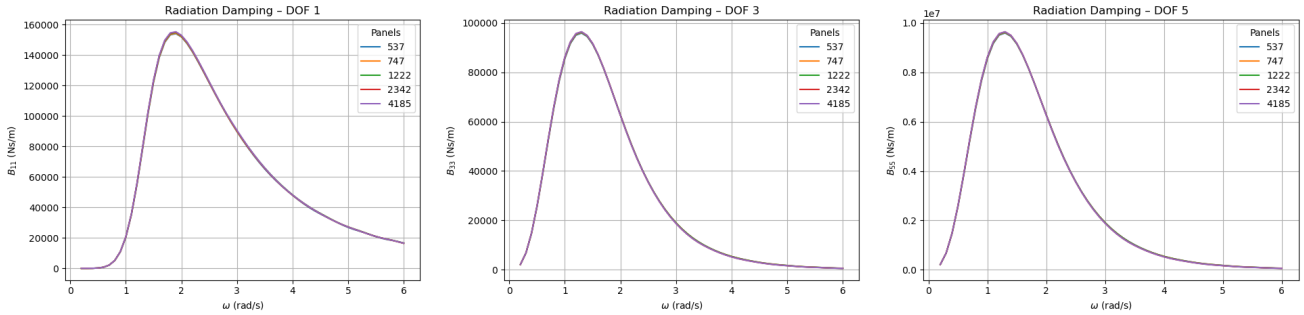

(a) DOF 1 **(b)** DOF 3 **(c)** DOF 5

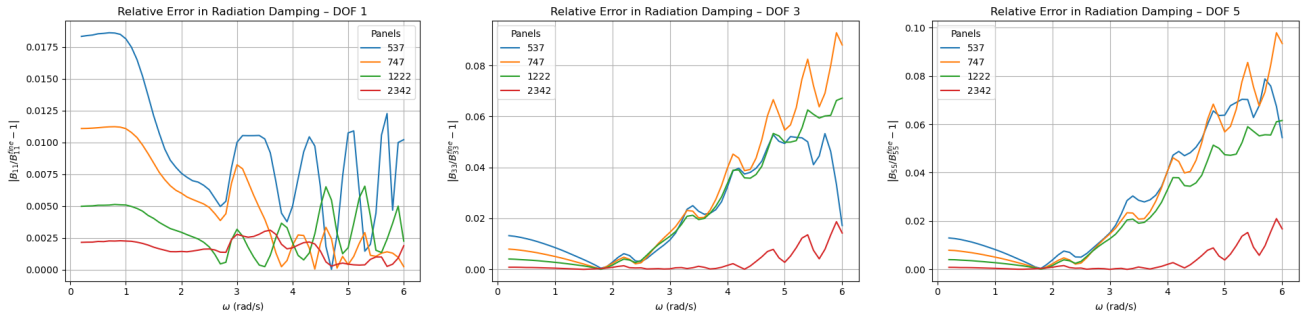

(d) Relative Error – DOF 1 **(e)** Relative Error – DOF 3 **(f)** Relative Error – DOF 5

Figure D.2: Convergence of radiation damping coefficients and relative errors.

Excitation Force: Magnitude and Phase

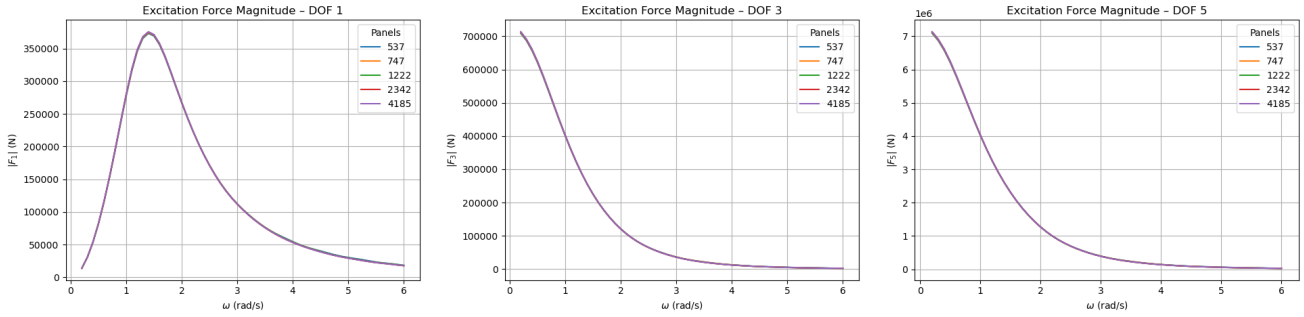

(a) Magnitude — DOF 1 **(b)** Magnitude — DOF 3 **(c)** Magnitude — DOF 5

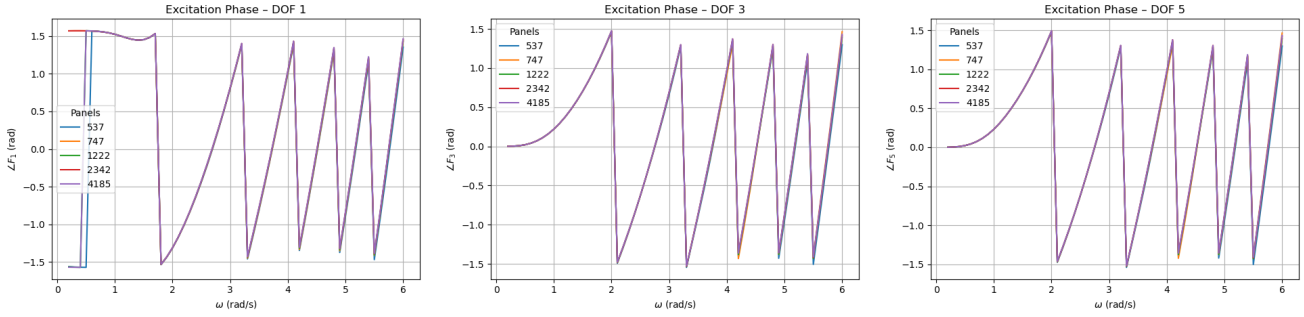

(d) Phase — DOF 1 **(e)** Phase — DOF 3 **(f)** Phase — DOF 5

Figure D.3: Convergence of excitation force magnitude and phase across mesh densities.

E

PTO parameter sweep

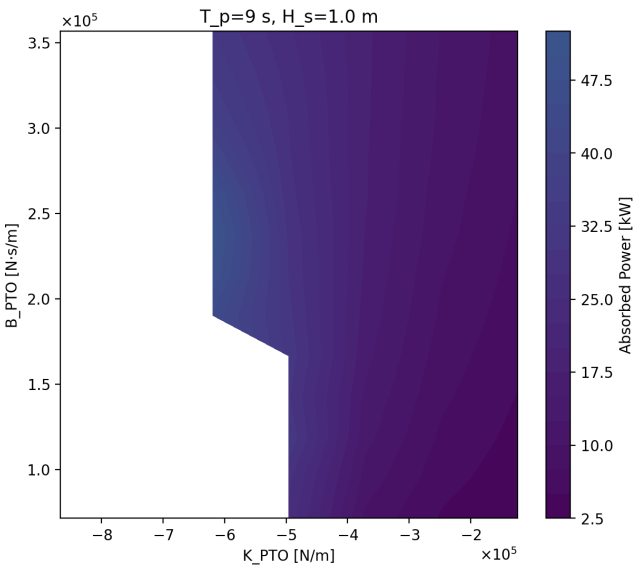

(a) $T_p = 9\,\mathrm{s}$, $H_s = 1\,\mathrm{m}$

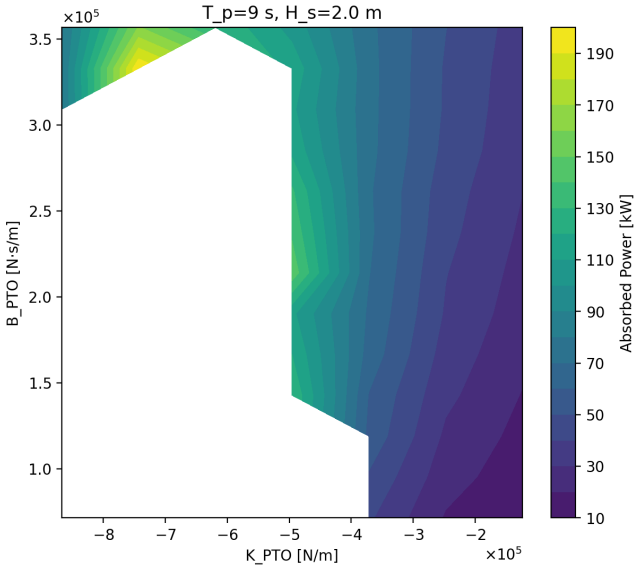

(b) $T_p = 9\,\mathrm{s}$, $H_s = 2\,\mathrm{m}$

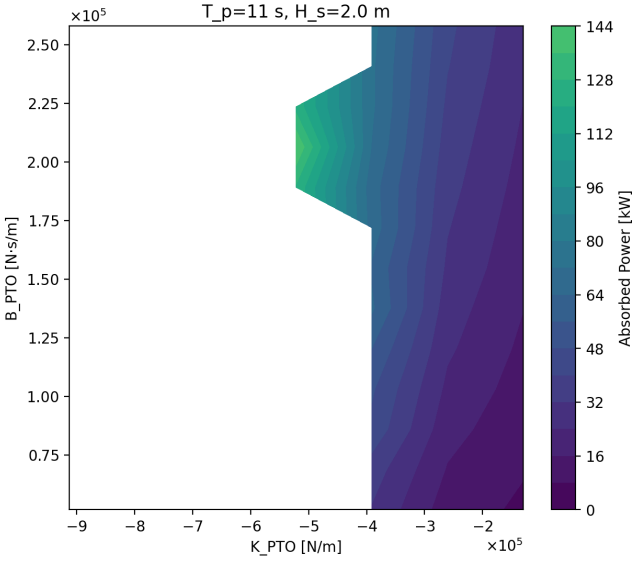

(c) $T_p = 11\,\mathrm{s}$, $H_s = 2\,\mathrm{m}$

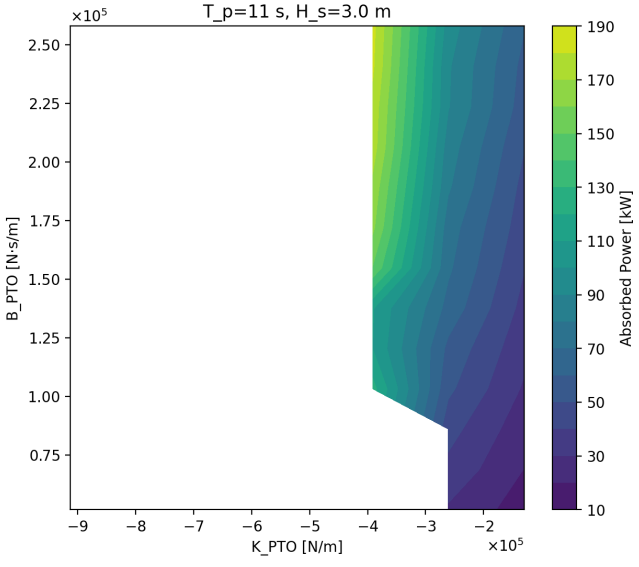

(d) $T_p = 11\,\mathrm{s}$, $H_s = 3\,\mathrm{m}$

Figure E.1: Absorbed-power surfaces from the PTO parameter sweeps for each sea state. White regions indicate non-converged harmonic balance solutions.

F

MATLAB Verification

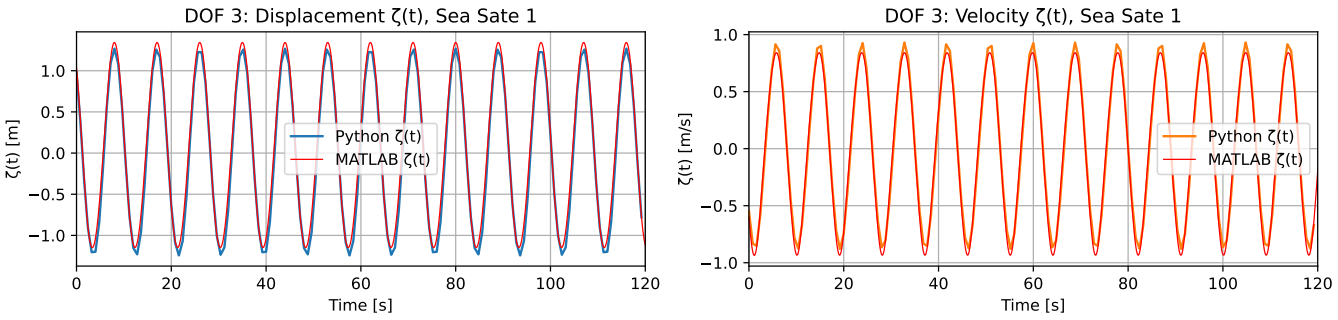

Figure F.1: Sea State 1 validation.

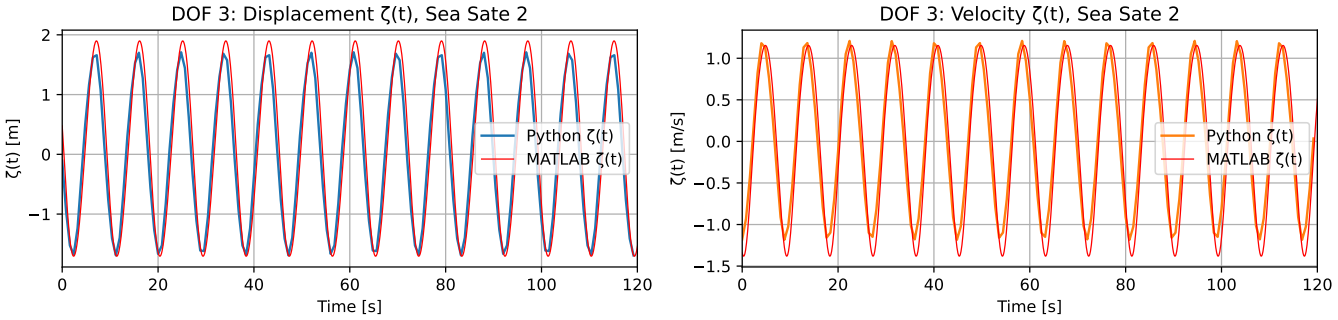

Figure F.2: Sea State 2 validation.

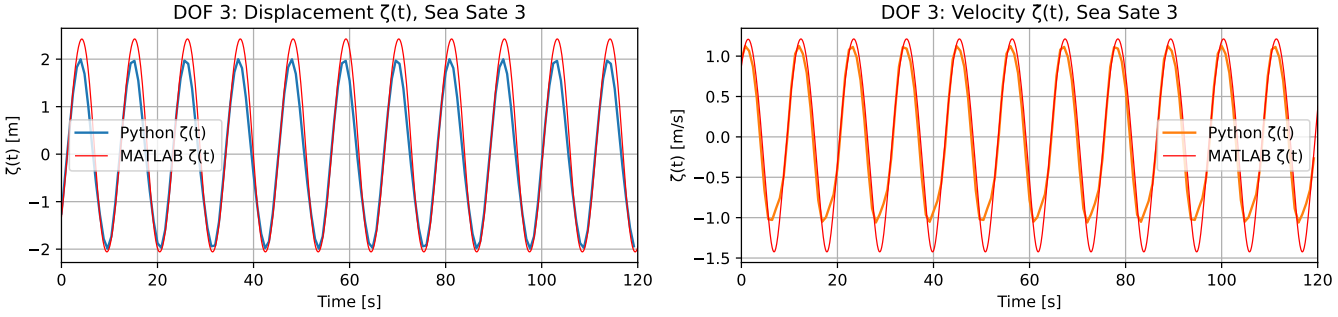

Figure F.3: Sea State 3 validation.

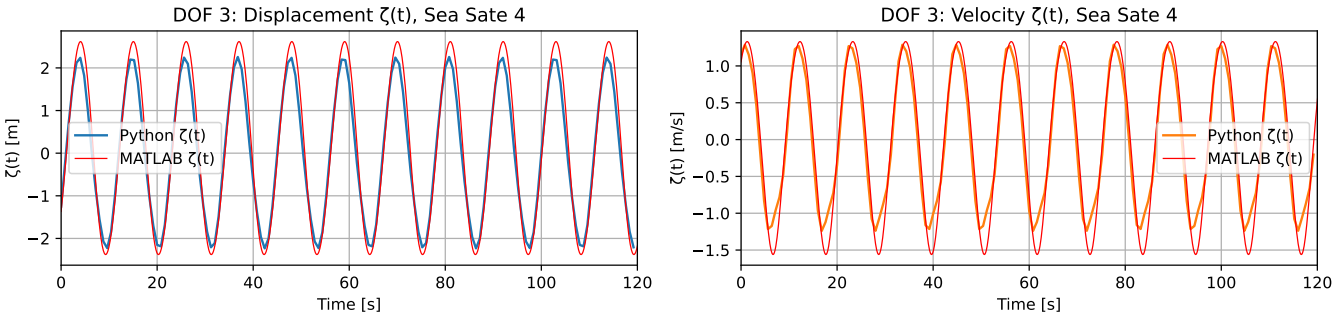

Figure F.4: Sea State 4 validation.

G

Convergence Statistics

All values denote the number of converged segments out of ten.

Table G.1: Convergence counts for spacing 5D

(T_p, H_s)	β0°	β30°	β60°	β90°
(9.0,1.0)	10	10	5	10
(9.0,2.0)	10	10	10	10
(11.0,2.0)	3	5	5	10
(11.0,3.0)	7	6	7	10

Table G.2: Convergence counts for spacing 10D

(T_p, H_s)	β0°	β30°	β60°	β90°
(9.0,1.0)	10	10	7	10
(9.0,2.0)	9	9	10	10
(11.0,2.0)	7	8	4	7
(11.0,3.0)	5	8	8	10

Table G.3: Convergence counts for spacing 15D

(T_p, H_s)	β0°	β30°	β60°	β90°
(9.0,1.0)	10	10	9	10
(9.0,2.0)	10	10	10	10
(11.0,2.0)	8	5	6	10
(11.0,3.0)	3	7	6	9

H

Linear Validation Against HAMS-MREL

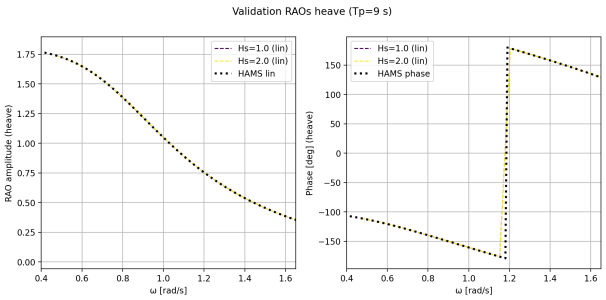

(a) Heave, $T_p = 9$ s

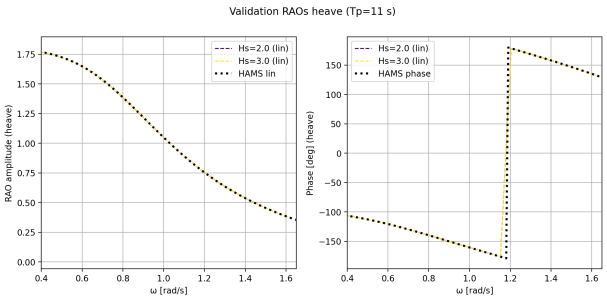

(b) Heave, $T_p = 11$ s

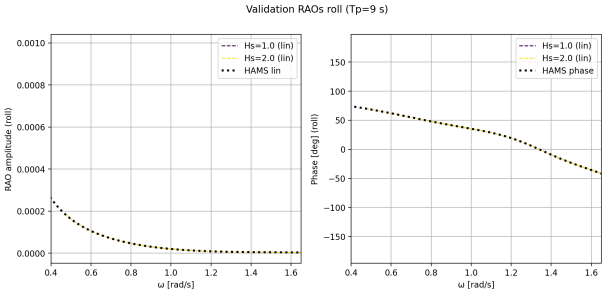

(c) Roll, $T_p = 9$ s

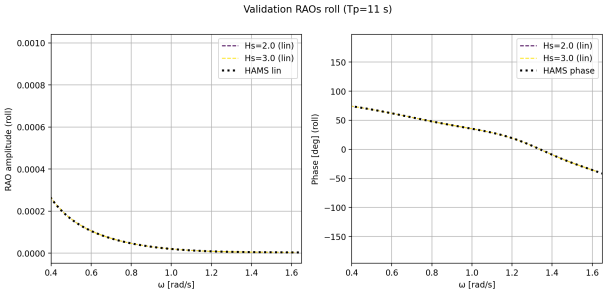

(d) Roll, $T_p = 11$ s

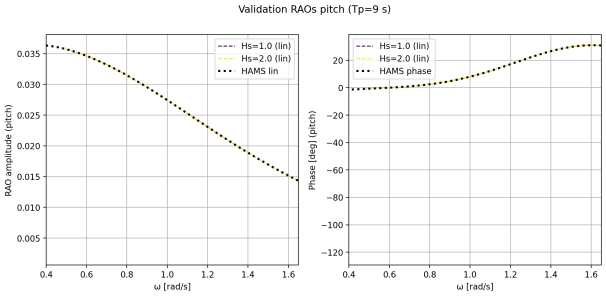

(e) Pitch, $T_p = 9$ s

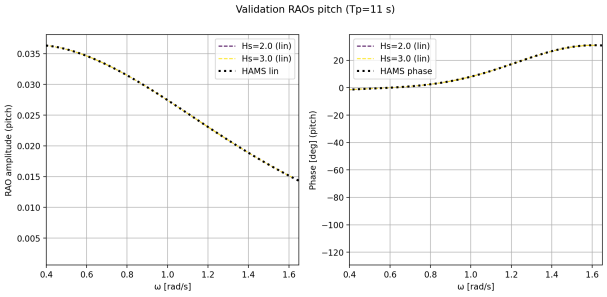

(f) Pitch, $T_p = 11$ s

Figure H.1: Linear RAO and phase validation against HAMS-MREL for $T_p = 9$ and $T_p = 11$ s. The solver collapses to the HAMS-MREL reference for all DOFs, verifying correct linear hydrodynamics.